Surge and swab pressure

A transient approach to running expandable assemblies

J.J.F.M. Willemse

Delft University of Technology

TU Delft

Surge and swab pressure

A transient approach to running expandable assemblies

by

J.J.F.M. Willemse

to obtain the degree of Master of Science
at the Delft University of Technology,
to be defended publicly on January 23 at 15:00

Student number:	4161777	
Project duration:	April 18, 2017 – January 23, 2018	
Thesis committee:	Prof.Dr. A.V. Metikine,	TU Delft
	Dr.Ir. K.N. van Dalen,	TU Delft
	Ir. J.S. Hoving,	TU Delft
	Dr.Ir. M.A.N. Hendriks,	TU Delft
	Dr. H.R. Pasaribu,	Shell Global Solutions
	Dr. W. Assaad,	Shell Global Solutions

TU Delft

Abstract

Conventional hydrocarbon well design results in a telescopic well. As a well is drilled, steel casing is cemented to the borehole to prevent collapse of the hole. Subsequent casing sections (liners) experience a stepwise reduction in diameter as each new liner must be able to pass through the previous casing. The small diameter restricts the flow of hydrocarbons, limiting production rates.

Shell is working on mono-diameter drilling (MOD). A MOD well, or MOD well section, has a (nearly) constant diameter over several sections. This is achieved by deploying expandable liners: a liner is lowered into position and is expanded by pulling an over-sized cone through it. This plasticly deforms the pipe, increasing its inner diameter to that of the previous section. MOD eliminates many of the constraints of conventional well design. Greater depths may be reached and zonal isolation may be performed without paying the penalty of reduced production rates.

While lowering an expandable assembly (expandable liner and expansion tools) into a well, caution is required. Displacement of the drilling mud causes a pressure drop due to fluid friction and acceleration. The running speed of the assembly into the well is limited by the surge (overpressure) or swab (underpressure) pressure. Pressure must remain within a predefined window to ensure well control.

The current understanding of the mechanisms governing surge/swab pressure, as well as the models used to predict it, are deemed insufficient. The effect of unorthodox MOD conditions is unknown. This study is conducted to overcome these obstacles.

Firstly, a model is programmed so that transient surge and swab pressures, induced by assembly movement, may be predicted. The drilling mud's velocity and pressure are described by the water hammer equations, which are solved using the interpolated method of characteristics. One dimensional (1D) flow of a slightly compressible fluid in a conduit with linearly elastic walls is considered. The annular pressure drop for flow with a moving inner pipe is solved considering both laminar and turbulent flow of a Herschel-Bulkley fluid. Flow over the expansion tools is solved separately and is considered 1D and incompressible. The model is validated for conventional conditions using field measurements presented in literature and performs better than existing models.

Secondly, the effect of extremely small clearances, as found in MOD applications, is investigated through a full-scale experiment on Shell's test rig. The surge and swab pressures are generally predictable. Some discrepancies between predictions and measurements are observed and are attributed to the relatively large uncertainty in clearance size and shape, which results from imperfect pipes. The surge/swab pressure's sensitivity to the size and shape of the pipes means that predictions should be treated with care. The effect of local annular flow restriction over the expansion tools is investigated too. The tools are found to cause acceleration induced transient pressures not predicted by the model. This implies that the 1D and incompressible assumption at does not describe the flow adequately.

Thirdly, the effect of MOD well design at true well depths and assembly lengths is investigated through a case study. The surge pressure is significant. The pressure drop generated in the narrow annulus between assembly and wellbore is too high to allow significant flow. Instead, all drilling mud is displaced upwards through the drillstring. Circulation while tripping in expandable assemblies is therefore impossible. At these depth and length scales, the effect of fluid compression and borehole expansion becomes significant, causing steady state models to become increasingly inaccurate with depth.

Preface

This thesis is the result of a 9 month long study conducted at Shell Rijswijk and the TU Delft.

I was first interested in MOD back in 2016, after seeing Jan-Willem van Dongen present his work on cone pop-out during a symposium. I thought the combination of fluid dynamics and structural dynamics made for an interesting and tangible problem. Who knew I would find myself working on a similar problem just a year later.

The subject was well defined and so I could hit the ground running. The modeling work was progressing faster than expected and thus the opportunity for a full-scale test became available. Motivated by this opportunity and the rather tight deadline that came with it, I spent the summer modeling and reading rather than enjoying the sun. The learning curve was incredibly steep as I had to acquire a tremendous amount of in-depth knowledge on subjects ranging from non-Newtonian fluid behavior, to pressure sensor calibration, to turbulence. I managed to finish the model and test design on time and now look back at my week on the rig as one of the most fun weeks of my education. I owe it to my colleagues at Wells R&D. Their enthusiasm, knowledge and experience have made the last 9 months a pleasure.

Having said that, my first word of thanks goes to Wissam Assaad, my supervisor at Shell. He made sure I stayed on track, especially at the beginning. I could always come to him with questions or doubts and his experience allowed us to have may insightful discussions on a wide range of topics.

Secondly, I would like to thank Karel van Dalen. His sharp intellect forced me to really understand my work. He not only provided encouragement and new ideas, but also helped me produce academically sound work.

Thirdly, Rihard Pasaribu, my mentor at Shell. Rihard was always very enthusiastic and full of ideas. The monthly meetings I had with him were very valuable. The confidence he showed in me, by allowing me to design and execute my own test on the rig, meant a lot to me.

I would also like to thank my graduation professor Andrei Metrikine. His interest in my work and willingness to spend some of this precious time thinking about my project is appreciated. His academic prowess and broad knowledge made meetings with him challenging and tiring, but also rewarding.

Last but not least, I would like to thank my friends and family for their support. My colleagues Frank, Kristel, Sander and Tessel were excellent coffee and lunch buddies. My roommates Johan, Max and Romke were always willing to listen to me as I got excited telling them about steel pipes and mud. My girlfriend Frederique was always supportive and put a smile on my face on the rare occasions during which I struggled with my research.

J.J.F.M. Willemse
Delft, January 2018

Contents

List of Tables

List of Figures

Nomenclature

List of Symbols

Symbol	Units	Description
a	m	Inner pipe radius
A	m^2	Area
A_{an}	m^2	Cross-sectional area of the annulus
A_{ds}	m^2	Cross-sectional area of the drill string
b	m	Outer pipe radius
B	-	Coefficient matrix
c	ms^{-1}	Wave propagation speed
D	m	Pipe diameter
D_h	m	Hydraulic diameter
D_i	m	Inner pipe diameter
D_o	m	Outer pipe diameter
e	-	Exponent
E	-	Coefficient matrix
E_c	Nm^{-2}	Young's modulus of cement
E_f	Nm^{-2}	Young's modulus of the formation
E_s	Nm^{-2}	Young's modulus of steel
f	-	Darcy-Weisbach friction factor
f_{int}	-	Intermediate friction factor
f_{lam}	-	Laminar friction factor
f_{trans}	-	Transitional friction factor
f_{turb}	-	Turbulent friction factor
f_u	-	Unsteady friction factor
g	ms^{-2}	Gravitational acceleration
k	$lbs^n/100ft^2$	Consistency factor for Herschel-Bulkley fluids
k_p	$lbs^{n_p}/100ft^2$	Consistency factor for Power law fluids
k_q	-	Unsteady friction coefficient
K	Nm^{-2}	Bulk modulus
K_{GC}	-	Loss coefficient for gradual contraction
K_{GE}	-	Loss coefficient for gradual expansion
K_{AC}	-	Loss coefficient for abrupt contraction
K_{AE}	-	Loss coefficient for abrupt expansion
L_1	-	Equation for conservation of momentum
L_2	-	Equation for conservation of mass
n	-	Flow behaviour index for Herschel-Bulkley fluids
n_p	-	Flow behaviour index for Power law fluids
N_{ReG}	-	Generalized Reynolds number for non-Newtonian fluids
N_{CRe}	-	Critical Reynolds number
p	Nm^{-2}	Pressure
p_{atm}	Nm^{-2}	Atmospheric pressure
p_{pump}	Nm^{-2}	Pump pressure at the surface
P_w	m	Wetted perimeter
PV	cP	Plastic Viscosity
Q	m^3s^{-1}	Flow rate
r	m	Radius
r_i	m	Inner radius
r_o	m	Outer radius

R	-	Reflection coefficient
Re	-	Reynolds number for Newtonian fluid
s	m	Streamline
t	s	Time
Δt	s	Time step
u	s	Time used in the convolution integral
$\mathbf{U}$	-	Coefficient matrix
v	ms^{-1}	Velocity
v_p	ms^{-1}	Pipe velocity
$\overline{v}$	ms^{-1}	Mean velocity
$\overline{v}_{eff}$	ms^{-1}	Effective mean velocity
$\overline{v}_{rel}$	ms^{-1}	Mean relative velocity
W	-	Weighting function
YP	$lbf/100ft^2$	Yield Point
z	m	Depth
Δz	m	Spatial step

Greek

Symbol	Units	Description
α	-	Ratio of inner pipe diameter to outer pipe diameter for annuli
δ	-	Uncertainty
γ	s^{-1}	Shear rate
ϵ	-	Kinetic energy dissipation
ϵ_e	-	Dimensionless eccentricity of the inner pipe
θ	$^\circ$	Inclination of the well
θ_3	$^\circ$	Viscometer reading at 3 rpm
θ_6	$^\circ$	Viscometer reading at 6 rpm
λ	-	Multiplier for total derivatives
λ'	ms^{-1}	Eigen values of matrix **B**
μ	Nsm^{-2}	Dynamic viscosity
μ_c	-	Poisson's ratio of cement
μ_f	-	Poisson's ratio of formation
μ_s	-	Poisson's ratio of steel
ν	m^2s	Kinematic viscosity
ρ	kgm^{-3}	Density
σ	Nm^{-2}	Stress
σ_θ	Nm^{-2}	Tangential stress
σ_r	Nm^{-2}	Radial stress
τ	Nm^{-2}	Shear stress
τ_c	-	Dimensionless time used in the convolution integral
τ_w	Nm^{-2}	Shear stress at the wall
$\tau_{w,1}$	Nm^{-2}	Shear stress at the wall for pipe flow with stationary walls
$\tau_{w,2}$	Nm^{-2}	Shear stress at the wall for pipe flow with moving walls
$\tau_{w,3}$	Nm^{-2}	Shear stress at the wall of a hydraulically equivalent pipe for annular flow with moving inner walls
τ_y	$lbf/100ft^2$	Fluid yield stress
ϕ	$^\circ$	Angle of pipe convergence or -divergence
ψ	-	Geometry factor

List of abbreviations

BHA	Bottom hole assembly
CFL	Courant-Friedrich-Lewy
HB	Herschel-Bulkley
IAB	Instantaneous Acceleration Based
ID	Inner diameter
MoC	Method of Characteristics
MOD	Mono diameter drilling
OD	Outer diameter
PL	Power-Law
TD	Total depth

Conversion to SI units

To convert from	**To**	**Multiply the non-SI value by**
lbf/100ft^2	Pa	$4.788 \cdot 10^{-1}$
ft	m	$3.048 \cdot 10^{-1}$
in	m	$2.54 \cdot 10^{-2}$
psi	Pa	$6.89476 \cdot 10^{3}$
lbf/gal	kgm^{-3}	$1.19826 \cdot 10^{2}$
cP	mPas	1

1 Introduction

"The scientific mind doesn't so much provide the right answers as ask the right questions."
— Claude Levi-Strauss

This chapter briefly introduces monodiameter drilling (MOD) of hydrocarbon wells. The advantages of monodiameter wells are stated and the objective of this thesis is presented afterwards.

1.1. Hydrocarbon wells

1.1.1. Conventional wells

Hydrocarbon wells are often several kilometers deep. Drilling mud is circulated through the drillstring into the borehole to remove drill cuttings and to stabilize the borehole by providing a pressure which counters the formation pressure. When the drilling mud is no longer able to provide sufficient counter pressure, drilling is stopped and a section of casing is cemented to the bore hole. A change in formation properties such as its composition, permeability, strength, or pore pressure may also require a casing section to be set. After the casing has been cemented to the borehole, drilling continues with a smaller drill bit that is able to fit thought the newly set casing. This process is repeated until the reservoir depth is reached. The well's diameter is reduced at every new casing section. This typical telescopic well design, pictured in Figure 1.1, leaves the well with a small diameter at reservoir depth. Deep reservoir production flow rates in particular are reduced as the small diameter restricts hydrocarbon flow. Small production volumes make it difficult to make deep wells economically feasible.

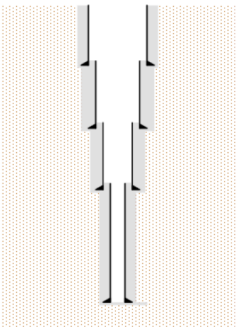

Figure 1.1: Schematic cross-sectional view of conventional tapered well design [32]

1.1.2. Monodiameter wells

MOD wells are wells in which the inner diameter of the casing is kept (nearly) constant over several well sections. This is achieved by deploying expandable liners. Monodiameter drilling is performed as follows: after a section is set, (under reamed) drilling continues to the desired depth and the drill bit is pulled out of the hole (Figure 1.2 a). A new string of tubulars (a liner) is lowered into the borehole, see Figure 1.2 b.

Cement is used to fill the annulus between the liner and the borehole. An anchoring system then holds the liner in place while it is expanded by an over-sized cone which is pulled though the liner (Figure 1.2 c). This expansion results in no (or minimal) loss in well diameter. Well sections are overlapped to ensure a good seal is created. Drilling once again continues after the cement has set.

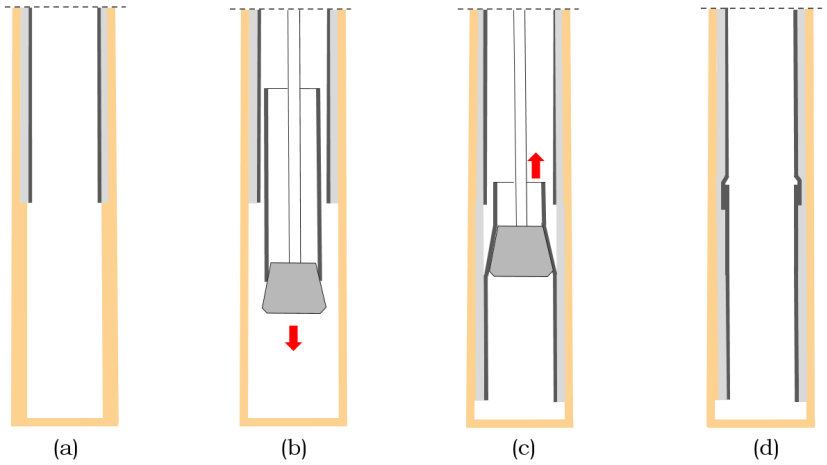

Figure 1.2: Installation of an expandable liner

Several subsequent sections may be drilled and cased with this process. Setting several expandable liners back to back results in a well with minimal to no loss in inner diameter. A schematic cross section of a monodiameter well is presented in Figure 1.3.

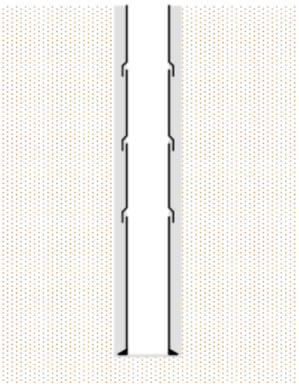

Figure 1.3: Schematic cross-section of a monodiameter well [32]

1.2. Advantages of monodiameter wells

MOD wells, or wells with MOD sections, present several advantages over traditional tapered well designs. These advantages are both environmental and economic.

Maintaining a single diameter over the entire well depth removes the need for large diameters across the first few sections. Less rock is cut and less cuttings are produced. This also reduces the wells surface footprint. Smaller drill rigs may be used as initial drilling with large bits is no longer required. These smaller rigs consume less power reducing the environmental impact of the operation.

Economically, the use of lighter rigs results in savings on rig rates. Wellhead sizes are scaled down and the use of materials such as mud and cement is reduced during the drilling of monodiameter wells. Achieving a larger diameter at reservoir depth increases production rate and therefore the generated income. Monodiameter wells also present several opportunities such as the production of deep reservoirs which are unreachable or economically infeasible using traditional well design. Expandable technology may also be used to isolate

depleted zones without a reduction in diameter allowing deeper production zones to maintain their production rates after zonal isolation is performed. It will allow the drilling of depleted, narrow margin, and unstable well sections while reaching production zones with larger conduits sizes. This eliminates many of the constraints faced by traditional well design.

1.3. Thesis objective

Shell is working on mono-diameter wells. The technology is currently in use, most notably in the Gulf of Mexico in the USA. One of the obstacles encountered in the field is the necessity to exercise extreme caution while lowering the expandable bottom hole assembly (BHA), see Figure 1.2 b. The BHA is the bottom section of the drill string; an expandable BHA consists of anchoring tools, the to be expanded liner, and expansion tools, see Figure 1.4. The running speed of the BHA is limited by the resulting surge or swab pressure. Surge (overpressure) and swab (underpressure) pressures are induced by movement of drillstring and the attached assembly. Well control is crucial during drilling, as excessive surge pressures may fracture the formation, leading to mud loss, while swabbing may cause reservoir fluid influx and, in extreme cases, blowouts. In most wells, the pressure surges are not critical since proper casing design and mud plans result in a large margin between fluid influx and formation fracture pressure. Some operations, such as running low clearance liners into deep wells or into unstable formations, as is often the case for MOD, may result in critical pressures.

Currently, a poorly understood model built without considering unorthodox MOD conditions, is used to predict the pressures resulting from drillstring movement. Running assemblies is a transient event. The aim of this master thesis is to deliver a MATLAB program capable of performing transient pressure predictions with MOD well design and pipe movement as input. The model is to be verified by comparing its predictions to data recorded during field tests as presented in literature. The performance of the model during MOD conditions is assessed through a full-scale test performed with Shell's test rig. This test will also reveal how the governing processes interact under MOD conditions.

Accurate downhole pressure predictions enable optimization of running speeds and thus a reduction in time spent tripping in or tripping out pipe; this time saving is reflected in reduced drilling costs. Careful pressure control also prevents loss of drilling mud.

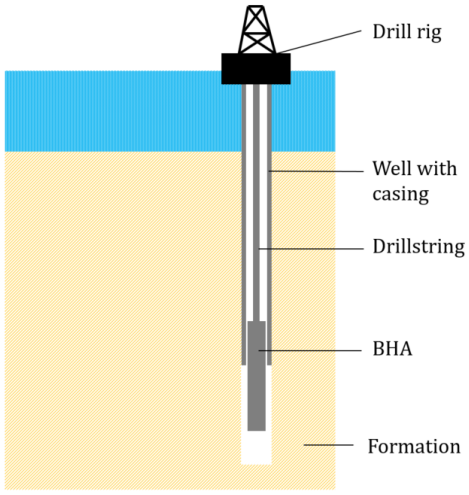

Figure 1.4: Schematic of an offshore well with the components most crucial to this thesis identified.

2

Literature

"If I have seen further it is by standing on the shoulders of Giants."
— Isaac Newton

Downhole pressure surges have long been known to cause well control problems. Cannon first identified pipe movement as a cause of pressure surges back in 1934.

In 1955, E.H. Clark Jr. studied downhole pressures due to pipe movement [7]. He concludes the surge or swab pressure is equal to the total pressure drop due to skin friction and acceleration. Assuming the fluid to be incompressibe and rigid conduit walls, the drilling mud is perfectly displaced by the drill string motion. Pressure build up due to hydraulic skin friction losses is calculated for turbulent and laminar flow. Drilling mud is assumed to behave as a Bingham fluid. Several mud velocity profiles are used to formulate a 'clinging constant,' a non-physical constant which accounts for the increase in pressure drop caused by drilling mud sticking to the moving drillstring. Pressure due to fluid acceleration is determined separately. Several pressure surge reducing practices are recommended. The results are not compared to experimental data.

J.A. Burkhardt (1961) considered the existing theories too complex as they were not fit for use in the field [5]. Along with resolving this issue, he also performed an field experiment in order to measure pressure oscillations. Steady state conditions are used to predict the pressure drop due to viscous drag, gell breaking and inertia of the mud. The pressure drop due to viscous drag is based on a clinging constant provided in graphical form, its derivation is not well explained. A distinction is made between laminar and turbulent flow. Open or closed strings are considered separately. His predictions are compared to field measurements in which pipe velocity and acceleration are measured along with the downhole pressure. The theory matches the data reasonably well and is compressed into a graphical format, allowing it to be used in the field.

J.E. Fontenot and R.K. Clark saw the need for "*An improved Method for Calculating Swab and Surge Pressures and Circulating Pressures in a Drilling Well*" [12]. Their 1974 paper describes their model which was also programmed for a computer solution. The following improvements were made with respect to the existing theory: both Bingham and power law fluid models are considered. In addition, mud properties can be varied with depth and a complex well geometry could be included. Up to ten well sections with different properties could be considered. Swab and surge pressures are calculated with the mud pumps on or off. They derived a clinging constant for laminar flow, presented in equation form, which closely matches Burkhardt's value. A different turbulent value is suggested. The program does not consider pressure build up due to gel strength or fluid acceleration, only frictional terms are considered. The model is verified with measurements from two wells and is considered adequate in most cases.

Lubinkski *et. al.* (1977) developed the first fully dynamic surge and swab pressure model based on transient wave propagation, the Bergeron graphical technique is used [20]. Previously all calculations had been performed in the steady state, assuming the fluid to be incompressible. The paper demonstrates that highly viscous fluids take considerable time to reach the steady state. This justifies the need for a transient analysis. The dynamic model stresses the significant effect of fluid compressibility and pipe and wellbore elasticity on

the pressure calculations. These are factors that cannot be accounted for in the steady state models. Friction is considered to be a lumped parameter.

In 1983, Monohar Lal improved upon Lubinski's model [19]. Friction is treated as a distributed parameter. The model calculates maximum surge or swap pressure, or its variation in time, given a trip velocity. The model is also able to specify the maximum running speed given an effective circulation density window. Influential parameters such as wellbore geometry, mud properties, flow over the drill bit, borehole expansion, and (plugged) jets and are used as input. The method of characteristics (MoC) is used to solve the governing equations. The relative effect of these parameters on the pressure magnitude is studied. Most important is the trip, or running, speed of the drillstring and BHA, followed by well geometry factors such as the casing and drillstring diameters and the depth at which the pipe is run. The mud parameters are less influential, but do influence the pressures.

The most comprehensive dynamic surge/swab model is presented by R.F. Mitchell in 1988 [22]. Mitchell's model includes the following four improvements: drillstring and annular pressures are coupled through the drillstring's radial elasticity, the drillstring and BHA displacement is determined considering viscous friction forces and the pipes' axial elasticity, fluid properties vary as a function of temperature and pressure, the elasticity of the formation, the casing, and the cement are used to determine the composite wellbore response. The article does not state clearly how the turbulent friction factors determined, but they seem to be based on power law fluid velocity profiles. Mitchell uses the interpolated MoC to solve the fluid flow and the assembly motion is solved with the tri-diagonal algorithm. The model results are compared to the data gathered by Burkhardt, and Fontenot and Clark and achieves a better fit to the measurements than previous models. Some tentative conclusions are drawn: in shallow wells, inertial and friction forces seem dominant, inertial flow oscillations are of the order of 50% of the peak surge pressures; fluid compressibility is most important in deep wells, causing steady state models to be increasingly inaccurate with depth, pressure oscillations are about 10% of the peak pressure.

More recent literature shows a trend towards approximating the dynamics of wellbore hydraulics with steady state calculations. The physics is sacrificed, or so it would seem, in order to simplify mathematics and save computation time. New regression models for laminar flow are published quite frequently. Crespo and Ahmed performed such a study and published it in 2013 [9]. They noted, albeit the large number of past studies, no controlled laboratory experiments had been performed. They investigated the effect of trip speed, fluid properties, and borehole geometry on surge and swab pressures. Based on the experimental data a regression model for steady state laminar flow conditions is made based on approximate numerical solutions in which the annulus is treated as a narrow slot. The obtained results were considered satisfactory.

Mme and Skalle performed a sensitivity analysis to investigate the effects of fluid density, plastic viscosity, yield point, bore hole diameter, and drillcollars-to-drillpipe length ratio on swab and surge pressures [23]. A simple, ready for use in the field, code was developed based on steady state flow. Results were converted into graphical form, convenient for mud and drilling engineers. Mme and Skalle concluded that mud properties and BHA configurations are carefully selected and can be varied only to a limited degree. The conclude safe tripping speeds are greatly influenced by the hole size. The clinging constant as derived in earlier work, is used to circumvent the need to determine mud velocity profiles.

3

Approach

"Nothing in life is to be feared, it is only to be understood. Now is the time to understand more, so that we may fear less."
— Marie Curie

The approach to conducting this research is explained in this chapter. The aim of this thesis is to develop and validate a numerical model which can be used to predict assembly movement induced pressure waves in (MOD) wells. Several steps are taken to achieve this goal. First, the desired model is made, and once finished, its performance under conventional conditions is assessed by comparing its predictions to measurements taken during field tests presented in literature. The validity of the model while running extremely narrow clearance liners is then judged by validating its predictions with a full-scale experiment. The last step is to perform a case study on MOD application in a deepwater well to gain understanding of how the governing phenoma interact at true well depths.

3.1. Model

A detailed description of the model is given in Chapter 4 and the fluid friction theory is covered in detail in Chapter 5. A review is provided in the subsequent sections.

3.1.1. Structure

As explained by Mitchell, swab/surge pressures form because of fluid-structure interaction. The movement of the drillstring and the BHA excites the fluid. The forces resulting from wall friction between the fluid and pipe and pressure acting on the pipe's surface retard the pipe's movement [22]. However, as the tripping speeds in MOD are fairly low (< 1m/s), the dynamic behavior of the structural component in assumed to be negligible. The drillstring and assembly are assumed to be a rigid body and to move with the velocity applied by the drilling rig's top drive. By assuming the structure to be rigid, the coupling between the fluid and the structure is ignored, the structure excites the fluid but the fluid does not influence the structure.

3.1.2. Fluid

The fluid component is solved to determine the swab/surge pressure. Movement of the BHA and drill string excites the fluid through displacement and friction. Therefore, the pressure loss is build up over the entire length of the wellbore and so the velocity and pressures of the fluid must be solved over the entire well using transient flow analysis. The conservation of mass and momentum equations are solved simultaneously considering one dimensional (1D) flow of a slightly compressible fluid through a conduit with linearly elastic walls. Under these circumstances the equations are a coupled set of hyperbolic partial differential equations often referred to as the water hammer equations [6]. The fluid is divided into four regions as seen in Figure 3.1. The regions are connected through interface conditions consisting of energy and balance of mass relations. Regions 1 (bottom hole), 2 (drillstring) and 3 (assembly annulus) are connected at the bottom of the BHA and regions 3 and 4 (annulus to surface) are coupled at the top of the assembly. Fully reflective boundary conditions are used at the system boundaries.

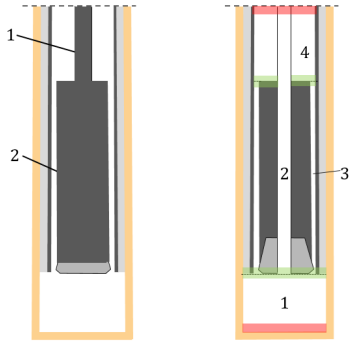

Figure 3.1: Model components, structural components on the left: (1) drillstring, (2) expandable BHA. Fluid regions on the right: (1) bottom hole, (2) drill string, (3) BHA annulus and (4) annulus to surface. Fluid boundaries indicated in red and interfaces in green

3.1.3. Solution method

The interpolated MoC is used to solve the fluid's governing equations in MATLAB. This is an intuitive and easy solution method to implement. It is first order accurate. The MoC regions are connected through interface conditions. The fine discretization required around the interfaces requires a different approach. Here the fluid is assumed to be incompressible and flow is solved using balance of mass together with a linearized energy equation. The energy equations are linearized so all non-linear terms are calculated using the velocity of the previous time step. This removes the need for an iterative solution process.

3.2. Validation

3.2.1. Field tests from literature

The results from a field test performed by Burkhardt in 1961 are used to validate the model under conventional conditions: the well is shallow and clearances are large. The effect of fluid compression and wellbore expansion is confirmed with data from a field test performed in a deeper well by Clark and Fontenot in 1974. See Chapter 7 for the results and discussion.

3.2.2. Experiment on the Rijswijk test rig

The validation step mentioned above is very valuable but several questions are left unanswered. It is unknown if the assumptions made to calculate the swab/surge pressure hold while running narrow clearance liners. Data of pressures caused by tripping extremely narrow clearance liners, as applied during MOD, is non-existent. The limited data presented by Burkhardt, and Fontenot and Clark make it difficult to judge if swab/surge pressures are consistently predictable. Therefore, a full-scale experiment is designed and executed on Shell's test rig located in Rijswijk. The effect of localized annular flow restriction is also investigated. Chapter 6 describes the experimental design, the results are presented and discussed in Chapter 7.

3.3. Application

Case study

4

Model description

"When one has a good understanding of the problem one must rid it of all the superfluous concepts and reduce it to the simplest elements."
— Rene Descartes

4.1. Structure

The drillstring and assembly form a structural component of the fluid structure interaction. They are assumed to be a rigid body and move with the velocity applied by the top drive at the surface. It is therefore not explicitly modeled. Through wall friction and the use of mass sources and sinks, the excitation of the fluid by the structure is included. To avoid continuous re-meshing of the fluid domain, the structure is fixed in place. The BHA is located at its average depth for each movement. This simplification is valid as the distance traveled by the assembly during one movement is small relative to the well depth.

Another structural component of the well is the cased wellbore. The thickness of the casing and cement layer, together with the Young's moduli and Poisson's ratios of the casing, cement and formation are used to determine the elasticity of the composite wellbore. Its effect on the fluid flow is incorporated through the wave speed as explained in the next section.

4.2. Fluid

In its simplest configuration, the fluid domain is separated into four regions as depicted in Figure 4.1. More regions may be added to capture more complex well geometries or variable mud properties. Each region is modeled as a one dimensional pipe with an equivalent hydraulic diameter. Two or more fluid regions may be connected through a set of interface conditions consisting of mass balance and energy relations. The fluid domain's boundaries require boundary conditions to solve the for the pressure and/or velocity. Working in 1D assumes that the mean axial velocity can be used to describe flow. This is a valid assumption as the axial fluxes in mass, energy and momentum are much larger than the radial fluxes. All velocities are averaged over the cross-section unless indicated otherwise. The fluid is assumed to be single phase, with no dissolved gas. Its properties (mass, temperature and rheology) must be constant for each region and are assumed to be constant over the entire length of the well.

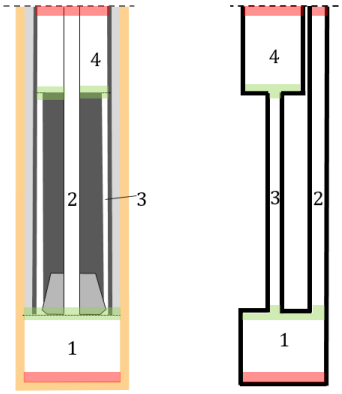

Figure 4.1: Fluid regions (1) bottom hole, (2) drillstring, (3) BHA annulus, (4) the annulus, and a schematic representation of the fluid model consisting of hydraulically equivalent pipes. Boundaries are shaded in red and the interfaces between the fluid regions in green

4.2.1. Governing equations

The transient pressure and velocity of the fluid are described by the continuity and conservation of momentum equations as derived in Appendix A. The two coupled hyperbolic partial differential equations describe the conversion between kinetic and potential energy and with that the propagation of waves in fluids.

$$\frac{\partial p}{\partial t} + \overline{v}\frac{\partial p}{\partial z} + \underbrace{\frac{1}{\left(\frac{1}{K} + \frac{1}{A}\frac{dA}{dp}\right)}}_{\rho c^2}\frac{\partial \overline{v}}{\partial z} = 0 \tag{4.1}$$

$$\frac{\partial \overline{v}}{\partial t} + \overline{v}\frac{\partial \overline{v}}{\partial z} + \frac{1}{\rho}\frac{\partial p}{\partial z} - g\sin\theta + \frac{\tau_w \pi D_{hyd}}{\rho A} = 0 \tag{4.2}$$

in which, p is the pressure, $\overline{v}$ the mean velocity, K the fluid's bulk mudulus, A the conduit's cross-sectional area, ρ the drilling mud's density, c the undamped wave speed, g the gravitational acceleration, θ the well inclination, τ_w the shear stress at the pipe wall, t is time, z depth, and D_h is the hydraulic diameter [6]. The wave speed depends on the wellbore elasticity (see Appendix C) and on the mud's compressibility. The later is assumed to be equal to that of water which is an acceptable approximation for water based drilling mud. The wave speed may be regarded as a stiffness term as it is a proportionality term in the conversion of kinetic energy into potential energy. A stiff system translates to a high wave speed. The equations are solved with the interpolated MoC, its derivation is presented in Appendix B.

4.2.2. Wall friction

The BHA and drillstring interact with the drilling mud through wall friction over the entire length of the well. Friction dissipates energy in all fluid regions, the resulting pressure drop is referred to as the major loss in pipe systems. The 2D velocity profiles differ for the various flow scenarios occurring within the well. These scenarios may be generalized to the three situations depicted below, each requires a different approach to determine the shear stress at the wall.

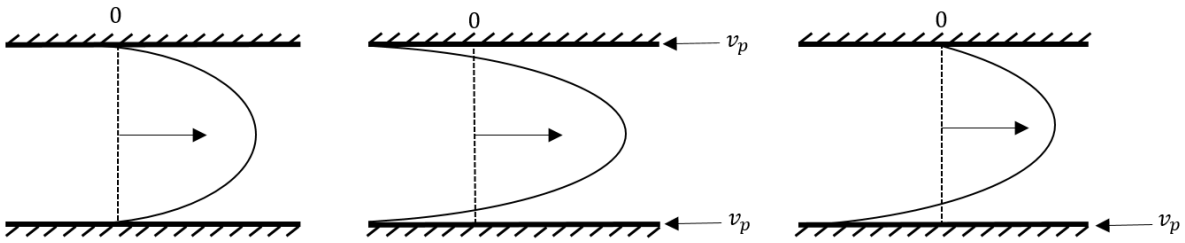

Figure 4.2: Flow situations: pipe flow with stationary walls (left), pipe flow with moving walls (middle), annular flow with moving inner walls (right), v_p is the pipe wall velocity

The shear stress at the wall is calculated using the Darcy-Weisbach friction factor. The shear stress at the wall is:

$$\tau_{w,1} = f(\overline{v})\frac{\rho}{8}\overline{v}|\overline{v}| \qquad \text{for pipe flow with stationary walls} \tag{4.3}$$

$$\tau_{w,2} = f(\overline{v}_{rel})\frac{\rho}{8}\overline{v}_{rel}|\overline{v}_{rel}| \qquad \text{for pipe flow with moving walls} \tag{4.4}$$

$$\tau_{w,3} = f(\overline{v}_{eff})\frac{\rho}{8}\overline{v}_{eff}|\overline{v}_{eff}| \qquad \text{for concentric annular flow with a moving inner pipe} \tag{4.5}$$

in which f is the Darcy-Weisbach friction factor, $\overline{v}$ is the mean velocity, $\overline{v}_{rel} = \overline{v} - v_p$ the relative velocity between fluid and pipe, and $\overline{v}_{eff}$ is the effective velocity of the fluid which accounts for fluid sticking to moving inner pipe. The theory used to determine the friction factors is discussed in Chapter 5.

4.2.3. Boundary conditions

At the surface

At the surface (top dashed line in Figure 4.1), the annulus is assumed open. The pressure in the drillstring is equal to the pressure in the mud pumps, which are assumed to be off. The boundary conditions are therefore constant pressure boundary conditions as mud is free to flow in and out. Assuming no circulation, the pressure in the pumps is equal to the atmospheric pressure. Using gauge pressure, the pressure at the surface in the drill string and annulus are:

$$p_{DS}(0,t) = p_p = p_{AN}(0,t) = p_{atm} = 0. \tag{4.6}$$

Here p_{DS} is the pressure inside the drill string, p_p the mud pump pressure, p_{AN} the annular pressure, and p_{atm} is the atmospheric pressure.

Bottom hole

At total depth, the pressure wave is either partially or fully reflected. If the wave is fully reflected, the bottom hole region is considered to be a closed system; no fluid is leaked into the formation and no formation fluid influx is permitted. Use of this boundary condition at total depth (TD) led to accurate pressure predictions according to literature [22]. It is therefore used in this study to. At TD, $z = L_{tot}$ and the velocity is

$$v_{BH}(L_{tot},t) = 0. \tag{4.7}$$

4.2.4. Interface conditions

At the interfaces between the fluid regions, various tools such as the cone, cement plug, dart-catchers, etc. give the BHA an irregular shape. To include this shape, a fine discretization is required and use of the MoC becomes impractical. Therefore, earlier work on swab pressures during cone pop-out assumed flow over the interfaces to be incompressible [32]. This approach is applied again: the interface's geometry is simplified to a 1D pipe with equivalent hydraulic diameter. The incompressible flow over the interface is solved using the unsteady Bernoulli equation as derived in Appendix D

$$p + \rho\int\frac{\partial\overline{v}}{\partial t}ds + \frac{\rho}{2}\overline{v}^2 + \rho g z = \text{constant} \tag{4.8}$$

in which p is pressure, g the gravitational acceleration , ρ the fluid's density, s is the streamline path and z the elevation. The integral accounts for the time-dependent acceleration of the fluid, making the equation unsteady. The streamline is assumed to be straight and vertical. Strictly speaking the Bernoulli equation is valid for frictionless flow only (conservation of energy). This is not the case as major and minor losses occur at the interfaces (refer to Chapter 5). The Bernoulli principle is therefore written as an energy equation to include the losses [26, 37]. As depicted in figure 4.3, the interface is discretized into several small volumes. The energy equation and balance of mass are solved over each volume

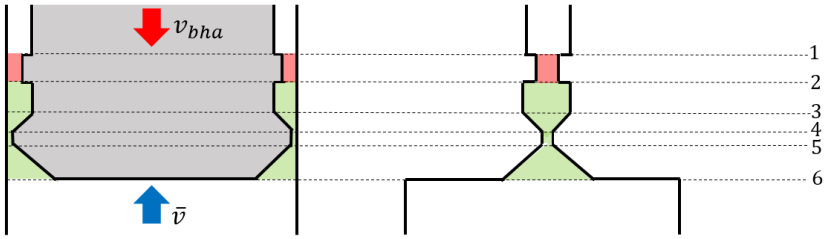

Figure 4.3: Example interface geometry and descritization. Incompressible region in green, example volume in red

For the volume shaded in red in Figure 4.3, the energy equation for upward flow is:

$$p_1 + \frac{\rho}{2}\overline{v}_1^2 + \rho g z_1 + K_{1-2}\frac{\rho}{2}\overline{v}_s^2 + \Delta p_{1-2} + \rho \int_{z_2}^{z_1} \frac{\partial \overline{v}}{\partial t} dz = p_2 + \frac{\rho}{2}\overline{v}_2^2 + \rho g z_2 \tag{4.9}$$

in which, K_{1-2} the minor loss coefficient, Δp_{1-2} the major loss over the volume. The flow in this volume is flow in an annulus with moving inner walls, resulting in the velocity profile is given in Figure 4.4. The pressure drop over the volume due to wall friction must thus be calculated with

$$\Delta p_{1-2} = f(\overline{v}_{eff,1-2})\frac{\rho L}{2D_h}\overline{v}_{eff,1-2}^2 \tag{4.10}$$

in which L is the length of the volume, D_h the average hydraulic diameter, $\overline{v}_{eff,1-2}$ the mean effective velocity in the volume. One should understand that, under steady conditions, if the pressure below the BHA is not high enough to overcome the shear applied to the fluid by the moving BHA, the net flow of fluid will be downwards.

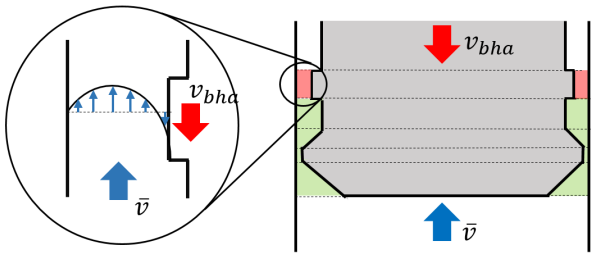

Figure 4.4: Velocity profile in the example volume

The last term on the left hand side of Equation 4.9 accounts for the effect of acceleration. It is numerically approximated by using the trapezoidal rule for the integration and the upwind method for the partial derivative [35]

$$\int_{z_2}^{z_1} \frac{\partial \overline{v}}{\partial t} dz \approx \frac{z_1 - z_2}{2}\left(\frac{\overline{v}_1^{t+\Delta t} - \overline{v}_1^t}{dt} + \frac{\overline{v}_2^{t+\Delta t} - \overline{v}_2^t}{dt}\right). \tag{4.11}$$

The energy equation is solved together with balance of mass. The volumes are assumed to be non-deformable, and thus, for the volume shaded in red in Figure 4.3

$$A_1\overline{v}_1 = A_2\overline{v}_2 - (A_2 - A_1)v_{bha} \tag{4.12}$$

where A is the cross-sectional area, $\overline{v}$ the velocity and v_{bha} the assembly velocity. The obtained set of equations is linearized by using the velocity of the previous time step in the non-linear terms and in the calculation of the the losses. The resulting set of equations may be solved directly. However, as a well is several kilometers deep, the pressure is several orders larger than the velocity, resulting in an ill conditioned set of equations. This causes the solution to become unstable when the pressure loss terms become too large. To cope with this issue three steps are taken:

1. The size of matrix is reduced by condensing the set of energy and mass balance equations into two equations: one energy equation where the losses over the whole interface are summed and one balance of mass equation ensuring mass balance at the top and bottom of the incompressible section.

2. Manual scaling is performed by multiplying the resulting energy equation by $\frac{1}{\rho^2}$
3. The scaling is further improved by considering only the differential pressure over the interface. The hydrostatic pressure is subtracted from the system of equations before it is solved, and added it again after the system has been solved.

As an example, the interface condition equations for the annulus and bottom hole (see Figure 4.5) for upward flow are given in matrix form below

$$\begin{bmatrix} A_{AN} & 0 & -A_{BH} & 0 \\ 0 & \frac{1}{\rho^2} & 0 & -\frac{1}{\rho^2} \\ 1 & \frac{1}{\rho c_{AN}} & 0 & 0 \\ 0 & 0 & 1 & -\frac{1}{\rho c_{BH}} \end{bmatrix} \begin{bmatrix} v^t_{AN,N} \\ p^t_{AN,N} \\ v^t_{BH,1} \\ p^t_{BH,1} \end{bmatrix} = \begin{bmatrix} (A_{AN} - A_{BH})\, v^t_{bha} \\ \left(-\frac{1}{2}\rho(v^{t-\Delta t}_{AN})^2 - \Sigma\Delta p^{t-\Delta t} - \rho g \Sigma \Delta z + \frac{1}{2}\rho(v^{t-\Delta t}_{BH})^2\right) \cdot \frac{1}{\rho^2} \\ v^{t-\Delta t}_{AN,N-1} + \frac{1}{\rho c_{AN}} p^{t-\Delta t}_{AN,N-1} + g\sin\theta\Delta t - \frac{\Delta t}{2D} f\, v^{t-\Delta t}_{AN,N-1} v^{t-\Delta t}_{AN,N-1} |v^{t-\Delta t}_{AN,N-1}| \\ v^{t-\Delta t}_{BH,2} - \frac{1}{\rho c_{BH}} p^{t-\Delta t}_{BH,2} + g\sin\theta\Delta t - \frac{\Delta t}{2D} f^{t-\Delta t}_{BH,2} v^{t-\Delta t}_{BH,2} |v^{t-\Delta t}_{BH,2}| \end{bmatrix} \tag{4.13}$$

in which the last two equations are a positive characteristic equation, C^+, from MoC fluid region AN (the annulus) and a negative characteristic equation,C^+, from region BH (bottome hole), $\Sigma\Delta p$ is the total pressure drop over all volumes which make up the interface , i.e. the sum of the major and minor losses of each volume, f is the friction factor and N the number of nodes in the neighboring MoC region. The first subscript indicates the MoC fluid region for which the characteristic is written, the second subscript indicates the node number, the superscript identifies the time step at which the value is taken.

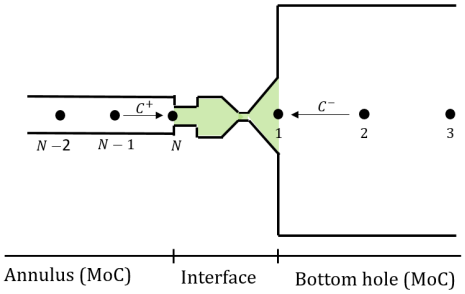

Figure 4.5: Numerical approach to solving flow over the interface. Rotated 90 degrees for convenience. Upward flow is right to left

The velocities at the top and bottom of the interface volumes (see Figure 4.3) are subsequently solved using balance of mass in the form of Equation 4.12 so that the losses over each volume may be estimated for the next time step. The solution has been compared to that of a uncondensed, unlinearized and iterative solution. The difference in the solution is negligible, the stability and computation time are drastically improved.

4.2.5. Initial conditions

While running MOD assemblies into a well, it is generally impossible to circulate mud. Initially the system is thus assumed to be at rest. Fluid velocity is zero throughout the wellbore and the pressure distribution is hydrostatic.

4.3. Pressure coupling through pipe

Mitchell states that pressure coupling through the drill string is possible, i.e. a large difference in pressure in the drill string and in the annulus radially expands or contracts the drillstring as depicted in Figure 4.6. This elastic deformation of the string couples the pressures in the two fluid regions [22]. The significance of this coupling is investigated by determining the change in area of the annulus and drillstring after applying a large pressure difference across the drillstring ($P_{AN} << P_{DS}$). This is done using the composite elasticity of the wellbore as described in Appendix C. It is found that both the change in area and the resulting change in pressure is insignificant. The assumption that the fluid regions are not coupled through radial pipe expansion is therefore justified.

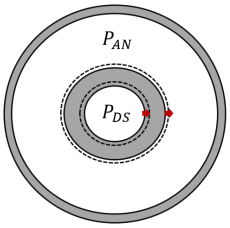

Figure 4.6: Pressure coupling in the borehole, a large pressure difference deforms the pipe resulting in coupling

4.4. Implementation

The theory described above is implemented into MATLAB. A flowchart of the model is presented in Appendix I. During implementation some practical considerations must be taken into account.

4.4.1. Fluid region length

A rectangular MoC grid is used. This grid type is inflexible as the Courant number must equal one. The numerical wave speed must thus equal the physical wave speed. The spacial discretization is thus proportional to the time step and wave speed

$$\Delta z = c\Delta t. \tag{4.14}$$

A single time step is used to perform the simulation. As the wave speeds vary per fluid region, it is impractical to attempt to find a spacial discretization for each region such that Equation 4.14 is satisfied for all regions by a single time step. A common approach used in piping systems is to alter the wave speed or section length slightly so that a single time step is used for the whole system [6]. The current model includes the second option, slightly lengthening or shortening the fluid sections, as depicted in Figure 4.7, so that one time step governs the system. Sufficiently fine spatial discretization minimizes the error.

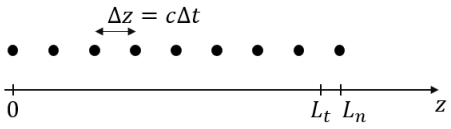

Figure 4.7: Adjusting the section length: L_t is the true section length, adjusted to L_n so that Δt may be used as the time step

4.4.2. Interpolation

The CFL stabilty criterion is derived considering only the linear terms of Equations 4.1 and 4.2. Therefore, instability may occur if the non-linear friction term becomes too large, even if the stability criterion is met [6]. Refering to Appendix B, we may write the friction term as

$$\frac{1}{2D} f \overline{v}|\overline{v}|\Delta t \tag{4.15}$$

from which it is evident that a high friction factor, high velocity, small diameter or large time step may result in a large friction term. Refining the spatial discretization will result in a smaller time step and thus smaller friction term. However, this is an inefficient approach since computational time increases quadraticly with the spatial step. The MoC scheme is therefore interpolated using the method of specified intervals [6]. The Courant number is set to unity throughout the system whenever possible. If instability occurs, the Courant number may be decreased while using a value as close to unity as possible. This makes the numerical scheme significantly more stable. Using a Courant number close to unity minimizes the numerical damping and dispersion introduced by the interpolations.

4.4.3. Flowpaths

Various scenarios are investigated with the model. Therefore, it has the capability to exclude certain fluid regions. Flow may be permitted to exit the bottom hole region through either the drill string, through the annulus, or through both.

5

Fluid friction

The surge or swab pressure is the sum of the pressure drop which occurs over the entire length of the wellbore. The frictional pressure drop is a major component, and therefore significant effort was committed to correctly include all relevant phenomona. The mechanisms causing frictional pressure drops in piping systems are generally divided into two categories. Major losses, or skin friction losses occur due to friction between the fluid and conduit's walls. As mentioned in the previous chapter, three situations occur:

1. Pipe flow with stationary walls (the bottom hole region below the BHA).
2. Pipe flow with moving walls (inside the drillstring).
3. Concentric annular flow with a moving inner pipe (inside the annuli).

Minor losses, also called nozzle pressure losses, are losses which occur locally due to changing conduit geometry. Before the losses are discussed, the mud's rheology is briefly examined.

5.1. Rheology

Rheology studies the relationship between the shear in a fluid and the applied stress. A fluid is considered Newtonian if the relation between shear stress and shear rate is linear. The two are linked through a proportionality constant: viscosity. Newton's law of viscosity is expressed with the constitutive equation

$$\tau = \mu \frac{\partial v}{\partial y} = \mu \gamma \tag{5.1}$$

in which τ is the shear stress, μ the dynamic viscosity and $\frac{\partial v}{\partial y} = \gamma$ the shear rate. The shear rate is defined with Figure 5.1.

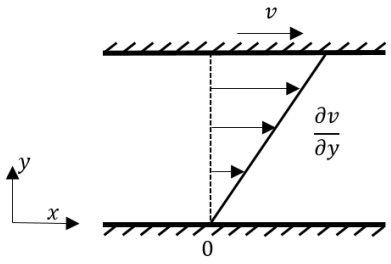

Figure 5.1: Flow between two parallel plates, the upper of which is moving with velocity v. The shear rate is the velocity gradient

A fluid is non-Newtonian if it does not follow Newton's law of viscosity. Non-Newtonian behavior may be sub-categorized into [13]:

1. **Generalized Newtonian** - shear stress is solely dependent on shear rate
2. **Time dependent** - shear stress is dependent on shear rate and a loading history

3. **Viscoelastic** - fluids not only behave viscously but also show Hookean behavior

Drilling mud tends to show all three kinds on non-Newtonian behavior. Modeling time-dependent and elastic effects is extremely complex and often impossible. Let us therefore assume drilling mud to be a generalized Newtonian fluid. It may be treated as either a power-law (PL), Bingham or Herschel-Bulkley (HB) fluid. The qualitative rheology curve of each fluid is given in Figure 5.2.

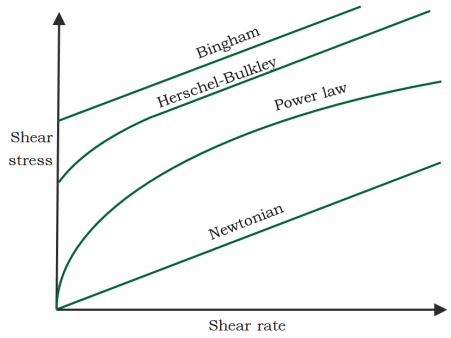

Figure 5.2: Drilling mud rheology

Drilling mud is a shear-thinning fluid: it becomes less viscous as shear rate increases. It is also known to develop a so called "gel strength," meaning it can sustain a shear stress at zero shear. Out of the three most commonly used rheology models, only the HB model captures both the shear-thinning and gelling behavior.

5.2. Major losses

Traditional transient pipe flow algorithms incorporate either steady or quasi-steady friction. Friction is included through a frictional term in the momentum equation. The friction term contains a friction factor, which is constant in steady friction models and dependent on the instantaneous local velocity in the quasi-steady models. The following sections explain how the quasi-steady friction factors used in this study are determined for the three flow scenarios listed at the start of this chapter.

5.2.1. Pipe flow with stationary walls

The method recommended by the American Petroleum Institute (API) for determining quasi-steady friction factor of a HB fluid is followed in this study. This method simplifies the non-Newtonian behavior by determining the shear rate at the wall using a Newtonian relation, which effectively eliminates the extra dimensions required to describe non-Newtonian flow. The non-Newtonian rheology is then used to determine the shear stress at the wall. A shear stress based generalized Reynolds number leads to the friction factor. This approach is limited to pipes and annuli with stationary walls. HB rheology is described by the following relation [1]:

$$\tau = \tau_y + k\gamma^n \tag{5.2}$$

in which,

$$n = 3.32 \log\left(\frac{2PV + YP - \tau_y}{PV + YP - \tau_y}\right) \tag{5.3}$$

$$k = \frac{PV + YP - \tau_y}{511^n} \tag{5.4}$$

where τ_y is the yield stress, n flow behavior index, PV the plastic viscosity, YP the yield point and k the consistency factor. Complex HB relations are difficult, sometimes impossible, to calculate analytically. Based on the assumption that the log-log slope of a HB fluid is close to that of a PL fluid at high shear rates, HB fluids are treated as generalized PL fluids characterized by n_p and k_p at high shear rates.

$$n_p = 3.32 \log\left(\frac{2PV + YP}{PV + YP}\right) \tag{5.5}$$

$$k_p = \frac{PV + YP}{511^{n_p}}. \tag{5.6}$$

The friction factor is dependent on the Reynolds number. This dimensionless parameter provides the ratio of viscous and inertial forces and is used as an indication of whether flow is laminar or turbulent. Laminar flow is dominated by viscous forces while inertial forces govern turbulent flows. For Newtonian fluids the viscosity is used to determine the Reynolds number. As viscosity is not constant in HB fluids, a shear stress based generalized Reynolds number is used

$$N_{ReG} = \frac{\rho \overline{v}^2}{19.36\tau_w} \tag{5.7}$$

where ρ is the fluid density [lb_m/gal], $\overline{v}$ the fluid velocity [ft/min] and τ_w the shear stress at the wall [$lb_f/100ft^2$]. Parameter units are included as they are imperial units. Determining the shear stress at the wall requires the use of a Newtonian relation:

$$\gamma_w = \frac{1.6 B_\psi \overline{v}}{D_{hyd}} \tag{5.8}$$

in which γ_w is the shear rate at the wall in [s^{-1}], and D_h the hydraulic diameter of the the conduit [in]. For a circular pipe the hydraulic diameter is equal to the diameter. For a non-circular conduit the hydraulic diameter is

$$D_h = \frac{4A}{P_w}, \text{ for annuli} = D_o - D_i. \tag{5.9}$$

Here A is the cross-sectional area and P_w the wetted perimeter. D_o is the inner diameter of the outer pipe and D_i is the outer diameter of the inner pipe. B_ψ is a geometry correction factor:

$$B_\psi = \left[\frac{(3-\psi)n+1}{(4-\psi)n}\right]\left[1+\frac{\psi}{2}\right] \tag{5.10}$$

in which ψ is a geometry factor[-], $\psi = 0$ for pipes $\psi = 1$ for annuli. The shear stress can at the wall may now be calculated according to:

$$\tau_w = 1.066\left(\left(\frac{4-\psi}{3-\psi}\right)^n \tau_y + k\gamma_w^n\right). \tag{5.11}$$

The flow regime is either laminar, transitional or turbulent and has a large effect on the maginitude of the friction factor. The critical Reynolds number, at which flow becomes transitional, is defined as

$$N_{CRe} = 3470 - 1370n \tag{5.12}$$

for non-Newtonian fluids. The generalized Reynolds number is now used to calculate the friction factor. Laminar flow friction factors for pipes and concentric annuli may be evaluated with a singe relation:

$$f_{f,lam} = \frac{16}{N_{ReG}}. \tag{5.13}$$

A friction factor for transitional flow is defined according to the empirical relation

$$f_{f,trans} = \frac{16 N_{ReG}}{N_{CRe}^2}. \tag{5.14}$$

The turbulent friction factor is determined one of two ways. The first uses the Blasius form of the turbulent-flow friction factor. It is most accurate for non-Newtonian fluids but it assumes smooth pipe walls which is valid only for low Reynolds number turbulent flow (upto Re = 10000). It is based on the power law parameters derived in equations 5.5 and 5.6.

$$f_{f,turb} = \frac{a}{N_{ReG}^b} \tag{5.15}$$

in which a and b are obtained by curve fits on PL fluids

$$a = \frac{\log(n_p) + 3.93}{50} \tag{5.16}$$

$$b = \frac{1.75 - \log n_p}{7}. \tag{5.17}$$

The second method is used for high Reynolds number turbulent flow. Friction factors for turbulent non-Newtonian flow are assumed to be the same as for Newtonian flow as the viscosity is (nearly) constant at high shear rates. The implicit Colebrook-White equation is the most established formulation of Newtonian friction factors for flow in rough pipes. Many explicit approximations exist, the most convenient and accurate of which is the Haaland approximation [37]:

$$f_{f,turb} = \frac{1}{4}\left(-1.8\log\left(\frac{6.9}{N_{ReG}} + \frac{\xi}{3.7D_h}\right)^{1.11}\right)^{-2} \tag{5.18}$$

in which ξ is the wall roughness. The following relations are used to calculate a friction factor which may be used across all three flow regimes

$$f_f = (f_{f,int}^{12} + f_{f,lam}^{12})^{\frac{1}{12}} \tag{5.19}$$

where,

$$f_{f,int} = (f_{f,trans}^{-8} + f_f, turb^{-8})^8. \tag{5.20}$$

The Darcy-Weisbach friction factor is four times larger than the Fanning friction factor which has just been determined. The quasi-steady Darcy-Weisbach friction factor, f, is used to determine the shear at the wall.

$$f = 4f_f \tag{5.21}$$

Now that the friction factor is known, the friction loss term in the momentum equation is known:

$$\tau_{w,1} = f(\overline{v})\frac{\rho}{8}\overline{v}|\overline{v}|. \tag{5.22}$$

5.2.2. Pipe flow with moving walls

It is rather trivial to find the friction factor for flow inside the drill string. The procedure described above is used but $\overline{v}$ is replaced with $\overline{v}_{rel}$, the mean relative velocity between the pipe and the fluid.

$$\tau_{w,2} = f(\overline{v}_{rel})\frac{\rho}{8}\overline{v}_{rel}|\overline{v}_{rel}|. \tag{5.23}$$

5.2.3. Concentric annular flow with moving inner walls

Due to the no-slip boundary conditions at the annular pipe wall, the velocity profile is skewed, see Figure 4.2. An unknown amount of mud 'clings' to the moving inner pipe. This restricts flow, increases the shear rate at the wall, and consequently causes the pressure drop per unit length to increase. Therefore, a separate procedure is required here. Older literature on swab and surge pressures recommends the use of an effective velocity ($\overline{v}_{eff}$). The effective velocity is the velocity for an annulus with stationary walls which results in the same pressure drop as the actual more complex flow:

$$\overline{v}_{eff} = \overline{v} - c_c v_p \tag{5.24}$$

in which $\overline{v}$ is the fluid velocity, c_c is the clinging constant and v_p is the pipe velocity. Several different formulations for the clinging constant are provided by different authors, see Figure 5.3. Unfortunately none are clear on how they obtained their values. More recent swab/surge models use fluid velocity profiles to determine the pressure drop through integration of the velocity profile [15, 22]. The following conclusions are drawn:

1. **Velocity profiles** - an exact analytical solution exists for Newtonian and PL fluids in laminar slit flow. No such solutions exist for turbulent flow. Approximations can be made for turbulent PL velocity profiles but these are highly sensitive to the boundary layer discretization [10]. This approach is computationally expensive as the model becomes quasi-2D. No HB fluid solutions exist. The velocity profiles become increasingly inaccurate as the ratio between outer and inner pipe diameter (α) decreases. They are derived for parallel plate flow ($\alpha = 1$), not for annular flow ($0 < \alpha < 1$).
2. **Clinging constant** - this method is computationally much faster and would allow us treat the fluid as a HB fluid. The turbulent pressure drop is also easily determined. However, clinging constant values from literature are dubious. The range in suggested values is large and derivations are absent or unclear.

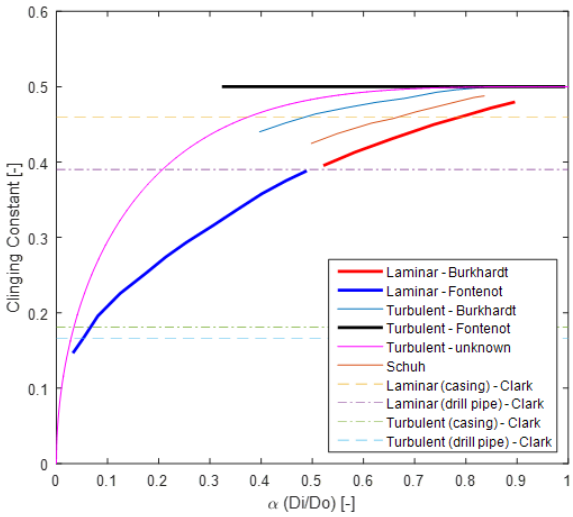

Figure 5.3: Clinging constants found in literature as a function of $\alpha = \frac{D_i}{D_o}$, the ratio of inner to outer pipe diameter

The clinging constant

The clinging constant approach is the better option, and so we must determined which values to use. Therefore the following steps are taken:

1. An analytical solution to the clinging constant is found for laminar fully developed uniform steady flow of an incompressible Newtonian fluid in an annulus.
2. For turbulent fully developed uniform steady flow of an incompressible Newtonian fluid in an annulus, the clinging constant is found using CFD simulations, performed in FLUENT by ANSYS using a $K-\epsilon$ turbulence model.
3. The effect of non-Newtonian behavior on the clinging constant is investigated using the analytical solution of laminar flow of PL fluids between two parallel plates. For flow between two parallel plates α=1. The clinging constant is determined for two PL fluids at various shear rates so that the influence of the shear thinning viscosity may be investigated.

The results are plotted in Figure 5.4. The complete derivation of the laminar values, discussion of the CFD calculations, derivation of PL fluid slit flow velocity profiles and discussion of velocity profiles are provided in Appendix D.

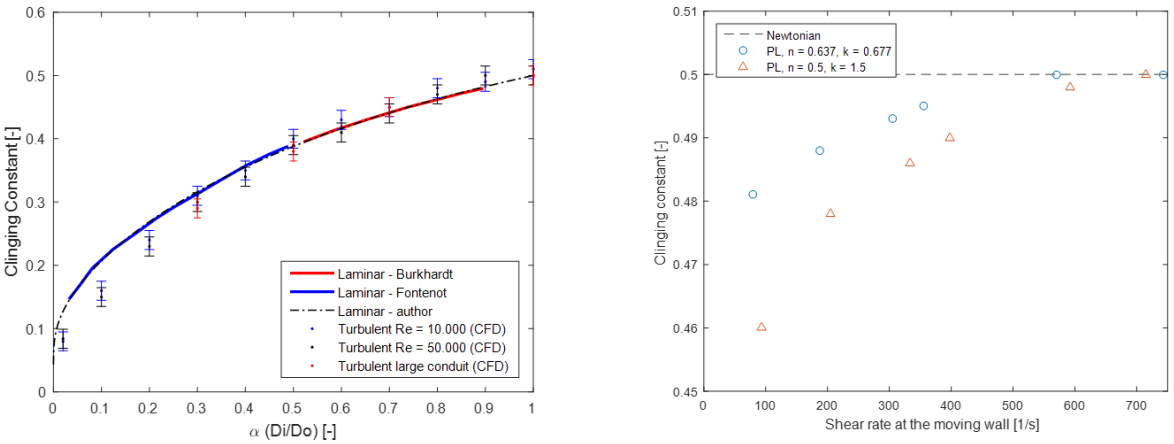

Figure 5.4: Clinging constant derived in this study: for Newtonian flow in annuli (left), and the effect of non-Newtonian behavior considering slit flow (right)

Several conclusions are drawn from Figure 5.4.

1. The laminar clinging constant presented in graphical form by Burkhardt and in equation form by Fontenot and Clark is confirmed to be
$$c_c = \frac{2\alpha^2 \ln(\alpha) - \alpha^2 + 1}{2(\alpha^2 - 1)\ln(\alpha)}, \quad \alpha = \frac{D_i}{D_o} \tag{5.25}$$
2. All turbulent formulations from literature are incorrect as none match the CFD results.
3. The turbulent clinging constant seems to be independent of the Reynolds number or conduit size. It only depends on ratio of inner to outer pipe diameter (α).
4. The shear thinning nature of PL and HB fluids ensures that the Newtonian value is always conservative. In the shear thinning regime ($\gamma < 600$ s^{-1}), the PL clining constant is less than the Newtonian value of 0.5. At shear rates above 600 s^{-1}, the viscosity becomes constant and the PL value matches the Newtonian value.

Analyzing the velocity profiles of the fluid along with the clinging constant yields an interesting insight. The last term in Equation 5.24 equals the mean velocity of flow induced by inner pipe movement only. This explains the decrease in c_c as α decreases: the shear stress distribution in the annulus is less uniform for small α, it is higher at the inner wall than at the outer wall. This skews the velocity profile as shown in Figure 5.5. In addition, cylindrical integration results in a smaller volume traveling down with the pipe as α decreases. Generalizing this finding means that the pressure drop of complex flow scenarios may be found through an effective mean velocity, which is the sum of the mean velocity of the individual flow components. This simplification holds as long as the convective acceleration is assumed to be zero.

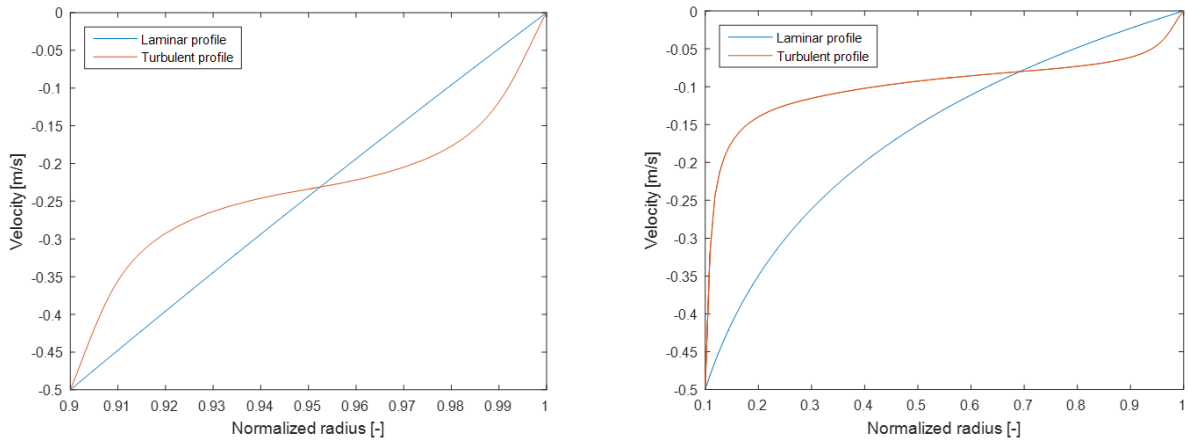

Figure 5.5: Annular velocity profiles of shear driven Newtonian fluid flow, the inner pipe moves with $v_p = 0.5$ m/s, $\alpha = 0.9$ (left), $\alpha = 0.1$ (right)

Implementation

For practical application the laminar value of the cling constant is used for all flow regimes. When $0.5 < \alpha \leq 1$, the values of the turbulent and laminar clinging constant are nearly equal. If $\alpha < 0.5$, the laminar clinging constant is larger. Using the laminar value for turbulent flows is conservative and avoids the use of dubious curve fitting required to obtain a continues solution for the turbulent value. The shear stress at the wall is calculated according to the API approach using $\overline{v}_{eff}$ (Equation 5.24) instead of $\overline{v}$.

$$\tau_{w,3} = f(\overline{v}_{eff})\frac{\rho}{8}\overline{v}_{eff}|\overline{v}_{eff}|. \tag{5.26}$$

Flow regime

The random eddies which characterize turbulent flow dissipate energy, hence turbulent flows cause a larger pressure drop than laminar flows. The critical Reynolds number determined in Equation 5.12 is only valid if both walls are stationary. Here flow is driven solely by a pressure gradient and is referred to as Poissueille flow.

If there is no pressure gradient and flow is driven by wall movement only, the flow is classified as Couette flow. In this study, we often deal with combined Couette-Poisueille flow, both the pressure gradient and wall speed are non-zero, see Figure 5.6. Couette flow is less stable than Poisueille flow, meaning it may become turbulent at a lower Reynolds number. Couette flow has been demonstrated to become turbulent at Reynolds numbers as low as 750. Literature on combined Couette-Pouisueille flow is rare as it is very difficult to create in a laboratory. One study by Potter is found [25]. He concludes Couette-Pouisueille flow is always laminar if $v_p > 0.7v_{max}$. Potter claims to have investigated the scenario in which v_p opposes v but presents no conclusions. Due to the lack of studies, the critical Reynolds number will be calculated according to Equation 5.12.

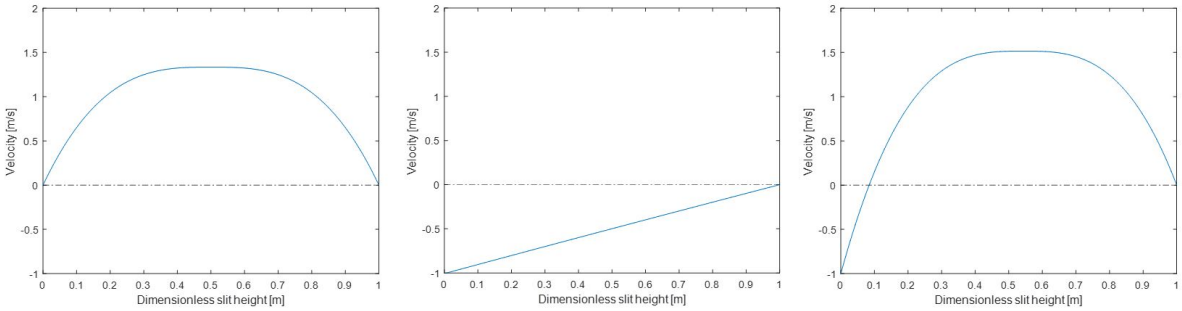

Figure 5.6: Velocity profiles for PL fluid. Poisueille flow (left), Couette flow (middle) and combined Couette-Poisueille flow (right)

5.2.4. Eccentricity

It is well established that eccentricity of the inner pipe reduces the pressure drop per unit length compared to the concentric situation. Eccentricity lowers the resistance to flow in the wide section of the annulus but may result in no-flow plugs in the narrow sections. This behaviour is amplified in drilling mud due to its non-linear rheology. A regression model which predicts the ratio of eccentric pressure drop to concentric pressure drop for HB fluids is suggested in literature [28].

$$\frac{(\Delta P_s/\Delta L)_{ecc}}{(\Delta P_s/\Delta L)_{con}} = 1 - 0.2391\epsilon_e n^{0.144}\alpha^{0.5568} - 1.309\epsilon_e^2 n^{0.7237}\alpha^{0.2856} + 1.0033\epsilon_e^3 n^{0.8741}\alpha^{0.2379} \tag{5.27}$$

n which ϵ_e is the dimensionless eccentricity expressed as $\epsilon_e = e/(r_o - r_i)$, where e is the offset distance between the center of the two pipes, r_o the outer pipe's radius, r_i the inner pipe's radius, n the fluids flow behavior index, and α is ratio of pipe diameters. The regression model is valid for $0.2 < \alpha < 0.8$, $0.2 < n < 1$ and $0 < \epsilon_e < 0.9$. If the well is perfectly vertical the drillstring and assembly should be assumed to be concentric in the host casing. If the well has a significant inclination, the assembly may be considered to be eccentric.

5.2.5. Unsteady major losses

Use of quasi-steady friction assumes flow is steady. As transient flow is considered, this is not the case. During a transient event, the maximum velocity and shear stress at the wall are out of phase and higher harmonics of the wave dampen out faster than low frequency components [4, 24, 38]. This results in a phase shift and attenuation not predicted by 1D quasi-steady models but observed in experiments performed by several authors. Unsteady friction losses should be included into the water hammer equations along with the quasi-steady friction. The study of 1D unsteady friction models is a complex field as one is attempting to fit a 2D effect into a 1D expression. One should be aware that unsteady friction theory is based on transient events in water pipe systems induced by sudden valve closure or opening. The available models can generally be placed into one of the following categories [6]:

1. **(Quasi-)2D models** - the effect of velocity in the radial direction as well as the phase differences are included. They are computationally very expensive and to be used on short and simple systems only, therefore not considered in this research.
2. **Instantaneous Acceleration Based (IAB) models** - are based on the assumption that the unsteady friction losses depend on the instantaneous local convective and temporal acceleration.
3. **Frequency-dependent models** - the unsteady friction coefficient is determined through a convolution integral. This integral is based on the analytical solution of laminar Newtonian pipe flow and has been extended to turbulent flow by various researchers.

IAB models

The unsteady friction factor according to the modified IAB (MIAB) model is:

$$f_u = \frac{k_q D}{\overline{v}|\overline{v}|}\left(\frac{\partial \overline{v}}{\partial t} + c\,\mathrm{sgn}(\overline{v})\left|\frac{\partial \overline{v}}{\partial z}\right|\right) \tag{5.28}$$

in which k_q is the unsteady friction coefficient, D the diameter and $\mathrm{sgn}(\overline{v}) = \pm 1$ depending on the direction of $\overline{v}$ [2, 6, 33]. The original IAB model was modified by inclusion of the $\mathrm{sgn}(\overline{v})$ operator to ensure the friction factor is always positive. An extensive literature review has led the author to conclude that the (M)IAB models are untrustworthy. The formulation is based on the fairly arbitrary assumption that the friction factor depends on the local instantaneous accelerations, fails under certain transient events, and it seems that the additional damping is numerical in nature [6, 34]. The unsteady friction coefficient, for which various empirically determined formulations are available, appears to be used to scale the numeric error so that predictions match measurements. Figure 5.7 shows the dependence of the unsteady losses on the numeric error. The observed phase shift is not correctly captured by the (M)IAB model. Instability will occur unless a staggered MoC grid is used [33].

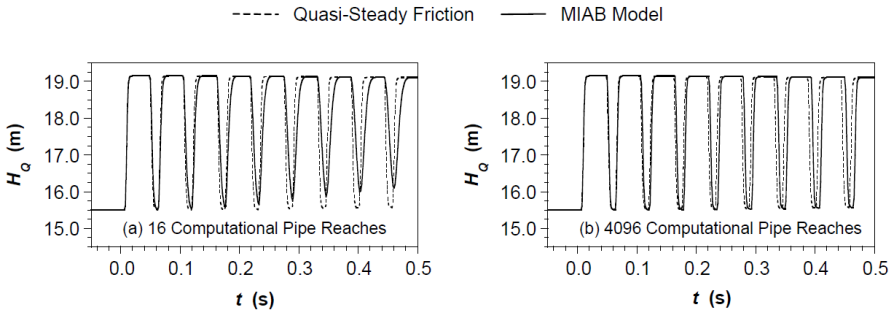

Figure 5.7: Damping introduced by the unsteady MIAB friction model decreases as a finer spatial discretization reduces the numeric error [34]

Frequency-dependent models

The first frequency-dependent model was developed by Zielke and is based on the analytical solution of unsteady laminar flow. The unsteady friction factor is found using past velocities and a weighting function. This flow history is expressed by the convolution integral given below [38]:

$$f_u = \frac{32\nu}{D\overline{v}|\overline{v}|}\int_0^t \frac{\partial \overline{v}}{\partial t}(u)W(t-u)\,du \tag{5.29}$$

in which ν is the dynamic viscosity, u the time used in the convolution integral and W a weighting function. W is a function of the dimensionless time τ_c,

$$\tau_c = \frac{\nu}{r^2}t \tag{5.30}$$

where r is the pipe radius. W may be calculated depending on the value of τ_c:

$$W(\tau_c) = e^{-26.3744\tau_c} + e^{-70.8493\tau_c} + e^{-135.0198\tau_c} + e^{-218.9216\tau_c} + e^{-322.5544\tau_c} \quad \tau_c > 0.02 \tag{5.31}$$

$$W(\tau_c) = 0.282095\tau_c^{-0.5} - 1.25 + 1.057855\tau_c^{0.5} + 0.9375\tau_c + 0.396696\tau_c^{1.5} - 0.351563\tau_c^{2} \quad \tau_c < 0.02. \tag{5.32}$$

Zielke's model has later been adapted by several authors to include turbulent flows [2]. While considering this unsteady friction model, it is important to realize it was developed with the analytical solution for pipe flow with stationary walls. It should therefore not be applied to annuli. One could consider applying it to pipe flow with moving walls if $\overline{v}$ is replaced with $\overline{v}_{rel}$. However, this is risky as accelerating pipe walls change the velocity profile in a different manner than acceleration of the flow does. The non-Newtonian fluid we are working with does not have a constant dynamic viscosity. Use of the plastic viscosity could be considered as an estimation, but the validity of this estimation is questionable as the effect of a non-constant viscosity on the fluids velocity profile is missed.

Relevance

Duan et al. studied the relevance on unsteady friction in pipe fluid transients [11]. They noted that real piping systems are an order larger than the systems used in laboratory experiments. The discrepancy between the steady and unsteady velocity profile exists only around the wave front where flow is unsteady. Its existence at any location behind the wave front is limited to the radial diffusion time. If the wave travel timescale (L/c) is of a similar order of magnitude, the flow is unsteady through out a significant portion of the system, as is often the case in experiments. Real systems have a much lower natural frequency meaning that the unsteady flow is a local effect, limited to the region behind the wave front, and often less important than the quasi-steady friction. Thus, it is likely that researchers have overestimated the significance of unsteady friction, a conclusion supported by several large scale field trials [21, 27]. This phenomenon is quantified by a dimensionless analysis which reveals that the influence of unsteady friction becomes insignificant if

$$\frac{fML}{D} \tag{5.33}$$

is of the order of 0.1 or larger. Here, f is the Darcy-Weisbach friction factor, M the Mach number, L the pipe length and D its diameter. This analysis is based on severe transients induced by sudden valve opening and closing. Duan et al. conclude that unsteady friction is unimportant for systems with less severe transients, even if the value of ratio 5.33 is smaller than 0.1[11].

Implementation

Unsteady friction is not included in the swab/surge model presented in this study. Its effect is most likely insignificant as the acceleration of fluid in MOD application is relatively low: the transients are not severe. In addition, ratio 5.33 is generally larger than 0.1. Its influence can therefore be ignored for engineering purposes.

5.3. Minor losses

5.3.1. Steady minor losses

Minor losses are local pressure drops which occur due to energy dissipation in the vortices which form behind changes in the pipe geometry such as changes in diameter or bends. Losses due to four different situations occur with in the system: abrupt expansions and contractions (Figure 5.8) and gradual expansions and contractions (Figure 5.9). The associated pressure drop is calculated according to:

$$\Delta p = \frac{1}{2}\rho \overline{v}_S^2 K \tag{5.34}$$

in which ρ is the fluid density, $\overline{v}_S$ the mean velocity in the small section, and K the minor loss coefficient. K is determined as follows:

$$\text{Abrupt expansion} \qquad K_{AE} = \left(1 - \frac{D_{h,S}^2}{D_{h,L}^2}\right)^2 \tag{5.35}$$

$$\text{Abrupt contraction} \qquad K_{AC} = 0.5\left(1 - \frac{D_{h,S}^2}{D_{h,L}^2}\right)^{\frac{3}{4}} \tag{5.36}$$

$$\text{Gradual expansion} \qquad K_{GE} = 2.6 \sin\frac{\phi}{2}\left(1 - \frac{D_{h,S}^2}{D_{h,L}^2}\right)^2 \tag{5.37}$$

$$\text{Gradual contraction} \qquad K_{GC} = \left\{ \begin{array}{ll} 0.8\sin\frac{\phi}{2}\left(1 - \frac{D_{h,S}^2}{D_{h,L}^2}\right)^{\frac{3}{4}} & \text{for } 0° < \phi < 45° \\ \frac{1}{2}\sqrt{\sin\frac{\phi}{2}}\left(1 - \frac{D_{h,S}^2}{D_{h,L}^2}\right)^{\frac{3}{4}} & \text{for } 45° < \phi < 180° \end{array} \right\} \tag{5.38}$$

Where $D_{h,S}$ is the hydraulic diameter of the small pipe section, $D_{h,L}$ is the hydraulic diameter of the large pipe section and ϕ is the angle with which the pipe gradually expands or contracts. These equations were derived for flow of a Newtonian fluid [16]. Using the ratio of hydraulic diameters is an acceptable approximation for non-circular conduits [3].

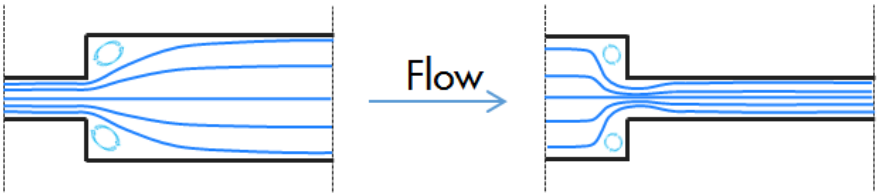

Figure 5.8: Abrupt expansion (left) and contraction (right)

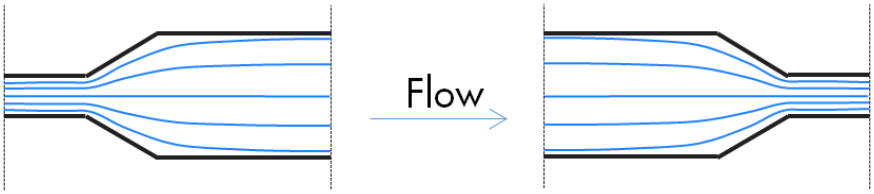

Figure 5.9: Gradual expansion (left) and contraction (right)

5.3.2. Unsteady minor losses

The above assumes flow is steady. During the transient process of tripping pipe flow is unsteady. The unsteadiness of orifice flow is still poorly understood as the resulting flow patterns are very complex. Literature on the subject is scarce and experimental work even more so. Two models are suggested in literature. Funk et al. introduced an instantanious interia based model and a frequency-dependent model was developed by Washio et al. in 1996. Experimental work shows that the steady models adequatly predict the pressure drop due to minor losses. Use of the unsteady models does not improve the prediction of the maginitude of the pressure drop and both fail to capture the observed phase delay between the measured pressure peaks and the peaks predicted by quasi-steady theory [17].

Inclusion of a complex unsteady minor loss formulation does not improve the accuracy of the model, and thus, the steady formulation described in the previous section is used.

6

Experimental design

"An experiment is a question which science poses to Nature, and a measurement is the recording of Nature's answer"
— Max Planck

6.1. Test philosophy

Data is vital, both to creating a better understanding and to validate models. Measurements of full-scale swab and surge events are rare, and non-existent for extremely low clearance liners. To obtain the desired data, an experiment is designed and executed at Shell's test rig in Rijswijk. The experiment is designed in order to:

1. Improve understanding of the phenomena governing swab and surge pressure (influence of velocity, acceleration, local losses, gel strength).
2. Determine the reliability of the model: do the assumptions still hold for narrow clearances and can we consistently predict the pressure accurately.
3. Check the robustness of the model (does it work for unusual movement, is it applicable if the assembly rotates, etc.).

The wall friction theory is already validated by comparing predictions to Burkhardt's field measurements (see Chapter 7). The results of this experiment are also presented in Chapter 7.

6.2. Experimental set up

Two experimental set ups are designed: one with a flush BHA and one with a local protrusion (cone) at the bottom of the BHA. The cone is included to locally restrict annular flow and allows the effect of local losses to be investigated. The dimensions given in Figure 6.1 are selected. The detailed description of the design considerations, safety issues, design constraints, component design and test plan are presented in Appendix E.

The dimensioning of the assembly is an iterative process, closely linked to the rheology and density of the drilling mud used to fill the test well. These two parameters, along with the tripping speed, which cannot exceed 300 mm/s, are most influential on the magnitude of the surge/swab pressure. A bentonine and water based mud is selected as it is a stable mixture; its properties should not vary significantly over the experiment's duration. The design properties are provided in Table 6.1.

Table 6.1: Design mud properties

Property	Value	Unit
Plastic viscosity (PV)	30	[cP]
Yield point (YP)	30	[$lb_f/100ft^2$]
Density (ρ)	1190	[kg/m^3]

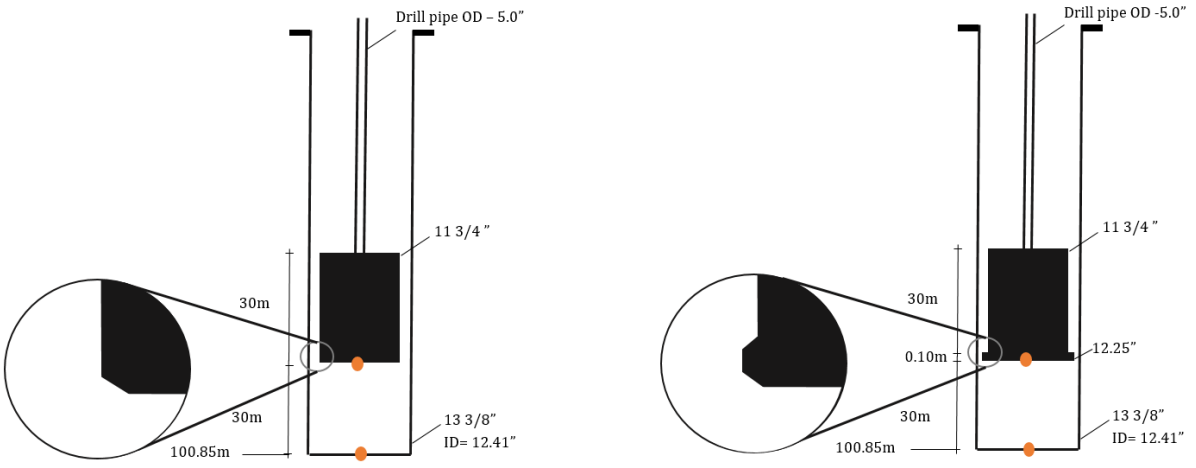

Figure 6.1: Schematic of experiment design. Flush assembly (left) and coned assembly on the right. Pressure sensor locations indicated in red

6.3. Test procedure

Once the pressure sensors and assembly are lowered into position and the hole is filled with mud, testing begins. Twenty-four movement are performed with each assembly. The movements consist of several different velocities and accelerations, see Figure 6.2, performed with different waiting times. Each movement is repeated with the goal of showing repeatability. The various movements and waiting times should allow the investigation of the influence of tripping speed, acceleration and gel strength on the pressure.

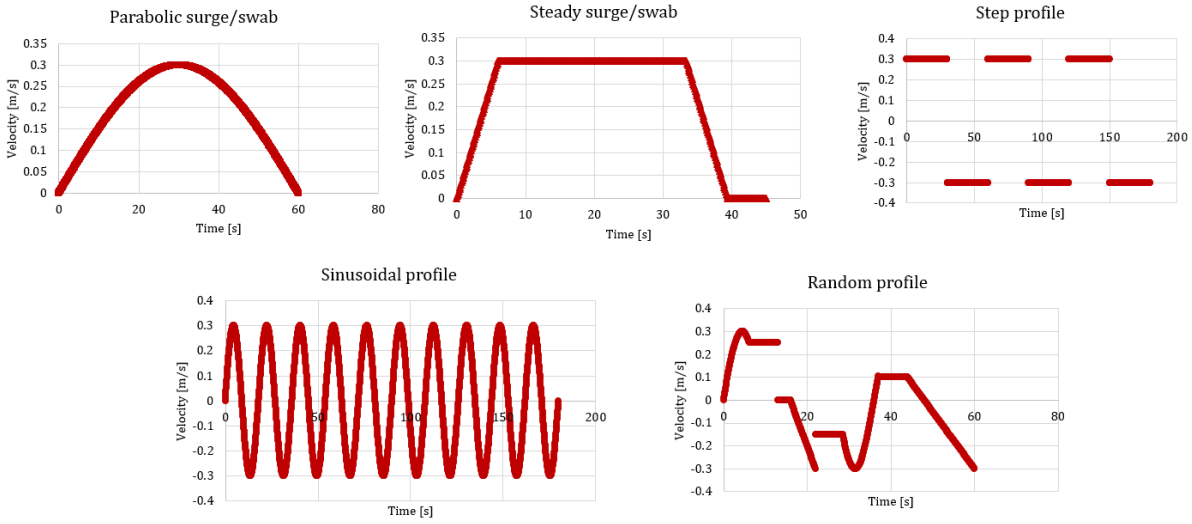

Figure 6.2: Proposed velocity profiles, performed at 2, 5, 10 or 15 minute intervals

The flush assembly is used first. This assembly is expected to induce lower pressures than the coned assembly and is therefore a safer candidate for the first run. Once all movements are performed the assembly is tripped out of the well. The pressure sensors are retrieved and the data transferred to a computer. After the cone is fixed to the assembly, it is run back into the well and the second set of movements is performed.

During each test, several mud samples are collected. The density and rheology of the sample are measured. Density is measured using a mud balance. The rheology is measured with a HAAKE MARS rheometer. The pressure is measured at 2 Hz using *AE sensors DLN 70* sensors. Top drive position and velocity are measured at 10 Hz.

6.4. Measurements and uncertainty

Before experimental results can be used to draw conclusions, the reliability of the data must be discussed. This is done through an uncertainty or error analysis. The goal of such an analysis is to quantify the range, or dispersion, of the value of a measurement or prediction. To structure such an analysis it is insightful to divide uncertainty into two categories [18].

1. **Aleatory -** uncertainty is associated with the randomness inherent to a system. It is thus a statistical uncertainty which, for example, arises from the noise in measurement data
2. **Epistemic -** uncertainty is attributed to a lack of knowledge. The influence of an unexpected or unknown process would result in epistemic uncertainty

6.4.1. Aleatory uncertainty

Quantification

This source of uncertainty is relatively straight foreward to quantify. Let's first distinguish between precise and accurate measurements. These two concepts are explained in Figure 6.3.

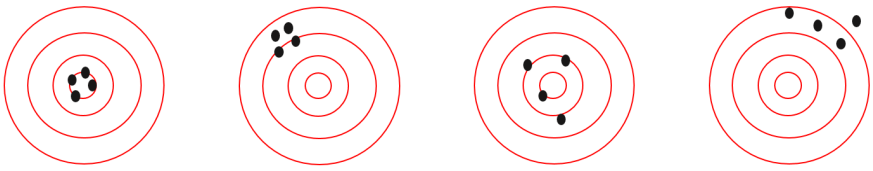

Figure 6.3: (a) High precision, high accuracy (b) high precision, low accuracy (c) low precision, high accuracy (d) low precision, low accuracy

All measurements are known to be precise. It is much harder to judge if they are accurate. Inaccuracy often stems from systematic errors. While measuring lengths it is fair to assume the measurement is accurate as it is extremely unlikely that the measuring tape or caliper gauge contains a systematic error. While measuring pressure, the presence of a systematic error is acceptable. The swab/surge pressure is the instantaneous deviation from the hydrostatic pressure. Any systematic error will cancel out. A systematic error in the rheology measurements is much harder to identify. The aleatory uncertainty is summarized in Table 6.2 and discussed in more detail in Appendix F.

Table 6.2: Measurement uncertainty

Measurement	Uncertainty	Unit
Pipe diameters	± 0.002	[m]
Pipe lengths	± 0.01	[m]
Pressure	± 0.7	[psi]
Mud density	± 0.1	[s.g.]
Rheology (shear rate)	± 0.01	[1/s]
Rheology (shear stress)	± 0.01	[Pa]
Top drive position	± 0.001	[m]
Top drive velocity	± 0.001	[m/s]

Uncertainty propagation

It is unlikely that all maximum or minimum extremes of the input parameters occur simultaneously. The overall uncertainty is therefore calculated as a root mean square. For example, considering a desired result $P = P(x_1^{e_1}, x_2^{e_2}, x_3^{e_3} + ...)$, then the overall uncertainty δP may be determined using the variables' uncertainty according to [37]

$$\delta P = P\left[\left(e_1\frac{\delta x_1}{x_1}\right)^2 + \left(e_2\frac{\delta x_2}{x_2}\right)^2 + \left(e_3\frac{\delta x_3}{x_3}\right)^2 + ...\right]^{0.5}. \tag{6.1}$$

6.4.2. Epistemic uncertainty

The question to be asked here is: are we measuring what we think we are measuring? Epistemic uncertainty arises from a lack of knowledge or data. The complexity of the problem demands that some simplifications be made. The resulting incomplete model causes an error in the predictions, since known physical processes are purposely neglected. In the following sections, sources of epistemic uncertainty and possible implications are discussed.

Rheology

While measuring the working fluid's rheology, time or temperature dependent behavior of the fluid is observed. Individual samples produce several rheology curves as is seen in Figure 6.4. The curve flattens with each measurement, suggesting that either loading history, or warming of the sample induces a gradual decrease in viscosity. The all measured samples produce very similar curves.

The 2 minute waiting time data is used, as this is the waiting time used for most runs. Calculations are performed with a 15% uncertainly range, this is the accuracy a lab technician can generally achieve [36]. The increase in viscosity at high shear rates is most likely due to the development of turbulence in the rheometer, these data points are discarded. The mud properties used for analysis are presented in Table 6.3. Appendix F contains a more detailed review of the rheology study.

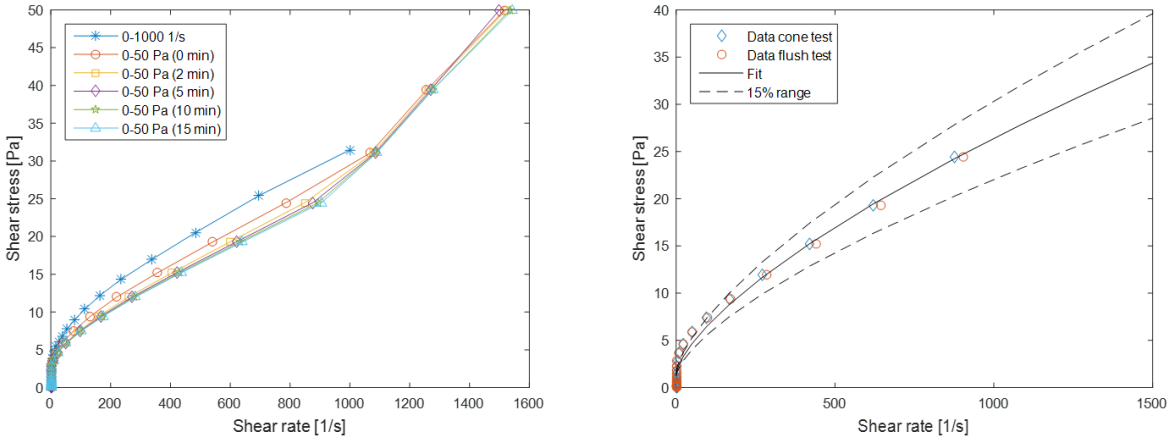

Figure 6.4: Rheology curves for the cone test mud sample (left) and the measurements, curve fit and uncertainty range used for calculation (right)

Table 6.3: Summary of the rheology study and the uncertainty

Property	-15%	Medium case	+15%
Plastic viscosity (PV) [cP]	17.0	20.0	23.0
Yield point (YP) [$lb_f/100ft^2$]	14.0	16.0	18.0
Yield stress (τ_y) [$lb_f/100ft^2$]	6.0	6.5	7.0

Varying mud level

As the assembly is tripped into the well, the drill string displaces drilling mud causing the mud level to rise. The assembly is perforated at the top to prevent it from being buoyant by allowing the mud enter the drillstring. This coupling between mud levels in the annulus and drillstring causes a variation in hydrostatic pressure which is not directly related to the assembly position, see Figure 6.5. The maximum and minimum hydrostatic pressure differ by 3 psi. The average hydrostatic pressure and atmospheric pressure are subtracted from the measured pressure.

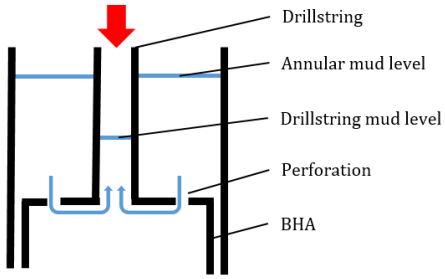

Figure 6.5: Variable mud level in the annulus due to displacement and coupling with the drill string mud level

Inner pipe eccentricity

As discussed in Chapter 5, eccentricity of the inner pipe can cause a significant reduction in the pressure drop. The pipe diameter ratio used in the experiment is outside the range of the regression model in Equation 5.27. CFD calculations are performed to qualtify the influence a fully eccentric inner pipe would have on the pressure drop for the highest steady tripping speed. The fluid's HB rheology is used. The results are summarized in Table 6.4, Appendix D contains a review of the CFD work. The flow is expected to be laminar.

Table 6.4: Summary of CFD results: pressure drop per meter and percent difference, v_p=0.34 m/s

Flow regime	Concentric [kPa/m]	Eccentric [kPa/m]	Percent difference [-]
Laminar	18.8	9.00	-52.1
Turbulent	18.8	11.7	-37.8

Pipe ovality

The host casing and assembly diameter are measured at several locations. Measuring the diameter of one cross-section in several directions reveals the pipes are somewhat oval. The diameter varies by a maximum of 2.0 mm over a cross-section. The ovality of the pipes is small relative to the diameter, but it has a relatively large effect on the clearance. The resulting cross section has a wide and narrow part (Figure 6.6), which like eccentricity, causes flow to encounter less resistance in the wide sections and more resistance in the narrow sections. The non-linear fluid behavior amplifes this effect. It is plausible that these effects average out, especially considering the two pipes move relative to each other. The uncertainty of the pipe diameter is included as aleatory uncertainty. However, one may argue this is incorrect as it is thus considered relative to the pipe diameter instead of to the clearance, which we know to be influenced by it.

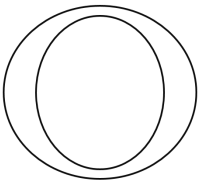

Figure 6.6: Presence of wide and narrow sections in a cross section due to ovality, exaggerated for clarity

Air bubbles

While filling the test well with the drilling mud, it mixed with the air causing it to foam. Mud samples taken from the top of the well had a density of 0.8-0.9 standard gravity. This means about 1/4 - 1/5 of the mud mixture is air by volume. Since the pressure drop is only developed over the assembly, these surface conditions do not influence the pressure drop. But if the mud around, and especially below the assembly, contains a lot of dissolved gas or some gas bubbles, then this may very well influence the pressure drop. The dissolved gas could come out of solution if the pressure decreases significantly as occurs during swabbing. Small gas bubbles may compress if additional pressure is applied as occurs during surges. This would mean the bulk modulus of the fluid is much lower then assumed.

7

Results & discussion

7.1. Validation with Burkhardt's field test

7.1.1. Results

In 1961, Burkhardt performed a field test designed specifically to measure surge/swab pressures. The data allows for an insightful comparison between the predictions by the model and the measured data.

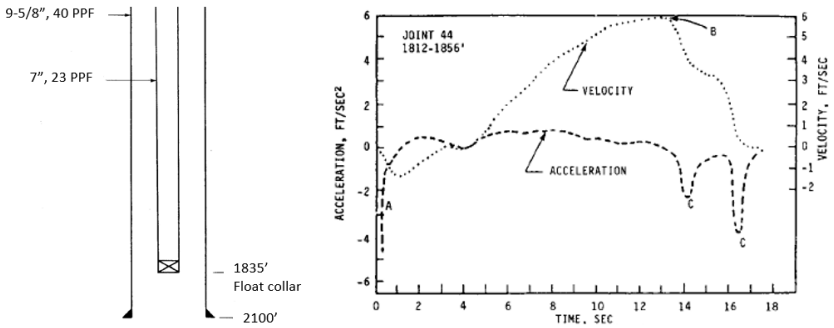

Figure 7.1: Wellbore geometry and string movement for joint number 44 in Burkhardt's 1961 field trial [5]

A 9-5/8", 40 lb/ft casing was set and cemented to form a wellbore, its ID is 8.83". A 7", 23 lb/ft casing was run into the hole (Figure 7.1). The wellbore was filled with a 10.8 lb_m/gal water based mud with a plastic viscosity of 12 cP and a yield point of 7 $lb_f/100ft^2$. Pressure fluctuations were recordered along with the casing string's movement [5]. The results of validation are plotted in Figure 7.2.

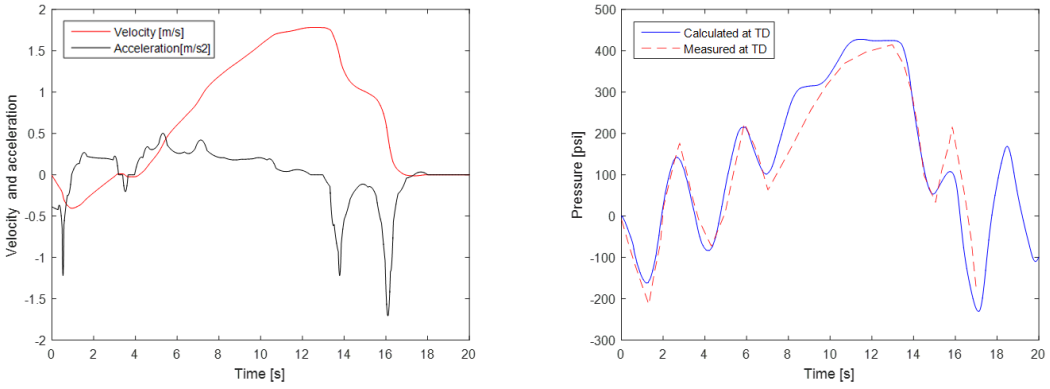

Figure 7.2: Velocity profile used (left) and the comparison of the measured and predicted swab/surge pressures (right) [5]

7.1.2. Discussion

The model captures the dynamic pressure oscillations reasonably well and matches the peak pressure within 3%. The pressure oscillations occurring within the first few seconds are inertial. They dampen out and the mud reaches an almost steady velocity at 13 s during which the peak pressure is observed. Breaking then decelerates the fluid and inertial oscillations are once again observed.

The good match between measurement and prediction most likely confirms that the influence of unsteady friction on the total pressure drop is indeed small. The peak at 16 s is not captured as well as the other. This is where the fluid's velocity profile encounters the largest distortion due to acceleration. This means unsteady friction would have largest impact here, which could explain the relatively large discrepancy between data and prediction.

The accuracy of the calculated results between 11 and 13 s means that the non-Newtonian quasi-steady friction model and the use of the clinging constant produce reliable results in steady conditions. The match between predictions and measurements is excellent considering that errors in friction factor predictions of 10% are the norm rather than an exception [37]. In fact, ignoring the clinging constant severely underestimates the peak pressure. The same holds for the use of laminar velocity profiles. The later is to be expected since the flow becomes turbulent after roughly 8 s.

Comparing the model to Burkhardt's measurements serves as a good validation of the model. However, this validation is limited due to the following points:

1. This is the only data presented by Burkhardt, we therefore do not know if swab/surge pressures are consistently this predictable.
2. The clearance between wellbore and liner is relavitely large is this test. Do the assumptions still hold for narrow clearance liners such as applied during MOD?
3. The shallow well and short bottom hole section mean that fluid is nearly perfectly displaced by the casing string. The influence of fluid compressibility and wellbore elasticity is negligible.

7.2. Validation Clark and Fontenot's field test

7.2.1. Results

Clark and Fontenot performed a set of field tests in a deep well and published their measurements in 1974, [8]. Their work allow us to confirm the effect of fluid compressibility and wellbore elasticity.

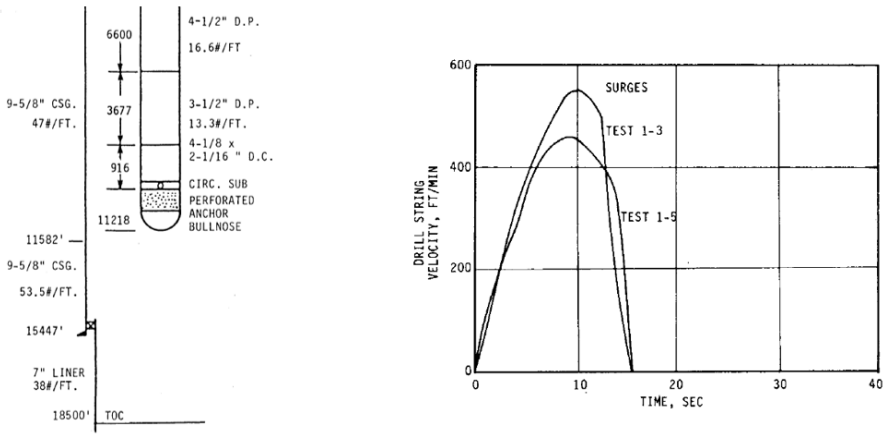

Figure 7.3: Wellbore geometry and string movement for the first test series in the Mississippi well [8]

As depicted in Figure 7.3, a 7" liner was set and cemented below a 9-5/8" casing to form a wellbore. A drillstring, composed of several sections of drill pipe and collars was run into the hole, see Figure 7.3. An oil based drilling mud with a plastic viscosity of 88 cP, a yield point of 34 $lb_f/100ft^2$, and a yield stress of 9 $lb_f/100\ ft^2$ was used. Its density was 17.5 lb_m/gal. Pressure was recorded by a sensor placed in the bullnose at the end of the drillstring [8]. The results of the validation are plotted in Figure 7.4.

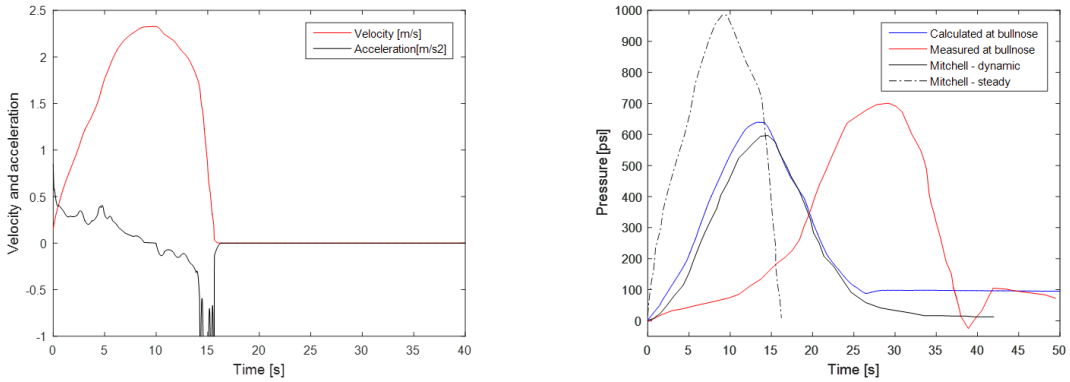

Figure 7.4: Velocity profile used (left) and the comparison of the measured and predicted swab/surge pressures (right) [8, 22]

7.2.2. Discussion

The qualitative shape of the surge pressure profile is well matched and the maximum pressure is predicted within 7% of the measured value. However, the predicted pressure peak occurs about 20 seconds before the measured peak. Mitchell concludes that the time axis is miscorrelated [22]. The long interval of compressible fluid and deformable wellbore below the assembly allows some of the fluid displacement to be balanced by storage. The importance of including this effect is evident from a steady state calculation performed by Mitchell. Steady state calculations do not include fluid compression and wellbore expansion; all fluid is perfectly displaced upwards, and thus the maximum surge pressure is overpredicted by roughly 40%. The accuracy of a steady state calculation decrease as well depth increases. The predictions by the model developed in this study are very similar to Mitchell's results. The gain in accuracy of the peak pressure prediction is due to the improved rheology model. Mitchell treats drilling mud as a PL fluid. The non-zero surge pressure from 25 s onward is due to the yield stress of the fluid. The slow dissipation of this residual pressure, as seen in the measurements, is not predicted. Inertial oscillations are not nearly as extreme as observed in Burkhardt's test: viscous forces are dominant in this deep well filled with a more viscous mud.

7.3. Experiment on the Rijswijk test rig

The experiment is performed to learn more about the effect of small clearances and local flow restriction, as well the consistency of surge/swab predictions. Instead of showing the results of all 48 movements performed during the experiment, a few insightful runs, which are considered representative of the results, will be discussed. The full set of results can be found in Appendix G.

7.3.1. Results flush assembly

Some results for the flush assembly are given below. The step profile at high speed (Figure 7.5), step profile at low speed (Figure 7.6), and random profile (Figure 7.7) are presented.

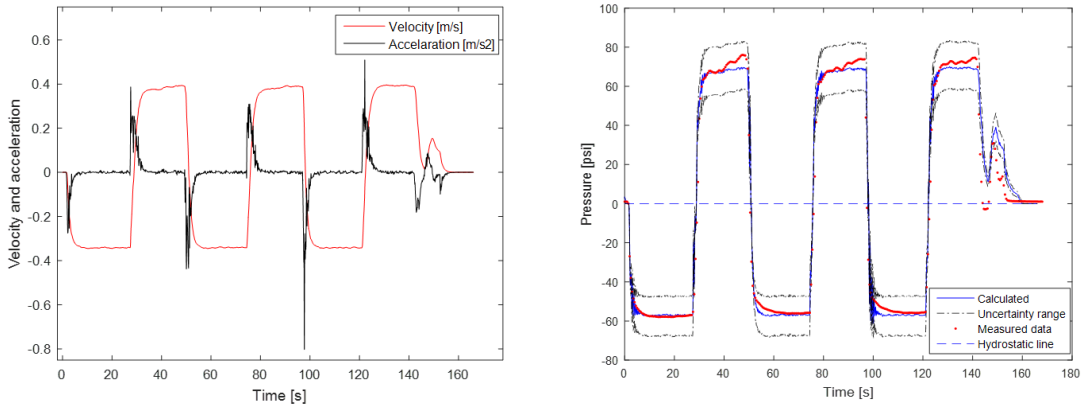

Figure 7.5: Flush assembly movement No. 5: velocity profile (left) measured and predicted swab/surge pressure with the range of aleatory and rheology uncertainty (right)

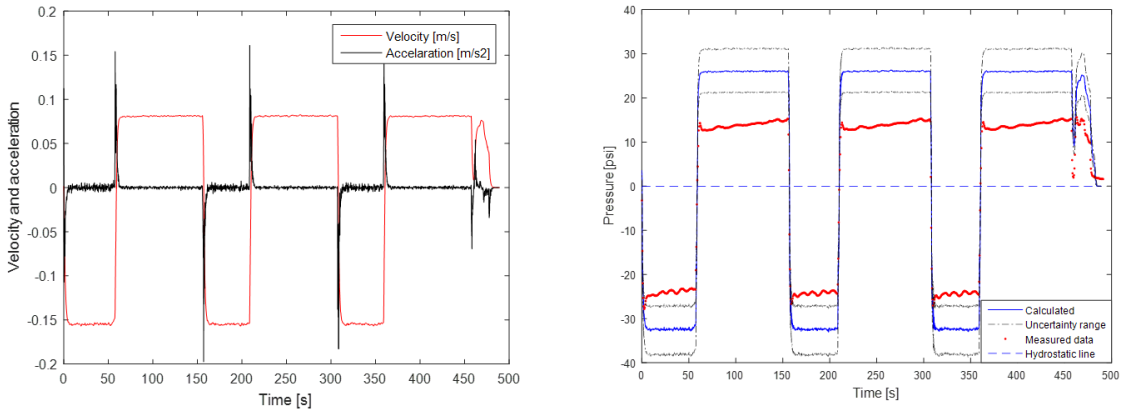

Figure 7.6: Flush assembly movement No. 7: velocity profile (left) measured and predicted swab/surge pressure with the range of aleatory and rheology uncertainty (right)

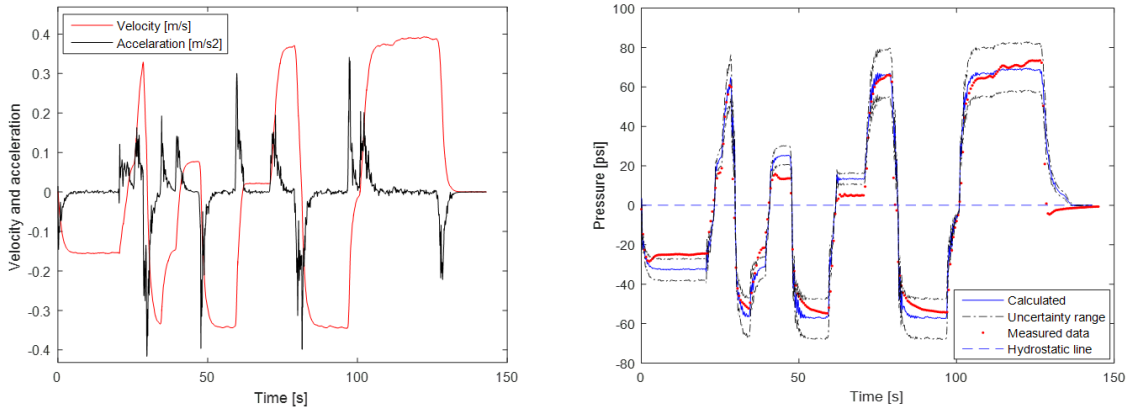

Figure 7.7: Flush assembly movement No. 9: velocity profile (left) measured and predicted swab/surge pressure with the range of aleatory and rheology uncertainty (right)

7.3.2. Discussion flush assembly

The experiment is considered a success. Obtaining good quality data is not trivial and the results enhance our understanding. The shape of the pressure fluctuations is well captured and seems to be dependent on the instantaneous velocity only. The acceleration has no noticeable effect as the relatively harsh acceleration applied with the step profiles (Figures 7.6, 7.7) do not result in additional swab/surge pressure. The mud's gel strength did not increase with waiting time. Its influence cannot be determined from this test. The most concerning observation is that the swab/surge is overestimated significantly at low tripping speeds as is evident in Figures 7.6 and 7.7. The plotted uncertainty range is aleatory. Therefore, if a measurement falls outside of this range, some process is not well modeled and the error is epistemic, or the aleatory uncertainty is poorly captured. The later is considered less likely. Three possible explanations are identified and discussed in order of likely hood.

Pipe ovality

As discussed, the ovality of the pipes results in wide and narrow sections, influencing the pressure drop in the same manner as eccentricity does. During speeds of 0.1 m/s, the shear rate at the wall is on the order of 500 s^{-1}, still in the shear thinning regime. This non-linearity may cause a lower pressure drop than expected. This is the same process which causes eccentricity to have a larger effect on shear thinning fluids than on Newtonian fluids. During the faster trips, the shear rate increases to the order of 2000 s^{-1}. At this point the viscosity is shear rate independent and equal to the plastic viscosity. The more linear fluid behavior may well cause flow to be distributed more evenly over the cross-section, so that the assumption of circular pipes is satisfied. This could explain the gradual increase in prediction accuracy with increasing tripping speed.

System sensitivity

A second possible explanation for the error is that it is chance which causes the predictions to match well at the high speeds. The system is very sensitive to the size of clearance. The relative uncertainty on the pipe diameters is small (< 1%) , yet it is large on the clearance (≈ 10%). Changing the clearance size by ±10% changes the peak pressure by -18% and +25%. The pipe diameter were only measured at four different locations, more measurements might have yielded different average pipe diameters and thus a very different predicted pressure.

Eccentricity

As shown in Table 6.4, eccentricity of the inner pipe may reduce the pressure drop by 50%. This makes it a plausible explanation for the over-prediction of the swab/surge pressure. However, extensive thought experiments, confirmed with CFD work, indicate that there is no simple reason for why the inner pipe would always be eccentric at low speeds and then center as the pipe speeds up. The pressure is constant over the cross section. Entrance effects do apply a moment on the pipe but it is too small to significantly move the pipe. More complex fluid structure interaction may cause the pipe to centralize itself. However, these interactions are too complex to simulate. Due to the lack of proof for a centering mechanism we cannot rely on eccentricity to explain the error. The CFD work is presented in Appendix D.

7.3.3. Results coned assembly

Below the results of three movements of the coned assembly are shown. The parabolic profile (Figure 7.8), step profile at low speed (Figure 7.9), and random profile (Figure 7.10) are presented.

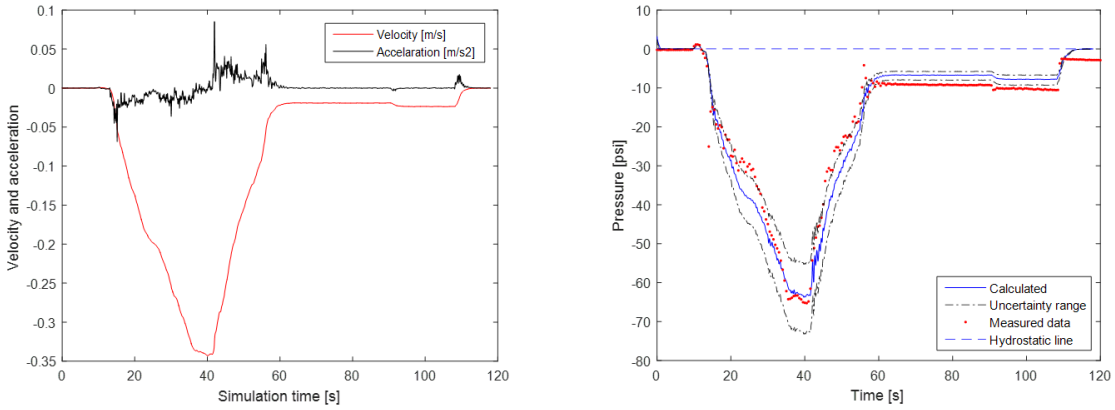

Figure 7.8: Coned assembly movement No. 01: velocity profile (left) measured and predicted swab/surge pressure with the range of aleatory and rheology uncertainty (right)

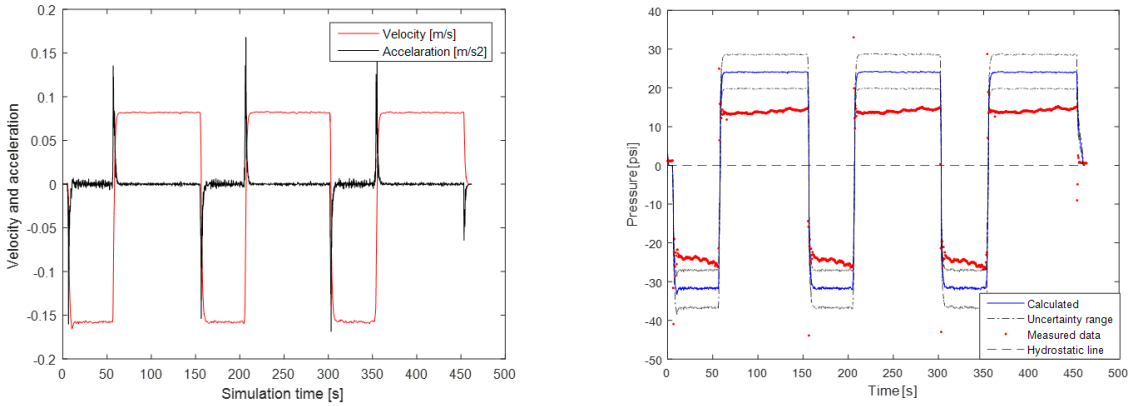

Figure 7.9: Coned assembly movement No. 07: velocity profile (left) measured and predicted swab/surge pressure with the range of aleatory and rheology uncertainty (right)

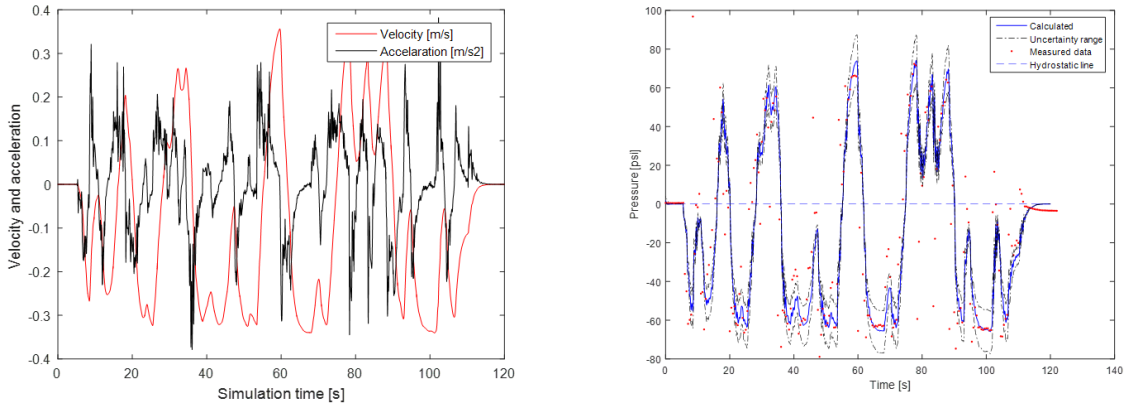

Figure 7.10: Coned assembly movement No. 09: velocity profile (left) measured and predicted swab/surge pressure with the range of aleatory and rheology uncertainty (right)

7.3.4. Discussion coned assembly

As is the case for the flush assembly, the pressure is overestimated at low tripping speeds. This supports the claim that eccentricity is not (the only) factor to explain it. The cone prohibits the assembly from reaching a fully eccentric position. As long as the acceleration is gentle, the pressure profile still follows the velocity profile, Figure 7.8. When harsh accelerations are applied (Figures 7.9 and 7.10), pressure peaks are observed. These peaks are not observed for a single run of the flush assembly but appear consistently for sudden movement of the coned BHA. This means that the local flow restriction by the cone induces transient pressures. These pressures are not predicted by the unsteady energy equation which is used to model flow around the cone and are not mentioned in literature on swab and surge pressures. The flow around this complex geometry is likely to require a more advanced method of solving flow, taking into its 2D or even 3D nature as well as the fluid's compressiblity. The quasi-steady assumption for the minor and major losses may also be a cause. In addition, the minor losses are determined based on equations derived for Newtonian fluids, the non-linear rheology might cause a discrepancy between measurement and prediction.

7.3.5. Rijswijk experiment discussion summary

The most significant lesson learned from this experiment is that the pressures developed during the running of narrow clearance liners are very difficult to predict, much more so than pressures under conventional conditions. This is because the pressures are quite sensitive to the size of the clearance. The uncertainty of the clearance size is large due to the imperfect pipes. Attempting to predict surge/swab pressures accurately is very difficult and any calculation should be treated with care.

The second important lesson is that the transients around the cone are not well predicted. The acceleration induced pressure peaks are a local effect and will not increase as the liner length increases. Their contribution to the total swab/surge pressure will therefore decrease as liner length increases and render them insignificant at actual assembly lengths. Their effect will further decrease as the longitudinal elasticity of the drill string will reduce the magnitude of the acceleration of the cone at critical depths. The observation is however very relevant to the work on cone pop-out. The same theory is used to predict the swab pressures in those models and it is clearly not predicting the correct pressure envelope.

7.4. Application - Casestudy

8

Conclusion & recommendations

"Science is always wrong, it never solves a problem without creating ten more."
— George Shaw

8.1. Conclusions

This thesis presents a model capable of predicting downhole surge/swab pressures induced by (MOD) assembly movement. 1D CFD is used: the continuity and momentum equations are solved throughout the wellbore using the method of characteristics considering a slightly compressible fluid in a conduit with linearly elastic walls. Flow at the bottom and top of the expandable BHA is solved using a linearized energy equation approach along with balance of mass. The influence of drillstring and BHA movement is accounted for through friction, mass sources and mass sinks. See Chapter 4.

The model is validated by comparing its predictions to the measurements made by Burkhardt during his 1961 field test, see Section 7.1. The model is judged to perform well. The peak pressure is captured with an error of 3% and inertial pressure oscillations are adequately predicted (Figure 7.2). The effect of fluid compression and wellbore expansion is validated with data collected by Clark and Fontenot. A transient calculation is required as a steady state calculation overestimates the surge pressure by 40%. The predictions match the measurements within 7% as can be seen in Figure 7.4.The most significant improvement compared to existing models is the use of a clinging constant accurate for both laminar and turbulent flows, which had previously not been available. The clinging constant approach is computationally much faster than the commonly used velocity profile approach. It is also accurate for small inner to outer pipe diameter ratios; the velocity profile approach is not (Chapter 5). This is the first fully dynamic model considering a Herschel-Bulkey mud rheology.

The validity of the model under MOD conditions is addressed next. The influence of an extremely small clearance between host casing and assembly on the pressure development is assessed through a full-scale experiment performed with Shell's Rijswijk test rig, see Section 7.3. While running a flush assembly, the surge/swab pressures are predictable and dependent on the instantaneous velocity as accelerations were limited and fluid displacement near perfect due to the limited well depth. If a cone is attached to the assembly, acceleration induced transients are measured but not predicted. The 1D assumption and associated overly simplistic equations describing flow around the cone, the quasi-steady assumption, and non-Newtonian fluid behavior are identified as possible causes. The pressures caused by low tripping speeds are systematically over predicted for both assembly configurations. The relatively large uncertainty of the size of the clearance and the slightly oval shape of the pipes are believed to be the causes rather than a modeling error.

Casestudy

8.2. Recommendations for future work

Future work should first focus on eliminating not understood sources of error as most risk is concentrated here. Secondly the model should be improved by increasing its complexity and flexibility.

The most pressing problem is understanding the acceleration induced pressures formed around the cone during the experiment. As it is a local effect, its relative contribution to the total pressure drop decreases as assembly length increases. It is therefore not expected to be of critical importance to surge/swab calculations for running assemblies. However, the swab pressures resulting from cone pop-out, are expected to be influenced significantly by this process. Cone-pop out is a local effect, with much higher accelerations, and flow over the cone is solved using the same theory as used in this study [30, 32]. Capturing the transient pressures generated at the cone is therefore vital for cone pop out induced swab pressure predictions. Modeling flow over the cone in 2D and including the movement of the cone is the recommended starting point. Validity of the quasi-steady assumption and effect non-Newtonian fluid behavior should also be investigated.

More work should be done to verify the author's conclusion on the cause of the over prediction of the swab/surge pressure which occurred during the experiment. Advanced CFD software may be used to investigate the effect of the pipes' oval shape on the frictional drop at high and low speeds. A more controlled, small scale experiment may also be performed to this end. We should confirm that the over prediction is not due to a fundamental mistake in the modeling but rather due to an unmodeled phenomenon.

The model may also be improved upon by incorporating some additional processes. The longitudinal elasticity of the drillstring should be included. Drilling mud properties are temperature dependent and should thus be varied accordingly over the various fluid sections. The effect of formation porosity should be investigated and a pressure dependent leak-off term may be included in the continuity equation for uncased well sections.

The flow, and associated losses, in the toolstring, the section of drillstring just above the cone, should be modeled with a finer discretization. The fairly rough approach taken in this thesis will yield the correct order of magnitude of the minor losses. Work by Tillema demonstrates the importance of correctly modeling the interface geometry [30].

The model should be upgraded so that input may be changed by means of a convenient user interface. Currently, adding fluid regions or changing the interface geometries and associated minor losses is a painstaking task.

More research is required into the field of unsteady friction. The (M)IAB model for unsteady friction is thought to be unreliable, this must be conclusively proven or disproven. The effect of an annular configuration and non-Newtonian rheology on the convolution integral solution should be investigated. The application of 1D unsteady friction models extends far beyond hydrocarbon well engineering.

Bibliography

[1] API. *Rheology and hydraulics of oil-well fluids*. American Petroleum Institute, recommended practice 13d edition, 2010.

[2] A. Bergant, A. Simpson, and J. Vitkovsky. Developments in unsteady pipe flow friction modelling. *Journal of Hydraulic Engineering*, Vol. 39, No. 3:249–257, 2001.

[3] R.D. Blevins. *Applied Fluid Dynamics Handbook*. Krieger Publishing Compay, Malabar, 1 edition, 1992. ISBN 0-89464-717-2.

[4] B. Brunone, B.W.Karney, M. Mecarelli, and M. Ferrante. Velocity profiles and unsteady pipe friction in transient flow. *Journal of Water Resources Planning and Management*, Vol. 126, No. 4:236–244, 2000.

[5] J.A. Burkhardt. Wellbore pressure surges produced by pipe movement. *Society of Petroleum Engineers*, 10.2118/1546-G-PA:595–605, 1961.

[6] M. Chaudhry. *Applied Hydraulic transients*. Springer, Delft, 3 edition, 2014. ISBN 978-1-4614-8537-7.

[7] E.H. Clark. Bottom hole pressure surges whule running pipe. *The Petroleum Engineer*, pages B68–B96, 1955.

[8] R.K. Clark and J.E. Fontenot. Field measurements of the effects of drillstring velocity, pump speed, and lost circulation material on downhole pressures. *Society of Petroleum Engineers*, Presented at the annual SPE meeting, 1974.

[9] F. Crespo and R. Ahmed. A simplified surge and swab pressure model for yield power law fluids. *Journal of Petroleum Science and Engineering*, 101:12–20, 2012.

[10] D.W. Dodge and A.B. Metzner. Turbulent flow of non-newtonian systems. *AIChE J.*, pages 189–204, 1959.

[11] H.F. Duan, M.S. Ghidaoui, P.J. Lee, and Y.K. Tung. Relevance of unsteady friction to pipe size and length in pipe fluid transients. *Journal of Hydraulic Engineering*, Vol. 138, No. 2:154–166, 2012.

[12] J.E. Fontenot and R.K. Clark. An improved method for calculating swab and surge pressures and circulating pressures in a drilling well. *Society of Petroleum Engineers*, 10.2118/4521-PA:451–462, 1974.

[13] G.W. Govier. *Flow of Complex Mixtures in Pipes*. Van Nostrand Reinhold Ltd., New York, 1 edition, 1972.

[14] A.S. Halal and R.F. Mitchell. Casing design for trapped annular pressure buildup. *SPE Drilling & Completion*, June SPEDC 25694:107–110, 1994.

[15] A.S. Halal, M. Wicks, H.F. Wedelich, and V.A. Dunayevsky. Dynamic and steady state swab/surge pressure prediction. *Shell internal document*, pages 21–24, 1999.

[16] I.E. Idelchik. *Handbook of Hydraulic Resistance*. Jaico Publishing House, 3 edition, 2005.

[17] Y. Kim, A.R. Simpson, and M.F. Lambert. The effect of orifices and blockages on unsteady pipe flows. *World Environmental and Water Resources Congress: restoring our natural habitat*, 2007.

[18] A. Kiureghian and O. Ditlevsen. Aleatory or epistemic? does it matter? *Structural Safety*, Vol. 31 Is. 2: 105–112, 2009.

[19] M. Lal. Surge and swab pressure modeling for dynamc pressures and safe trip velocities. *IADC/Society of Petroleum Engineers*, 10.2118/11412-MS:427–433, 1983.

[20] A. Lubinski, F.H. Hsu, and K.G. Nolte. Transient pressure surges due to pipe movement in an oil well. *Oil & Gas Science and Technology*, Rev. IFP 32:307, 1961.

[21] D. McInnes and B.W. Karney. Transients in distribution networks: Field tests and demand models. *Journal of Hydraulic Engineering*, Vol. 126, No. 10:218–231, 1995.

[22] R.F. Mitchell. Dynamic surge/swab pressure predictions. *Society of Petroleum Engineers*, 10.2118/16156-PA:325–330, 1988.

[23] U. Mme and P. Skalle. Effects of mud properties, hole size, drill string tripping speed and configurations on swab and surge pressure magnitude during drilling operations. *International Journal of Petroleum Science and Technology*, 6:143–152, 2012.

[24] I. Posthof. A turbulent approach to unsteady friction. *Journal of Hydraulic research*, Vol. 46 No. 5:679–690, 2008.

[25] M.C. Potter. Stabilty of plance couette-poiseuille flow. *Journal of Fluid Mechanics*, vol. 24 part 3:609–619, 1966.

[26] B.W. Roberts. Unsteady incompressible flow through hydraulic systems. *Proc Inst Mech Engrs*, Vol 181 Pt 3A, 1967.

[27] M. Stephens, A.R. Simpson, M.F. Lambert, and J.P. Vitkovsky. Field measurements of unsteady friction effects in a trunk transmission pipeline. *Proc. 7th Annual symp. on Water Distribution Systems Analysis*, ASCE:1–18, 2005.

[28] M. Tang, R. Ahmed, R. Srivastav, and S. He. Simpliefied surge pressure model for yield power law fluid in eccentric annuli. *Journal of Petroleum Science and Engineering*, 145:346–356, 2016.

[29] A.S. Tijsseling and A. Bergant. Meshless compution of water hammer. *Department of Mathematics and Computer Science, Eindhoven University of Technology, The Netherlands*, pages 69–70, 2007.

[30] H.A.M. Tillema. Measuring swab pressure due to cone pop-out. *TU Delft*, 2015.

[31] S.P. Timoshenko and J.N. Goodier. *Theory of Elasticity*. McGraw-Hill Book Co Inc., New York City, 1 edition, 1951.

[32] J.W. van Dongen. Swab pressure due to cone pop-out. *TU Delft*, 2015.

[33] J. Vitkovsky, M. Lambert, A. Simpson, and A. Bergant. Advances in unsteady friction modelling in transient pipe flow. *The 8th International Conference on Pressure Surges*, BHR, The Hague, The Netherlands: 12–14 April, 2000.

[34] J. Vitkovsky, A. Bergant, A. Simpson, and M. Lambert. Systematic evaluation of one-dimensional unsteady friction models in simple pipelines. *Journal of Hydraulic Engineering*, Vol. 132, No. 7:696–708, 2006.

[35] C. Vuik, P. van Beek, F. Vermolen, and J. van Kan. *Numerieke Methoden voor Differentiaalvergelijkingen*. VSSD, 1 edition, 2006.

[36] J. Wentink. Personal communication. *Shell Rijswijk, wells R&D*, 2017.

[37] F.M. WHite. *Fluid mechanics*. McGraw-hill Compaies, Inc, New York, 7 edition, 2009. ISBN 978-0-070352934-9.

[38] W. Zielke. Frequency-dependent friction in transient pipe flow. *ASME Journal of Basic Engineering*, Vol. 91, No. 4, 1969.

A

Continuity and momentum equations for fluid flow in pipes

Fluid flow in closed conduits is described by the conservation of mass and conservation of momentum equations. These are often referred to as the continuity and momentum equations. In this appendix these equations will be derived for a control volume [6].

A.1. Continuity Equation

The continuity equation is derived by ensuring conservation of mass over a control volume. A slightly compressible fluid is considered in a conduit with linearly elastic walls. Flow in only one dimension is considered, i.e. radial and circumferential flow due to expansion or contraction of the conduit is negligible. The effect of radial expansion and contraction is considered.

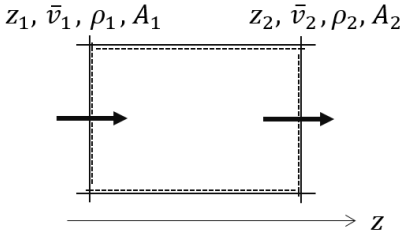

Figure A.1: Control volume

Conservation of mass dictates that the rate of change of mass within the control volume is equal to the net flux of mass over the control volume. Using the Reynolds transport theorem [1], this condition is fulfilled for a stationary control volume in the equation below, in which ρ, A, $\overline{v}$ are the fluid density, cross-sectional area of the conduit, and fluid velocity respectively.

$$\frac{d}{dt}\int_{z_1}^{z_2} \rho A dz + \rho_2 A_2 \overline{v}_2 - \rho_1 A_1 \overline{v}_1 = 0 \tag{A.1}$$

Applying Leipnitz's rule [2] to the first term results in:

$$\int_{z_1}^{z_2} \frac{d}{dt}\rho A dz + \rho_2 A_2 \frac{dz_2}{dt} - \rho_1 A_1 \frac{dz_1}{dt} + \rho_2 A_2 \overline{v}_2 - \rho_1 A_1 \overline{v}_1 = 0, \tag{A.2}$$

working with a stationary control volume, $\frac{dz_1}{dt}$ and $\frac{dz_2}{dt}$ are zero. The equation may be simplified to:

$$\int_{z_1}^{z_2} \frac{d}{dt}(\rho A) dz + (\rho A \overline{v})_2 - (\rho A \overline{v})_1 = 0. \tag{A.3}$$

[1] Reynold's transport theorem states that: $\frac{dB_{sys}}{dt} = \frac{d}{dt}\int_{cv} \beta\rho dA + \left[\beta\rho A(V-W)\right]_{OUT} - \left[\beta\rho A(V-W)\right]_{IN}$; in this case $\beta = 1$ and $B = Mass$

[2] Leipnitz's rule: $\frac{d}{dt}\int_{f_1(t)}^{f_2(t)} F(x,t)dx = \int_{f_1(t)}^{f_2(t)} \frac{\partial}{\partial t}F(x,t)dx + F(f_2(t),t)\frac{\partial f_2}{\partial t} - F(f_1(t),t)\frac{\partial f_1}{\partial t}$

The mean value theorem [3] is now applied

$$\frac{\partial}{\partial t}(\rho A)\Delta z + (\rho A\overline{v})_2 - (\rho A\overline{v})_1 = 0. \tag{A.4}$$

in which $\Delta z = z_2 - z_1$. Dividing through Δz and letting it approach zero we obtain:

$$\frac{\partial}{\partial t}(\rho A) + \frac{\partial}{\partial z}(\rho A\overline{v}) = 0. \tag{A.5}$$

Expansion of the partial derivatives leads to:

$$A\frac{\partial \rho}{\partial t} + \rho\frac{\partial A}{\partial t} + \rho A\frac{\partial \overline{v}}{\partial z} + \rho\overline{v}\frac{\partial A}{\partial z} + A\overline{v}\frac{\partial \rho}{\partial z} = 0. \tag{A.6}$$

Using the expression for material derivative in one spacial dimension ($\frac{df}{dt} = \frac{\partial f}{\partial t} + v\frac{\partial f}{\partial z}$)

$$A\frac{d\rho}{dt} + \rho\frac{dA}{dt} + \rho A\frac{\partial \overline{v}}{\partial z} = 0 \tag{A.7}$$

now we divide by ρA:

$$\frac{1}{\rho}\frac{d\rho}{dt} + \frac{1}{A}\frac{dA}{dt} + \frac{\partial \overline{v}}{\partial z} = 0. \tag{A.8}$$

The equation's three terms now illustrate the governing process: the first term accounts for compressibility of the fluid, the second term accounts for radial expansion/contraction of the conduit and the third term accounts for the in-and-out flow of the fluid. At this point it should be realized that radial expansion/contraction, i.e. the change in cross-sectional area, varies with pressure. Using the chain rule we can write

$$\frac{1}{\rho}\frac{d\rho}{dp}\frac{dp}{dt} + \frac{1}{A}\frac{dA}{dp}\frac{dp}{dt} + \frac{\partial \overline{v}}{\partial z} = 0. \tag{A.9}$$

Pressure rather then density is the variable of interest in this thesis. The following relationship, $K = \rho\frac{dp}{d\rho}$, and rearranging yields

$$\left(\frac{1}{K} + \frac{1}{A}\frac{dA}{dp}\right)\frac{dp}{dt} + \frac{\partial \overline{v}}{\partial z} = 0. \tag{A.10}$$

Equation A.10 is in accordance to Mitchell's equation [22]. However, it is preferable to express all terms in pressure and velocity. We therefore define a variable c with the following expression:

$$\rho c^2 = \frac{1}{\left(\frac{1}{K} + \frac{1}{A}\frac{dA}{dp}\right)} \tag{A.11}$$

here the variable c is the undamped speed at which a pressure wave travels in the fluid. Using this expression an expanding the total derivatives results in the continuity equation.

$$\frac{\partial p}{\partial t} + \overline{v}\frac{\partial p}{\partial z} + \rho c^2\frac{\partial \overline{v}}{\partial z} = 0 \tag{A.12}$$

[3] The mean value theorem: $\int_{x_1}^{x_2} F(x)dx = (x_2 - x_1)F(\zeta)$ where $x_1 < \zeta < x_2$

A.2. Conservation of momentum

In this section, the conservation of momentum equation is derived for the control volume. This is done by applying Newtons second law on the control volume.

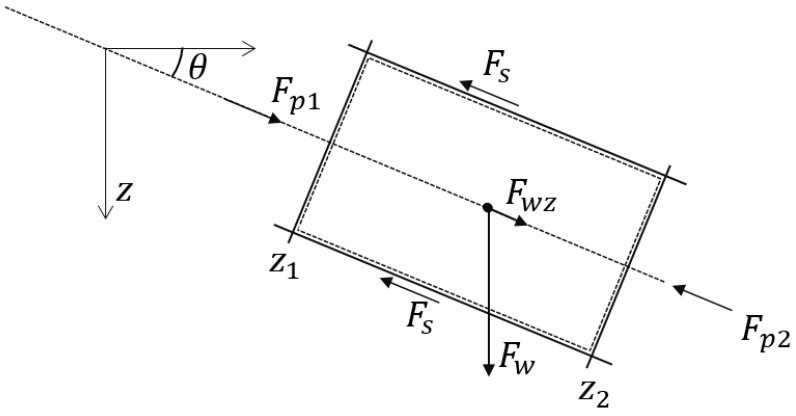

Figure A.2: Forces acting on the control volume

Newton's second law states the rate of change of momentum of a system is equal to the sum of forces applied to the system.

$$\frac{dM_{\text{sys}}}{dt} = \Sigma F \tag{A.13}$$

Following Chaudhry, we use Reynold's transport theorem[4] in combination with equation A.13, apply Leipnitz's rule and the mean value theorem to obtain the following equation for the control volume [6]:

$$\frac{d}{dt}(\rho A\overline{v}) + \frac{(\rho A\overline{v}^2)_2 - (\rho A\overline{v}^2)_1}{z_2 - z_1} = \frac{\Sigma F}{z_2 - z_1}. \tag{A.14}$$

The sum of forces acting on the control volume are as follows

$$\Sigma F = F_{p_1} - F_{p_2} + F_{wz} - F_s \tag{A.15}$$

$$\Sigma F = p_1 A_1 - p_2 A_2 + \rho g A(z_2 - z_1)\sin\theta - \tau_w \pi D(z_2 - z_1) \tag{A.16}$$

in which F_{p_1}, F_{p_2}, F_{wz} and F_s are the forces to to pressure, fluid weight and shear respectively. θ and τ_w are the inclination angle and shear stress, D is the conduit diameter. We now divide by $\Delta z = z_2 - z_1$

$$\frac{\Sigma F}{\Delta z} = \frac{(p_1 A_1 - p_2 A_2)}{\Delta z} + \rho g A \sin\theta - \tau_w \pi D \tag{A.17}$$

plugging this into equation A.14 and letting Δz approach zero

$$\frac{\partial}{\partial t}(\rho A\overline{v}) + \frac{\partial}{\partial z}(\rho A\overline{v}^2) + A\frac{\partial p}{\partial z} - \rho g A\sin\theta + \tau_w \pi D = 0. \tag{A.18}$$

Now the terms in the bracket are expanded and rearranged

$$\overline{v}\left[\frac{\partial}{\partial t}(\rho A) + \frac{\partial}{\partial z}(\rho A\overline{v})\right] + \rho A\frac{\partial \overline{v}}{\partial t} + \rho A\overline{v}\frac{\partial \overline{v}}{\partial z} + A\frac{\partial p}{\partial z} - \rho g A\sin\theta + \tau_w \pi D = 0 \tag{A.19}$$

refering to the continuity equation (see Equation A.5) the term between brackets is zero. Diving by ρA yield the conservation of momentum equation in its final form:

$$\frac{\partial \overline{v}}{\partial t} + \overline{v}\frac{\partial \overline{v}}{\partial z} + \frac{1}{\rho}\frac{\partial p}{\partial z} - g\sin\theta + \frac{\tau_w \pi D}{\rho A} = 0 \tag{A.20}$$

[4]Reynold's transport theorem states that: $\frac{dB_{\text{sys}}}{dt} = \frac{d}{dt}\int_{cv}\beta\rho dA + \left[\beta\rho A(V-W)\right]_{OUT} - \left[\beta\rho A(V-W)\right]_{IN}$; in this case $\beta = V$ and $B = M_{\text{sys}}$

One last alteration is made by expressing the shear stress on the wall τ_w in terms of a friction factor. It is assumed the energy losses for a given velocity in a transient state are the same as steady state losses at the same velocity. The shear stress may now be expressed in terms of the Darcy-Weisbach friction factor for steady flow

$$\tau_w = f\frac{\rho}{8}\overline{v}|\overline{v}| \tag{A.21}$$

here f is the Darcy-Weisbach friction factor. Plugging this expression into the momentum equation results in:

$$\frac{\partial \overline{v}}{\partial t} + \overline{v}\frac{\partial \overline{v}}{\partial z} + \frac{1}{\rho}\frac{\partial p}{\partial z} - g\sin\theta + \frac{f}{2D}\overline{v}|\overline{v}| = 0 \tag{A.22}$$

A.3. Classification of equations

The continuity and momentum equation form a set of first order partial differential equations PDE's. The equations must be classified before a solution method can be selected. The first step is to write the equations in matrix form:

$$\frac{\partial}{\partial t}\begin{pmatrix} p \\ \overline{v} \end{pmatrix} + \begin{bmatrix} \overline{v} & \rho c^2 \\ \frac{1}{\rho} & \overline{v} \end{bmatrix}\frac{\partial}{\partial z}\begin{pmatrix} p \\ \overline{v} \end{pmatrix} = \begin{pmatrix} 0 \\ +g\sin\theta - \frac{f\overline{v}|\overline{v}|}{D} \end{pmatrix} \tag{A.23}$$

or

$$\frac{\partial \mathbf{U}}{\partial t} + \mathbf{B}\frac{\partial \mathbf{U}}{\partial z} = \mathbf{E} \tag{A.24}$$

in which:

$$\mathbf{U} = \begin{pmatrix} p \\ \overline{v} \end{pmatrix}; \mathbf{B} = \begin{bmatrix} \overline{v} & \rho c^2 \\ \frac{1}{\rho} & \overline{v} \end{bmatrix}; \mathbf{E} = \begin{pmatrix} 0 \\ +g\sin\theta - \frac{f\overline{v}|\overline{v}|}{D} \end{pmatrix} \tag{A.25}$$

The eigenvalues of **B** determine the class of the equations. The characteristic equation is [6]:

$$(\overline{v} - \lambda')^2 = c^2 \tag{A.26}$$

and so

$$\lambda' = \overline{v} \pm c \tag{A.27}$$

The eigenvalues are real and distinct. Therefore the continuity and momentum equation form a set of hyperbolic PDE's. This type of equations describe the propagation of two component waves, the following solution methods may be applied:

- Method of characteristics
- Finite-difference methods
- Finite-element methods
- Spectral methods
- Boundary-integral methods

The method of characteristics is popular and often used in solving one dimensional fluid transients. It is easy to program, efficient in computational time, and allows for the inclusion of complex boundary conditions. This method also correctly captures the propagation of steep wave fronts. Finite difference models have a similar performance to the method of characteristics. Yet they are used less often as implementing boundary conditions in more tedious. Using a finite element method offers no advantages compared to the other available methods. Spectral methods are not suitable for boundaries which are not fully absorbing and the boundary-integral methods handle time dependent problems ineffeciently [6].

With these considerations, the method of characteristics is used.

B

Method of Characteristics

B.1. Characteristics equations

In order to derive the characteristic equations, we start with the conservation of momentum and continuity equations. The derivation is presented [6]. The conservation of momentum equation is as follows:

$$L_1 = \frac{\partial \overline{v}}{\partial t} + \overline{v}\frac{\partial \overline{v}}{\partial z} + \frac{1}{\rho}\frac{\partial p}{\partial z} - g\sin\theta + \frac{f}{2D}\overline{v}|\overline{v}| = 0 \tag{B.1}$$

And the continuity equation is:

$$L_2 = \frac{\partial p}{\partial t} + \overline{v}\frac{\partial p}{\partial z} + \rho c^2\frac{\partial \overline{v}}{\partial z} = 0 \tag{B.2}$$

We seek a linear combination of the two L. The two equations are added after equation B.2 is multiplied with an unknown multiplier λ

$$L = L_1 + \lambda L_2 \tag{B.3}$$

rewriting this equations

$$L = \left(\frac{\partial \overline{v}}{\partial t} + (\overline{v} + \lambda\rho c^2)\frac{\partial \overline{v}}{\partial z}\right) + \lambda\left(\frac{\partial p}{\partial t} + \left(\overline{v} + \frac{1}{\rho\lambda}\right)\frac{\partial p}{\partial z}\right) - g\sin\theta + \frac{f}{2D}\overline{v}|\overline{v}| = 0 \tag{B.4}$$

Now, knowing that $\frac{df}{dt} = \frac{\partial f}{\partial t} + \frac{dz}{dt}\frac{\partial f}{\partial z}$ we can state that

$$L = \frac{d\overline{v}}{dt} + \lambda\frac{dp}{dt} - g\sin\theta + \frac{f}{2D}\overline{v}|\overline{v}| = 0 \tag{B.5}$$

This is true only if:

$$\frac{dz}{dt} = \overline{v} + \lambda\rho c^2 = \overline{v} + \frac{1}{\rho\lambda} \tag{B.6}$$

therefore

$$\lambda = \pm\frac{1}{\rho c}. \tag{B.7}$$

We can now write out the characteristic equations in their final form:

$$\frac{d\overline{v}}{dt} \pm \frac{1}{\rho c}\frac{dp}{dt} - g\sin\theta + \frac{f}{2D}\overline{v}|\overline{v}| = 0 \tag{B.8}$$

The two coupled partial differential equations have been rewritten into a set of two uncoupled ordinary differential equations which are dependent only on time. However, this holds true only along the gradients

$$\frac{dz}{dt} = \overline{v} \pm c \tag{B.9}$$

These gradients are called the characteristic lines. Mathematically they divide in the z,t plane into two different regions for which different solutions hold. Physically they represent the paths along which information,

such as a disturbance, travels.

Another simplification is made. Recognizing that $\overline{v} << c$ it is acceptable to state that $\frac{dz}{dt} \approx \pm c$. This simplification is useful as the solution only depends on the wave speed c. Since c, unlike $\overline{v}$, does not vary in time, the characteristic lines are now straight lines in the z,t plane. This assumption is the same as assuming that the non-linear convective acceleration terms in the continuity equation ($\overline{v}\frac{\partial p}{\partial z}$) and momentum equations ($\overline{v}\frac{\partial \overline{v}}{\partial z}$) may be neglected as is often the case for engineering applications [6].

B.2. Characteristic lines

Before their numerical application is explained, the physical and mathematical significance of the characteristic lines should be mentioned. The characteristic lines are either a positive characteristic, C^+, valid along $\frac{dz}{dt} = +c$ or a negative characteristic, C^-, valid along $\frac{dz}{dt} = -c$. The z,t plane is filled with an infinite number of characteristic lines. However, discretization results in a finite number of lines. Information concerning the fluids pressure and velocity travels along these lines. A graphical representation of one positive and one negative characteristic is given below.

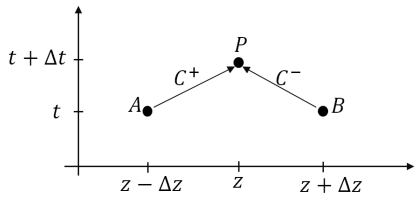

Figure B.1: Graphical representation of the characteristic lines

At point P, the two characteristic lines meet. Here two unknowns (pressure and velocity) may be solved by using the two characteristic equations. This means that the state of the fluid at a node is determined based on the fluid's state at the two surrounding nodes at the previous time step. The characteristics only meet at predefined points (nodes) in time and space.

B.3. Numerical integration

For the characteristic equations to be useful they must be solved for pressure and velocity. This is done by means of numerical integration along the gradients for which the equations are valid. This process will be performed on the positive C^+ characteristic. First, equation B.8 is multiplied by dt after which it is integrated.

$$\int_{t_A,z_A}^{t_P,z_P} d\overline{v} + \frac{1}{\rho c}\int_{t_A,z_A}^{t_P,z_P} dp - g\sin\theta \int_{t_A,z_A}^{t_P,z_P} dt + \frac{1}{2D}\int_{t_A,z_A}^{t_P,z_P} f\overline{v}|\overline{v}|dt = 0 \tag{B.10}$$

This integration is easily performed except for the friction term which depends on square of the mean fluid velocity. A first order approximation of the friction term is sufficient for most engineering practices [6] . This approximation is as follows:

$$\frac{1}{2D}\int_{t_A,z_A}^{t_P,z_P} f\overline{v}|\overline{v}|dt \approx \frac{1}{2D} f_A\overline{v}_A|\overline{v}_A|(t_P - t_A) = \frac{1}{2D} f_A\overline{v}_A|\overline{v}_A|\Delta t. \tag{B.11}$$

The step from steady to quasi-steady friction is made here too. The friction factor is determined based on the state of the fluid meaning that it is not constant. Performing the integration over the positive characteristic yields

$$\overline{v}_P - \overline{v}_A + \frac{1}{\rho c}(p_P - p_A) - g\sin\theta\Delta t + \frac{1}{2D} f_A\overline{v}_A|\overline{v}_A|\Delta t = 0 \tag{B.12}$$

performing the same procedure on for the negative characteristic leads to

$$\overline{v}_P - \overline{v}_B - \frac{1}{\rho c}(p_P - p_B) - g\sin\theta\Delta t + \frac{1}{2D} f_B\overline{v}_B|\overline{v}_B|\Delta t = 0 \tag{B.13}$$

At this point the expressions for the positive and negative characteristics are exact, except from the friction term. For both equations the only unknowns are $\overline{v}_P$ and p_P. Using both equations B.12 and B.13 it is possible to find an expression for these unknowns.

$$p_P = \frac{1}{2}\left(p_A + p_B + \rho c\left(\overline{v}_A - \overline{v}_B - \frac{\Delta t}{2D}\left(f_A \overline{v}_A|\overline{v}_A| - f_B \overline{v}_B|\overline{v}_B|\right)\right)\right) \tag{B.14}$$

$$\overline{v}_P = \frac{1}{2}\left(\overline{v}_A + \overline{v}_B + \frac{p_A - p_B}{\rho c} + 2g\sin\theta\Delta t - \frac{\Delta t}{2D}\left(f_A \overline{v}_A|\overline{v}_A| + f_B \overline{v}_B|\overline{v}_B|\right)\right) \tag{B.15}$$

B.4. Implementation

B.4.1. Interior nodes

As depicted in figure B.1, equations B.14 and B.15 can be used to solve for the pressure and velocity for all interior nodes based on the pressures and velocities in the system at the previous time step. Equations B.14 and B.15 are rewritten into matrix notation. These matrices are easily solved for each time step as MATLAB is a vector based programming language [32].

$$\begin{bmatrix} p_2^{t+\Delta t} \\ \vdots \\ p_{N-1}^{t+\Delta t} \end{bmatrix} = \frac{1}{2}\begin{bmatrix} 1 & 0 & 1 & & \\ & \ddots & & & \\ & & 1 & 0 & 1 \end{bmatrix}\begin{bmatrix} p_1^t \\ \vdots \\ p_N^t \end{bmatrix} + \frac{1}{2}\rho c\begin{bmatrix} 1 & 0 & -1 & & \\ & \ddots & & & \\ & & 1 & 0 & -1 \end{bmatrix}\begin{bmatrix} \overline{v}_1^t \\ \vdots \\ \overline{v}_N^t \end{bmatrix} - \frac{\rho c \Delta t}{4D}\begin{bmatrix} f_A & 0 & -f_B & & \\ & \ddots & & & \\ & & f_A & 0 & -f_B \end{bmatrix}\begin{bmatrix} \overline{v}_1^t \\ \vdots \\ \overline{v}_N^t \end{bmatrix}\begin{bmatrix} |\overline{v}_1^t| \\ \vdots \\ |\overline{v}_N^t| \end{bmatrix} \tag{B.16}$$

And similarly for the velocities we may write

$$\begin{bmatrix} \overline{v}_2^{t+\Delta t} \\ \vdots \\ \overline{v}_{N-1}^{t+\Delta t} \end{bmatrix} = \frac{1}{2}\begin{bmatrix} 1 & 0 & 1 & & \\ & \ddots & & & \\ & & 1 & 0 & 1 \end{bmatrix}\begin{bmatrix} \overline{v}_1^t \\ \vdots \\ \overline{v}_N^t \end{bmatrix} + \frac{1}{2\rho c}\begin{bmatrix} 1 & 0 & -1 & & \\ & \ddots & & & \\ & & 1 & 0 & -1 \end{bmatrix}\begin{bmatrix} p_1^t \\ \vdots \\ p_N^t \end{bmatrix} + \begin{bmatrix} g\sin\theta\Delta t \\ \vdots \\ g\sin\theta\Delta t \end{bmatrix} - \frac{\Delta t}{4D}\begin{bmatrix} f_A & 0 & f_B & & \\ & \ddots & & & \\ & & f_A & 0 & f_B \end{bmatrix}\begin{bmatrix} \overline{v}_1^t \\ \vdots \\ \overline{v}_N^t \end{bmatrix}\begin{bmatrix} |\overline{v}_1^t| \\ \vdots \\ |\overline{v}_N^t| \end{bmatrix} \tag{B.17}$$

B.4.2. Boundary Conditions

Reservoir

A constant pressure, or reservoir, boundary condition is used at the surface where the pressure is always atmospheric pressure ($P_{atm} = 0$). The velocity at this boundary may be solved by plugging the desired value of the pressure into either equation B.12 or B.13, depending on which end of the grid the boundary is located. At this boundary velocity waves are fully reflected.

Reflective

At the bottom hole the boundary is either fully or partially reflective. If the boundary is fully reflective, the velocity at the boundary is zero. i.e. the system is closed and any incoming pressure wave is reflected. Here $v = 0$ is plugged into to either equation B.12 or B.13 depending on which end of the grid the boundary is located. The pressure can be solved directly as it is the only unknown in the equation.

B.4.3. Numerical stability

Stability of the MoC scheme must be guaranteed in order to obtain trustworthy solutions. Methods to determine stability criteria for non-linear partial differential equations do not exist. However, these may be determined for linear equations and then applied to non-linear equations as long as the non-linearity are small. By neglecting the non-linear convective acceleration ($v << c$) and the friction term, it can be shown that a MoC scheme is stable if the the Courant-Friedrich-Lewy (CFL) stability condition (equation B.18) or Courant condition (equation B.19) is satisfied [6].

$$\Delta z \geq c\Delta t \tag{B.18}$$

$$C_N = \frac{c}{\Delta z/\Delta t} = \frac{c\Delta t}{\Delta z} \leq 1 \tag{B.19}$$

Here C_N is the Courant number, the ratio between the physical and numerical wave speed. It is convenient to set C_N equal to 1 since this will result in a numerical scheme in which no interpolation is needed as $c = \frac{\Delta z}{\Delta t}$. This should also increase accuracy of the solution as interpolation may lead to numeric dispersion. However, this stability criterion is formulated without the friction term. Large friction factors might therefore cause the finite difference scheme to become unstable even if the CFL criterion in satisfied.

B.5. Validation

Early in the project the numeric scheme used in the project was verified. A reference water hammer problem from literature is used to confirm the author's results [29, 32].This paper contains a suitable problem, with an accurate description of the input parameters and the results. The considered system is depicted in figure B.2. It is a friction less sudden valve closure problem, with a reservoir (constant pressure) boundary condition at end and a valve which closes instantaneously at t=0 at the other end.

Figure B.2: Numerical validation problem

The sudden closure of the valve sets and keeps the velocity at the valve equal to zero. This causes the kinetic energy of the fluid to be converted into potential energy: pressure with a magnitude of $\rho c v_0$. This is reversed at the pressure boundary. The resulting two component wave (pressure and velocity) oscillates between the boundaries.

Table B.1: Input variables for the numerical validation

Variable	Value
Boundary pressure (P_{res})	0 [Pa]
Length (L)	20 [m]
Density (ρ)	1000 [kg/m3]
Initial velocity (v_0)	1.002 [m/s]
Wave speed (c)	1025.7 [m/s]

The comparative results are displayed in Figure B.3. The calculated pressure magnitude matches the value obtained by [29] of 1.028 MPa. The shape and propagation speed of the pressure wave match. This validates the numerical scheme used by the author.

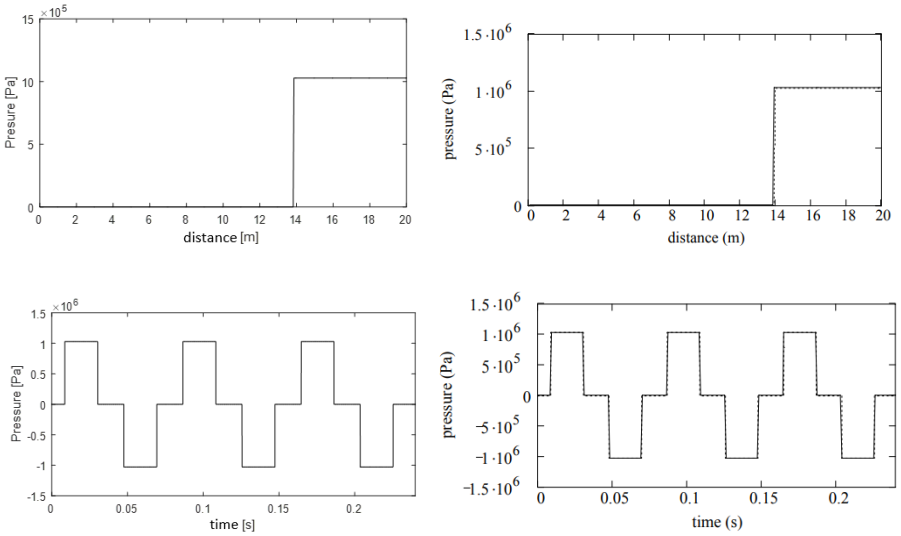

Figure B.3: Comparison of the results for the validation problem by the author (left) and by [29] (right)

B.6. Interpolation

As mentioned, the stability criteria are derived without the non-linear friction term. If this term becomes too large, the MoC scheme may become unstable even if the CFL criterion is satisfied. This is because a Courant number equal to unity means the system is on the edge of its stability limit. Unstable solutions were encountered during the analysis of the experimental data. The narrow clearance resulted in large friction term. To overcome this obstacle the MoC scheme is adapted so that it's Courant number is equal to 0.99. This requires interpolation. Having C_N close to unity minimizes the numeric dispersion and damping. The interpolation is linear and according to the method of specified intervals.

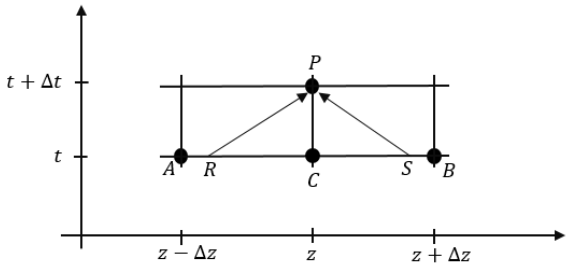

Figure B.4: Method of specified intervals

Linear interpolation is done by performing the following substitutions [6]

$$\overline{v}_A \Rightarrow \overline{v}_R = \overline{v}_C - \frac{c\Delta t}{\Delta z}(\overline{v}_C - \overline{v}_A), \tag{B.20}$$

$$\overline{v}_B \Rightarrow \overline{v}_S = \overline{v}_C - \frac{c\Delta t}{\Delta z}(\overline{v}_C - \overline{v}_B), \tag{B.21}$$

$$p_A \Rightarrow p_R = p_C - \frac{c\Delta t}{\Delta z}(p_C - p_A), \tag{B.22}$$

$$p_B \Rightarrow p_S = p_C - \frac{c\Delta t}{\Delta z}(p_C - p_B). \tag{B.23}$$

Naturally this changes the matrix form of the solution. An interpolated scheme is no longer equal to Equations B.16 and B.17. Interpolations cause dispersion and damping. The effect on the validation problem is shown below. The dispersion is clearly visible, and although not visible, damping occurs.

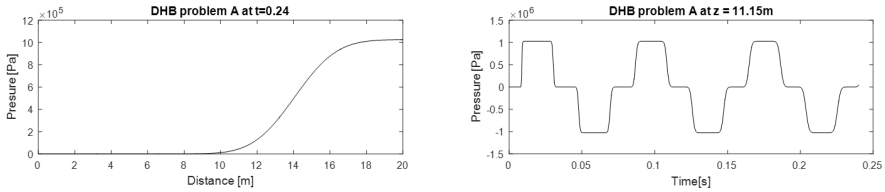

Figure B.5: Dispersion and some damping due to interpolations, $C_N = 0.8$

C

Wave celerity

The undamped wave propagation speed, c, contains a term which relates changes in conduit cross sectional area to fluid pressure. The wave speed is defined as:

$$c = \sqrt{\frac{1}{\rho\left(\frac{1}{K} + \frac{1}{A}\frac{\partial A}{\partial p}\right)}} \tag{C.1}$$

in which K is the fluid compressibility, which is assumed to be equal to the compressibility of water. The expression for $\frac{\partial A}{\partial p}$ is derived in this appendix.

The propagation speed is calculated for:

1. The drillstring
2. The annulus between casing and drillstring
3. The annulus between casing and assembly

C.1. Thick walled cylinder elasticity

Elastic theory as presented by [31] is used to determine the change $\mathrm{d}A/\mathrm{d}p$ for various sections of the well. Expansion or contraction of the conduits is governed by the fluid pressure acting on the conduit wall. If the pressure dependent radial displacement can be determined the change in area resulting from pressure changes can be determined. Lame's equations are the start of this analysis. For thick-walled cylinders the radial stress is defined as:

$$\sigma_r = \frac{p_i a^2 - p_o b^2 + \frac{a^2 b^2}{r^2}(p_o - p_i)}{b^2 - a^2} \tag{C.2}$$

in which a and b are the inner and outer radius and p_i and p_o are the inner and outer pressure. The Hoop stress is defined as:

$$\sigma_\theta = \frac{p_i a^2 - p_o b^2 - \frac{a^2 b^2}{r^2}(p_o - p_i)}{b^2 - a^2} \tag{C.3}$$

The engineering tangential strain is defined by:

$$\epsilon_\theta = \frac{u}{r} \tag{C.4}$$

$$\epsilon_\theta = \frac{1}{E}(\sigma_\theta - \mu\sigma_r) \tag{C.5}$$

where u is the radial displacement, r the radius, E the Young's modulus and μ is Poisson's ratio. Combining these two expressions leads to:

$$u = \frac{r}{E}(\sigma_\theta - \mu\sigma_r) \tag{C.6}$$

Now, using Lame's equation for the radial and hoop strain and solving for the radial displacement leads to:

$$u = \frac{r}{E(b^2 - a^2)}(p_i[(1-\mu])a^2 + (1+\mu)b^2] - 2p_o b^2) \tag{C.7}$$

thus the new cross sectional area equals

$$A_{new} = \pi(r+u)^2 = \pi(r^2 + 2ru + u^2) \tag{C.8}$$

the expression may be linearized since $u << r$

$$A_{new} \approx \pi(r^2 + 2ru). \tag{C.9}$$

Taking the derivative of A to either p_o or p_i leads to the desired $\mathrm{d}A/\mathrm{d}p$ term. Maple, mathematical software, is used to perform this operation.

C.2. The drillstring

While determining the elasticity term for the drillstring consider the cross-section A-A as presented in figure C.1.

$$u_1 = \frac{r_1}{E_s(r_2^2 - r_1^2}(p_{ds}[(1-\mu_s])r_1^2 + (1+\mu_s)r_2^2] - 2p_{an}r_2^2) \tag{C.10}$$

$$A_{ds,new} = \pi\left(r_1^2 + \frac{2r_1^2}{E_s(r_2^2 - r_1^2}(p_{ds}[(1-\mu_s])r_1^2 + (1+\mu_s)r_2^2] - 2p_{an}r_2^2)\right) \tag{C.11}$$

The derivative of equation C.11 is taken to p_{ds} and p_{an} to determine the dependency of the drillstring flow area on the external and internal pressure.

$$\frac{\partial A_{ds}}{\partial p_{ds}} = \frac{2\pi r_1^2}{E_s}\left(\frac{r_2^2 + r_1^2}{r_2^2 - r_1^2} + \mu_s\right) \tag{C.12}$$

$$\frac{\partial A_{ds}}{\partial p_{an}} = -\frac{4\pi r_1^2}{E_s}\left(\frac{r_2^2}{r_2^2 - r_1^2}\right) \tag{C.13}$$

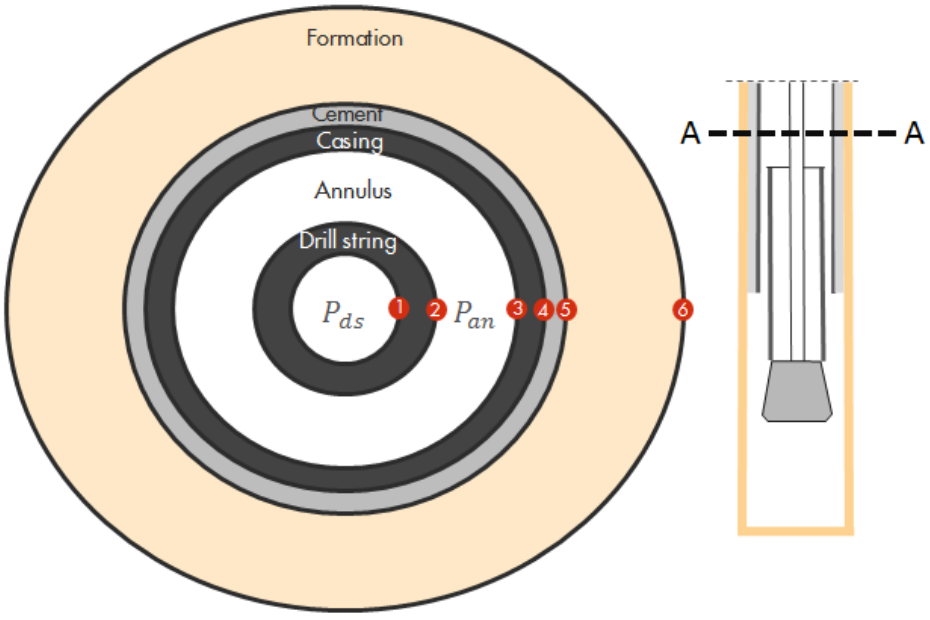

Figure C.1: Cross section (A-A)of composite cylinders making up the cased annulus

C.3. The annulus between casing and drillstring

The procedure for determining the elasticity of the annulus is more complex. The formation, cement, and casing form a composite cylinder, see figure C.1. The expansion of the annulus depends on the interaction between these layers. The composite wellbore is treated as steel and concrete annuli for which interface pressure dependent radial displacement relationships are formulated. This system of equations is then solved to obtain the composite elasticity. This procedure is described in [14] including thermal expansion, in this thesis thermal expansion is not included.

The radial displacement of the outside of the drillstring:

$$u_2 = \frac{r_2}{E_s(r_2^2 - r_1^2)}(2p_{ds}r_1^2 - p_{an}[(1-\mu_s)r_2^2 + (1+\mu_s)r_1^2]). \tag{C.14}$$

The radial displacement of the inside of the casing:

$$u_3 = \frac{r_3}{E_s(r_4^2 - r_3^2)}(p_{an}[(1-\mu_s)r_3^2 + (1+\mu_s)r_4^2] - 2p_4r_4^2) \tag{C.15}$$

$$u_3 = C_1p_{an} + C_2p_4 \tag{C.16}$$

in which p_4 is the interface pressure at r_4. The radial displacement of the outside of the casing is:

$$u_{4i} = \frac{r_4}{E_s(r_4^2 - r_3^2)}(2p_{an}r_3^2 - p_4[(1-\mu_s)r_4^2 + (1+\mu_s)r_3^2]) \tag{C.17}$$

$$u_{4i} = C_3p_{an} + C_4p_4. \tag{C.18}$$

The radial displacement of the inside of the cement layer is:

$$u_{4o} = \frac{r_4}{E_c(r_5^2 - r_4^2)}(p_4[(1-\mu_c)r_4^2 + (1+\mu_c)r_5^2] - 2p_5r_5^2) \tag{C.19}$$

$$u_{4o} = C_5p_4 + C_6p_5 \tag{C.20}$$

in which p_5 is the interface pressure at r_5. The radial displacement of the outside of the cement layer:

$$u_{5i} = \frac{r_5}{E_c(r_5^2 - r_4^2)}(2p_4r_4^2 - p_5[(1-\mu_c)r_5^2 + (1+\mu_c)r_4^2]) \tag{C.21}$$

$$u_{5i} = C_7p_4 + C_8p_5. \tag{C.22}$$

The radial displacement of the inside of the formation:

$$u_{5o} = \frac{r_5}{E_f(r_6^2 - r_5^2)}(p_5[(1-\mu_f)r_5^2 + (1+\mu_f)r_6^2] - 2p_6r_6^2). \tag{C.23}$$

The formation extends far enough for its outer limits not to be effected by wellbore pressures. The pressure at the outer edge of the formation is zero and r_6 approaches infinity. Taking this limit leads to:

$$u_{5o} = \frac{r_5}{E_f}(1+\mu_f)p_5 \tag{C.24}$$

$$u_{5o} = C_9p_5. \tag{C.25}$$

The radial displacement on both sides of the interfaces must be equal.

$$u_{4i} = u_{4o} = C_3p_{an} + C_4p_4 = C_5p_4 + C_6p_5 \tag{C.26}$$

$$u_{5i} = u_{5o} = C_7p_4 + C_8p_5 = C_9p_5 \tag{C.27}$$

which leads to

$$p_4 = \frac{C_3}{C_5 - C_4 - \frac{C_6C_7}{C_8 - C_9}} \tag{C.28}$$

this expression is plugged into equation C.16.

$$u_3 = \left(C_1 + C_2 \frac{C_3}{C_5 - C_4 - \frac{C_6 C_7}{C_8 - C_9}} \right) \tag{C.29}$$

the new annular area, assuming $u << r$, is

$$A_{an} = \pi (r_3^2 + 2u_3 r_3 - r_2^2 - 2u_2 r_2) \tag{C.30}$$

$$A_{an} = \pi \left(r_3^2 + 2r_3 \left(C_1 + C_2 \frac{C_3}{C_5 - C_4 - \frac{C_6 C_7}{C_8 - C_9}} \right) - r_2^2 - \frac{2r_2^2}{E_s(r_2^2 - r_1^2)} (2p_{ds} r_1^2 - p_{an}[(1-\mu_s) r_2^2 + (1+\mu_s) r_1^2]) \right). \tag{C.31}$$

Taking the derivative of equation C.31 to the annular and drill pipe pressures yields the required elasticity terms.

$$\frac{\partial A_{an}}{\partial p_{an}} = \pi \left(2r_3 \left(C_1 + C_2 \frac{C_3}{C_5 - C_4 - \frac{C_6 C_7}{C_8 - C_9}} \right) - \frac{2r_2^2}{E_s(r_2^2 - r_1^2)} \left((1-\mu_s) r_2^2 + (1+\mu_s) r_1^2 \right) \right) \tag{C.32}$$

$$\frac{\partial A_{an}}{\partial p_{ds}} = -\frac{4\pi r_2^2 r_1^2}{E_s(r_2^2 - r_1^2)} \tag{C.33}$$

C.4. Pressure coupling

During the derivation of the fluid's governing equations, it is assumed that the annulus and drill pipe pressures are uncoupled. This should be verified. A large pressure difference is applied across the drill string. The result area changes are very small. The corresponding change in pressure is also very small. Pressure coupling can therefore be ignored.

C.5. The annulus between casing and assembly

The flow along the liner which is to be expanded and mounted on the BHA is also solved with the MoC, therefore the speed of sound in this section must be known. dA/dp is found with the same procedure as used for the annulus. The composite wellbore is now as presented in figure C.2.

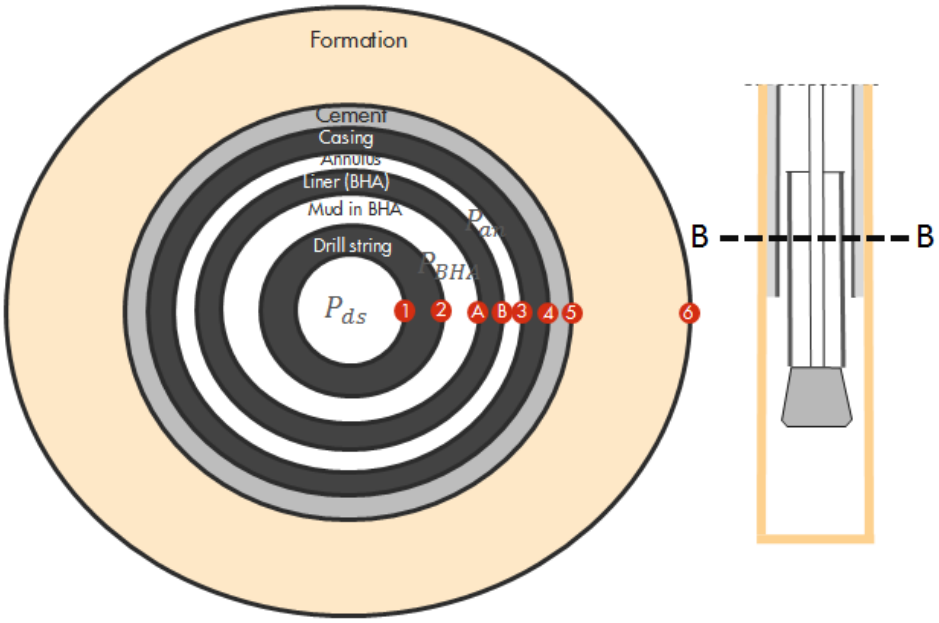

Figure C.2: Cross-section (B-B)of the composite cylinders making up the cased annulus and the BHA

D

Fluid mechanics

Throughout this thesis fluid mechanics, velocity profiles, and CFD calculations have been used to understand flows. The velocity profiles are especially useful while analyzing the clinging constant. CFD is used to study turbulent flows and the flow in and around complex geometries. The following subjects are covered in this appendix:

1. Derivation of the unsteady Bernoulli equation.
2. The derivation of the clinging constant for an incompressible Newtonian fluid in fully developed steady laminar slit flow.
3. The derivation of the clinging constant for an incompressible Newtonian fluid in fully developed steady laminar annular flow.
4. A review of the CFD calculations performed to find the clinging constant for an incompressible Newtonian fluid in fully developed steady turbulent annular flow.
5. The analytical solution to the velocity profile and pressure drop of a PL fluid in fully developed steady laminar slit flow.
6. A review of the CFD calculation concerning the effect of eccentricity on the pressure drop.

D.1. The unsteady Bernoulli equation

The Bernoulli equation is the result of a classical momentum analysis. First described in words by Bernoulli and later derived by Euler, it forms an approximate relation between pressure, velocity and elevation. Bernoulli's equation considers frictionless flow along a stream line as pictured in Figure D.1 [37].

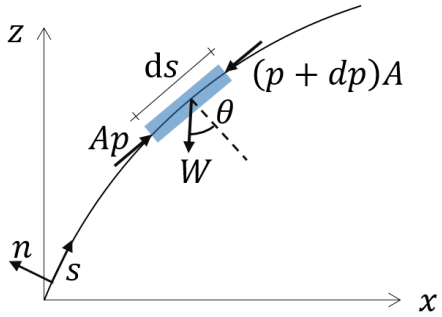

Figure D.1: Forces acting on a differential volume for flow along a streamline

Newton's second law, referred to as the law of conservation of linear momentum in fluid mechanics, is applied:

$$\Sigma F_s = m a_s \tag{D.1}$$

in which ΣF_s is the net force on the differential volume, m its mass and a_s the acceleration along the streamline. s is the streamline's path. ΣF_s is due to pressure and gravity and can be expressed as

$$\Sigma F_s = pA - (p+dp)A - W\sin\theta = -dpA - \rho g A ds\frac{dz}{ds} \tag{D.2}$$

where p is the pressure, ρ the density and A the area. Substitution and expansion of the acceleration into partial derivatives leads to

$$-dpA - \rho g A ds\frac{dz}{ds} = \rho A ds\left(\frac{\partial v_s}{\partial t} + v_s\frac{\partial v_s}{\partial s}\right) \tag{D.3}$$

where v_s is the velocity along the streamline. Dividing by A and by ds

$$-\frac{\partial p}{\partial s} - \rho g\frac{dz}{ds} = \rho\frac{\partial v_s}{\partial t} + \rho v_s\frac{\partial v_s}{\partial s}. \tag{D.4}$$

We now integrate along the streamline

$$-\int_1^2 dp - \rho g\int_1^2 dz = \int_1^2 \rho\frac{\partial v_s}{\partial t}ds + \rho\int_1^2 v_s dv_s. \tag{D.5}$$

Noting that $vdv = \frac{1}{2}d(v^2)$, performing the integration and moving all the terms to the left side of the equation results in

$$\int_1^2 \rho\frac{\partial v_s}{\partial t}ds + \frac{\rho}{2}(v_2^2 - v_1^2) + (p_2 - p_1) + \rho g(z_2 - z_1) = 0. \tag{D.6}$$

which is the unsteady Bernoulli equation. It is valid for incompressible frictionless flow along a streamline.

D.2. Clinging constant for laminar Newtonian slit flow

The pressure drop in a pipe is in equilibrium with the shear stress integrated over the cross-sectional area. If the annular flow is simplified to laminar slit flow (flow between two parallel plates) of an incompressible Newtonian fluid, an analytical solution for the velocity profile, and therefore the pressure drop exists.

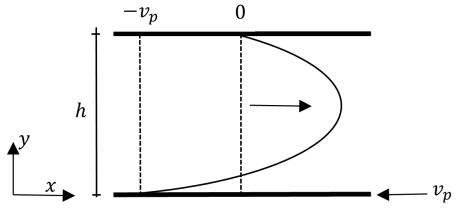

Figure D.2: Laminar slit flow

We begin with the equation of motion of the fluid (Navier-Stokes)

$$\frac{du}{dt} + u\frac{\partial u}{\partial x} + v\frac{\partial u}{\partial y} + w\frac{\partial u}{\partial z} = -\frac{1}{\rho}\frac{\partial p}{\partial x} + \nu\left(\frac{\partial^2 u}{\partial x^2} + \frac{\partial^2 u}{\partial y^2} + \frac{\partial^2 u}{\partial z^2}\right), \tag{D.7}$$

which, for fully developed steady flow in the x-direction in the xy plane reduces to

$$\frac{1}{\rho}\frac{\partial p}{\partial x} = \nu\frac{\partial^2 u}{\partial y^2}. \tag{D.8}$$

in which ν is the kinematic viscosity. Double integration and using the dynamic viscosity μ results in

$$u(y) = \frac{1}{2\mu}\frac{\partial p}{\partial x}y^2 + C_1 y + C_2. \tag{D.9}$$

Applying the boundary conditions, $v(0) = -v_p$ (the wall velocity) and $v(h) = 0$

$$u(y) = \frac{1}{2\mu}\frac{\partial p}{\partial x}(y^2 - hy) + v_p(1 - \frac{y}{h}) \tag{D.10}$$

and integrating over the area yields the discharge

$$Q = \int u dA = \int uW dy = -\frac{Wh^3}{12\mu}\frac{\partial p}{\partial x} + \frac{v_p W h}{2}. \tag{D.11}$$

in which W is the width of the plates. Expressing the pressure drop in terms of the velocity instead of discharge requires the following definitions

$$A = Wh, \quad \overline{v} = \frac{Q}{A} \tag{D.12}$$

in which $\overline{v}$ is the mean fluid velocity, which is known. Solving for the pressure drop per unit length yields

$$\frac{\partial p}{\partial x} = -\frac{12\mu}{h^2}\left(\overline{v} - \frac{v_p}{2}\right) \tag{D.13}$$

where $\overline{v}$ is the bulk velocity. The negative sign indicates that the pressure gradient and flow direction oppose each other if v_p is zero. This equation suggests that the pressure drop for flow of a Newtonian fluid between a stationary and a moving plate depends on the effective mean velocity

$$\overline{v}_{eff} = \left(\overline{v} - \frac{v_p}{2}\right) \tag{D.14}$$

$\overline{v}_{eff}$ is a non-physical equivalent velocity between two stationary plates which results in the same pressure drop as the more complex situation with one moving wall. The clinging constant is defined as the value with which the wall velocity must be multiplied to get the correct effective velocity. Equation D.14 implies that the clinging constant for slit flow is independent of slit height, wall speed or bulk velocity, and has a magnitude of $c_c = 0.5$.

D.3. Clinging constant for laminar Newtonian annular flow

The derivation of an annular clinging constant is a more complex. The geometry is given below.

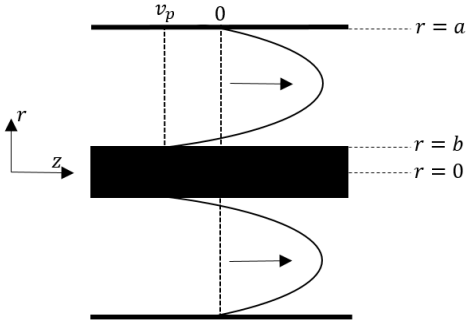

Figure D.3: Flow in an annulus

The same procedure is followed as for slit flow. The difference is that we are now working in cylindrical coordinates

$$\frac{1}{r}\frac{\partial}{\partial r}\left(r\mu\left(\frac{\partial u}{\partial r}\right)\right) = \frac{\partial p}{\partial x} \tag{D.15}$$

which, after double integration, gives

$$u = \frac{1}{4\mu}\frac{\partial p}{\partial x}r^2 + C_1 \ln(r) + C_2. \tag{D.16}$$

The same steps are now performed as in the previous section. However, this time Maple is used to perform the operations. First, the no slip boundary conditions are applied to solve for C_1 and C_2. The expression for u is then integrated to find Q

$$Q = \int_b^a 2\pi u r dr. \tag{D.17}$$

Q is then divided by the cross-sectional area to obtain the mean velocity $\overline{v}$, which is known. The expression is then solved for $\frac{\partial p}{\partial x}$. The equation is rewritten such that $\overline{v}$ and v_p are separated. As can be seen in Equation D.13, the coefficient of v_p is the clinging constant. This means that for an annulus

$$c_c = \frac{-2\ln(a)a^2 - \ln(b)b^2 + a^2 - b^2}{2\ln(a)a^2 - 2\ln(a)b^2 - 2\ln(b)a^2 + 2\ln(b)b^2} = \frac{2\alpha^2\ln(\alpha) - \alpha^2 + 1}{2(\alpha^2 - 1)\ln(\alpha)} \tag{D.18}$$

in which

$$\alpha = \frac{b}{a}. \tag{D.19}$$

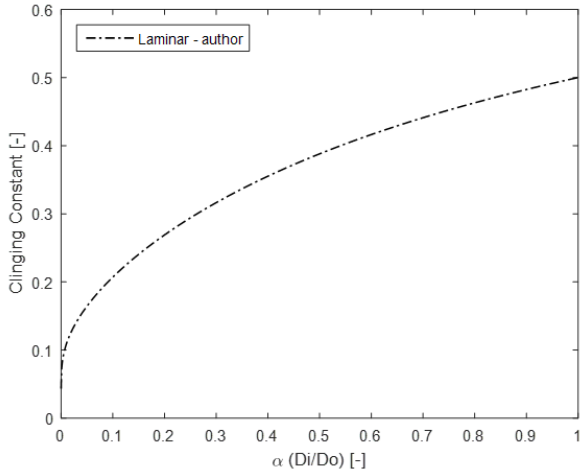

Figure D.4: The laminar annular clinging constant

D.4. Clinging constant for turbulent Newtonian annular flow

D.4.1. Turbulence model

Since no analytical solution is available for turbulent flows in an annulus, CFD calculations are required. FLUENT by ANSYS is used. The $k-\epsilon$ turbulence model with enhanced wall treatment is use.

D.4.2. Set up and verification

The annular geometry is modeled axi-symmetrically so that only one half of the annulus has to be modeled in 2D. The domain has the following components:

1. A stationary outer wall.
2. A moving or stationary inner wall.
3. A pressure inlet.
4. A pressure outlet.
5. A fluid domain which is at least sufficiently long to achieve fully developed flow over the last meter of the pipe (where entrance effects are 0).

The clinging constant is calculated with the following procedure

1. Flow is forced through the domain by a pressure gradient. The mean velocity and pressure drop over the last meter of the pipe are determined with a moving inner wall.
2. The inner wall is fixed. The bulk velocity required to obtain the same pressure drop over the last meter is iteratively found.
3. Knowing the mean velocity for a moving and stationary inner wall allows us to calculate the clinging constant.

Unfortunately there is no analytical solution available to readily verify the turbulent CFD velocity profiles. Yet the axi-symmetric set up of the problem may be verified for a laminar case. As shown in Figure D.5, the solutions match. The velocity profile is non-symmetric because the shear stress is higher at the inner wall.

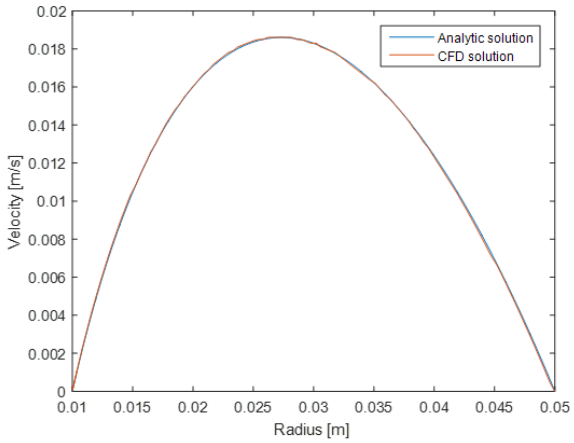

Figure D.5: Verification of the CFD set up, $Re = 100, r_i = 0.01$ m, $r_o = 0.05$ m, $dP/dx = 0.0873$ Pa/m

D.4.3. Calculations

A large set of calculations is performed. The inner radius is varied while the outer radius is kept constant so different values of α are obtained. For the first set of calculations the Reynolds number (Re) is kept at 10.000. During the second set of calculations, Re is set to 50.000. For the 3rd set of calculations the conduit size in increased and Re is arbitrary. This shows the turbulent clinging constant is independent of both Re and the conduit size. Error bars are included; an error of 0.02 is assumed to be fair since the iterative process does not yield the exact value.

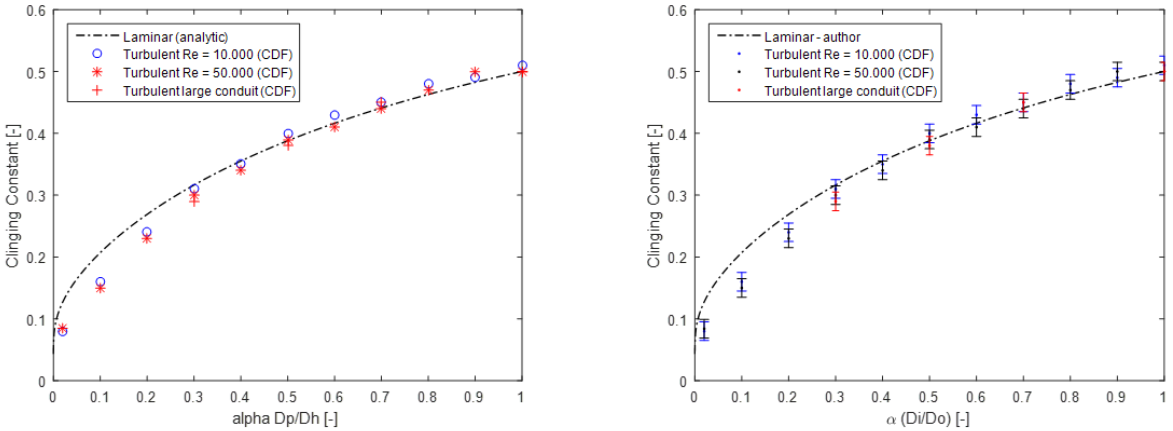

Figure D.6: CFD results for the turbulent clinging constant, obtained values (left) and estimated error range (right)

D.5. Analytical power law fluid velocity profile

D.5.1. Equation of motion

The pressure drop in a pipe is in equilibrium with the shear stress integrated over the cross-sectional area. For laminar flow between two parallel plates of a power law fluid, an analytical solution for the velocity profile, and therefore the pressure drop exists. We aim to find the pressure drop per unit length and the shape of the velocity profile. The inputs are slit height, mean flow velocity and the power law constants. The following derivation is based on [36]. We begin with the equation of motion (Navier-Stokes equation) for a Newtonian fluid in the x direction.

$$\frac{du}{dt} + u\frac{\partial u}{\partial x} + v\frac{\partial u}{\partial y} + w\frac{\partial u}{\partial z} = -\frac{1}{\rho}\frac{\partial p}{\partial x} + \nu\left(\frac{\partial^2 u}{\partial x^2} + \frac{\partial^2 u}{\partial y^2} + \frac{\partial^2 u}{\partial z^2}\right) \tag{D.20}$$

Which, for fully developed laminar slit flow in the xy plane reduces to

$$\frac{1}{\rho}\frac{\partial p}{\partial x} = \nu\frac{\partial^2 u}{\partial y^2} = \frac{1}{\rho}\frac{\partial \tau}{\partial y} \tag{D.21}$$

Rewriting $\frac{\partial p}{\partial x}$ as p and replacing the Newtonian rheology with power law rheology we obtain:

$$p = \frac{\partial}{\partial y}\left(k\left(\frac{du}{dy}\right)^n\right) \tag{D.22}$$

$$k\left(\frac{du}{dy}\right)^n = p(y - y_0) \tag{D.23}$$

y_0 is the point where shear in the fluid is zero, i.e. $\frac{du}{dy} = 0$. Due to the moving wall y_0 could be outside of the slits dimensions. Between the two plates

$$k\left(\frac{du}{dh}\right)^n = p(h - h_0) \tag{D.24}$$

here h is the height of the slit. Let's introduce y as the non dimensional slit height so that $y(w = 0) = 0$ at the lower wall and $y(w = h) = 1$ at the upper wall. w is the distance from the lower wall. $y = \frac{h}{w}$.

D.5.2. Pressure driven flow

If the flow is dominated by a driving pressure instead of the moving wall, the velocity profile be similar to that of Poisueille flow. Here the point y_0 falls within the slit's dimensions.

For $y \leq y_0$

$$\frac{du}{dy} = \left(-\left|\frac{p}{k}\right| w(y - y_0)\right)^{\frac{1}{n}} \tag{D.25}$$

Integration and rewriting $\frac{1}{n}$ as N:

$$u(y) = -\beta(-(y - y_0))^{N+1} + C_1 \tag{D.26}$$

in which

$$\beta = \frac{1}{N+1}\left|\frac{p}{k}\right|^N w^{N+1} \tag{D.27}$$

We can now apply our first boundary condition at the stationary wall

$$u(0) = 0 \Rightarrow C_1 = \beta y_0^{N+1} \tag{D.28}$$

$$u(y) = -\beta((-(y - y_0))^{N+1} - y_0^{N+1}) \tag{D.29}$$

$$u(y_0) = \beta(y_0^{N+1}) \tag{D.30}$$

For $y > y_0$

$$\frac{du}{dy} = -\left(\left|\frac{p}{k}\right| w(y - y_0)\right)^N \tag{D.31}$$

$$u(y) = \int_{y_0}^{y}\frac{du}{dy} + u(y_0) = u(y) = -\beta(((y - y_0))^{N+1} - y_0^{N+1}) \tag{D.32}$$

Applying the second boundary condition:

$$u(1) = v_p = -\beta(((y - y_0))^{N+1} - y_0^{N+1}) \tag{D.33}$$

However, both β and y_0 are still unknown. Integration of the velocity profile yields the mean velocity $\overline{u}$, which we assume to be known. Integration must be performed separately over the two intervals.

$$\overline{u} = \int_0^{y_0} u(y)dy + \int_{y_0}^{1} u(y)dy = -\beta\left(\frac{1}{N+2}\left(y_0^{N+2} + (1 - y_0)^{N+2}\right) - y_0^{N+1}\right) \tag{D.34}$$

Using both the boundary condition and the expression for the bulk velocity we can solve for y_0 and subsequently solve for β.

$$\beta = -\frac{v_p}{(((y-y_0))^{N+1} - y_0^{N+1})} = \frac{\overline{u}}{\frac{1}{N+2}\left(y_0^{N+2} + (1-y_0)^{N+2}\right) - y_0^{N+1}} \tag{D.35}$$

With α known, we can solve for the pressure drop due to the moving inner wall of the annulus during laminar flow

$$p = k\left(\frac{\beta(N+1)}{w^{N+1}}\right)^n \tag{D.36}$$

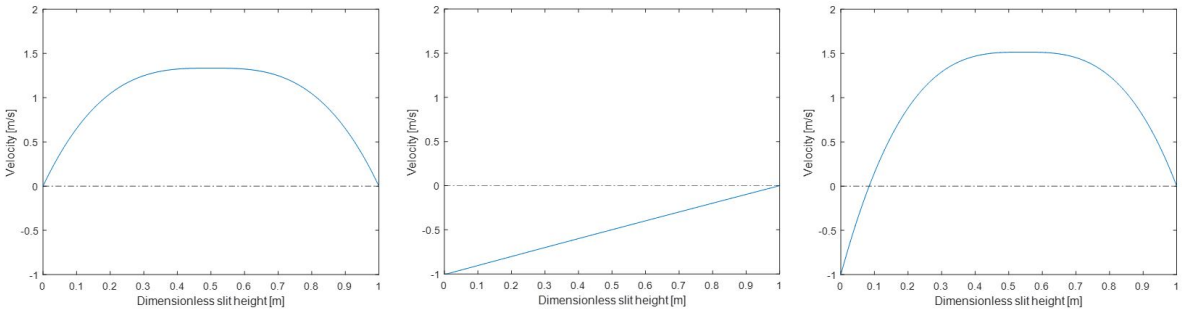

Figure D.7: Velocity profiles for (1) Poisueille flow, (2) Couette flow and (3) combined Couette-Poisueille flow

D.5.3. Shear driven flow

If the flow is driven primarily by the wall movement, the velocity will similar to Couette flow. It is possible that y_0 falls outside of the interval [0 1], requiring a separate solution.

In case $y_0 > 1$

$$\frac{du}{dy} = \left(-\left|\frac{p}{k}\right| w(y-y_0)\right)^{\frac{1}{n}} \tag{D.37}$$

$$\overline{u} = \int_0^1 u(y)dy = -\beta\left[\frac{1}{N+2}((y_0^{N+2} - (-(1-y_0))^{N+2}) - y_0^{N+1}\right] \tag{D.38}$$

in case $y_0 < 0$

$$\frac{du}{dy} = -\left(\left|\frac{p}{k}\right| w(y-y_0)\right)^N \tag{D.39}$$

$$u(y) = -\beta(y-y_0)^{N+1} + C_1 \tag{D.40}$$

Applying the boundary conditions at the walls

$$u(0) = 0 \rightarrow C_1 = \beta(-y_0)^{N+1} \tag{D.41}$$

$$u(y) = -\beta((y-y_0)^{N+1} - (-y_0)^{N+1}) \tag{D.42}$$

$$u(1) = v_p = -\beta((1-y_0)^{N+1} - (-y_0)^{N+1}) \tag{D.43}$$

$$\overline{u} = \int_0^1 u(y)dy = -\beta\left[\frac{1}{N+2}((1-y_0)^{N+2} - (-y_0)^{N+2} - (-y_0)^{N+1}\right] \tag{D.44}$$

y_0 and β may then be solved as was done for Poisueille dominated flow.

D.6. Inner pipe eccentricity

D.6.1. Pressure drop

Eccentricity of the inner pipe is known to reduce the pressure drop per unit length given an average velocity. Regression models from literature for calculating the ratio of eccentric to concentric pressure drop are not valid for the ratio of pipe diameters considered in this thesis. To obtain insight in the order of magnitude of the reduction in resistance, CFD simulations are performed. The goal of these calculations is to find out how large the effect of an eccentric inner pipe would be on the surge/swab pressures observed during the experiment on the Rijswijk test rig. Thus for these calculations the pipe is assumed to be fully eccentric, the pipe walls make contact. The input geometry for the concentric and eccentric scenario are given below.

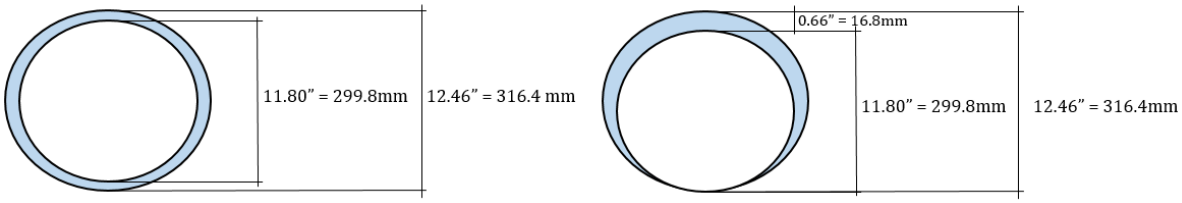

Figure D.8: Geomtery for the CFD calculation, concentric (left) and eccentric cases (right)

The inner pipe is given a velocity of 0.34 m/s. The fluid is given a mean velocity of 3.08 m/s, in the opposite direction. This mean velocity corresponds with the maximum velocity the fluid would reach due to perfect displacement. Calculations are performed for both turbulent and laminar flow. Flow is expected to be laminar. Yet, entrance effects or the movement of the inner pipe could make the flow turbulent. The problem is treated in 3D and the pipe is assumed infinitely long. Turbulent flow is solved with the $k-\epsilon$ model. The results are provided below.

Table D.1: Summary of CFD results: pressure drop per meter and percent difference

Flow regime	Concentic [kPa/m]	Eccentric [kPa/m]	Percent difference [-]
Laminar	18.8	9.00	-52.1
Turbulent	18.8	11.7	-37.8

It is clear that eccentricity has a significant effect on the swab/surge pressure, reducing it by 40-50%. The value of 18.8 kPa/m for the concentric case yields a pressure drop of 80 psi over the length of the assembly. This value is very close to the measured pressure. It has been mentioned that the non-Newtonian behavior of the fluid amplified the effect of eccentricity. Compared to Newtonian flow, the velocities are high is the wide section and much lower in the narrow part (Figure D.9).

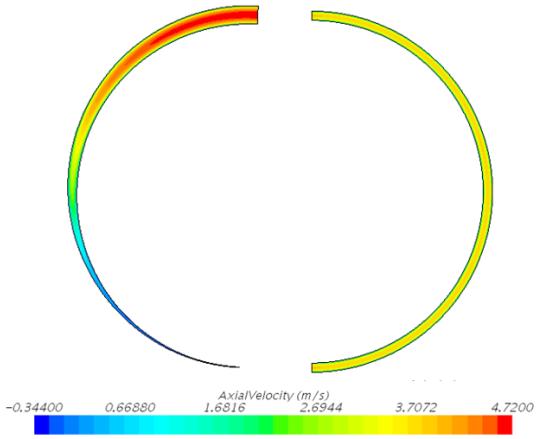

Figure D.9: Velocity contour plot over the cross-section, eccentric (left) and concentric (right)

D.6.2. Centering mechanism

For eccentricity to explain the difference between the measurements and predictions, the pipe must center itself when traveling at high speed and return to an eccentric position once it is slowed down. The author first believed the velocity difference over the cross-section would result in a pressure difference equal to the dynamic pressure. In fluid mechanics the total pressure is defined as

$$p_t = p_s + p_d \tag{D.45}$$

where p_s is the static pressure, the true pressure acting on the surroundings. The dynamic pressure

$$p_d = \rho \frac{v^2}{2g} \tag{D.46}$$

is defined as the pressure required to bring flow to a standstill, this is the increase in pressure seen in front of a body placed in a flow. The author expected to total pressure to be constant over the intersection and the static pressure to vary with the dynamic pressure, which would result in a net centering force on the inner pipe as the high velocity in the wide section would lead to a low pressure. However, the CFD results predict a constant static pressure over the cross-section, Figure D.10.

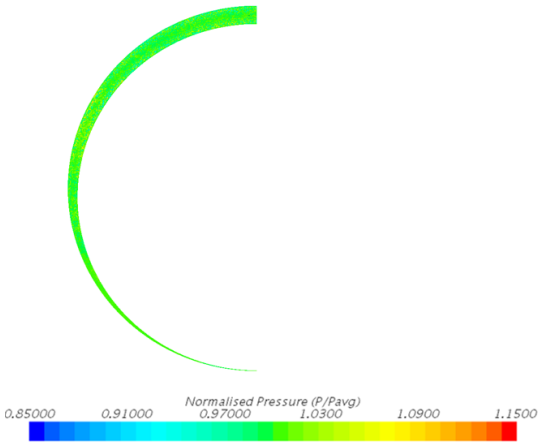

Figure D.10: Normalized static pressure over the cross-section

Thought experiments lead to the conclusion that the CFD results are indeed correct. The pipe acts like a symmetric airfoil with zero angle of attack in ground effect, which does not produce any lift. This hypothesis is confirmed with another CFD simulation. This time, the modeled inner pipe is given a finite length. To simplify calculations the reference frame is changed from a moving inner pipe to a stationary inner pipe, see Figure D.11. Although this slightly changes the velocity field, and thus the pressure field, the results will reveal if their is a significant centering force on the pipe.

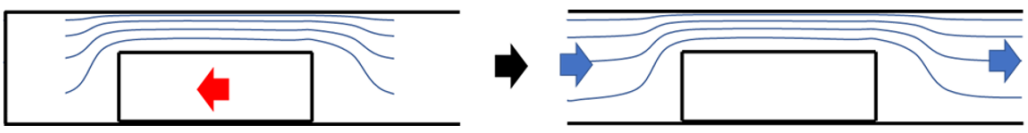

Figure D.11: Changing the reference frame

The resulting pressure distribution is given in Figure D.12.

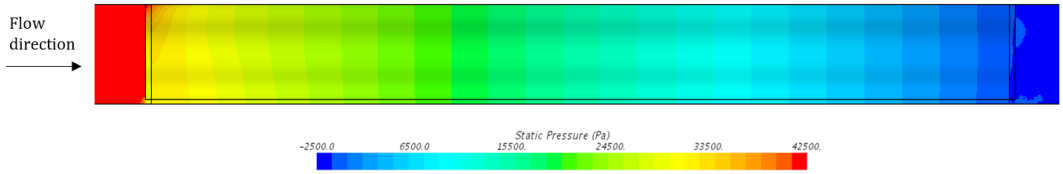

Figure D.12: Pressure distribution along the pipe

After a strong entrance effect, the static pressure indeed becomes constant over the cross section. This means that in the pipe may only be centered by the entrance effect. A centering force in the order of 50 N is created here along with the associated moment. Considering the weight of the pipe and added mass of the fluid, it is clear that the pipe will not center quick enough to explain the observed measurements.

E

Experiment - design and execution

E.1. Test philosophy

When designing an experiment, it's goal should be clear. The reason for performing this experiment in order of importance are:

1. Improve understanding of the phenomena governing swab and surge pressure (influence of velocity, acceleration, local losses, gel strength)
2. Determine the reliability of the model under normal conditions
3. Check the robustness of the model (does it work for unusual movement, is it applicable if the assembly rotates, etc.)

Because model performed well in predicting the pressures measured by Burkhardt, it is assumed that the influence of rheology and mud clinging are well captured in the model. Therefore, the initial idea of performing a test with water instead of drilling mud as a validation step was abandoned. Instead the effect of local flow restiction due to a cone is investigated.

E.2. Constraints

Due to constraints in timing and funding the author was not entirely free to design an experiment from scratch. These constraints were:

- The wellbore would be 13-3/8" 68lb/ft casing
- The wellbore should not be deeper than required
- All tubulars should be standard sizes (ID, OD, length) preferably in stock at the Rijswijk facilities
- No more than 3-5 days of rig time
- The drilling mud must contain at least 4% starglide oil (to serve as a lubricant during the next test)
- Drilling mud properties were unlikely to match the requested properties
- The well is vertical
- Two pressure sensors are available, recording range 0-100 and 0-250 bar absolute pressure with measurement precision of ±0.1 % and a sampling frequency of 2 Hz
- The velocity and position of the cone will be measured at 10 Hz
- Maximum velocity 300 mm/s.
- The maximum stroke length is 10m

In addition, due to the rig configuration, available time, and standard safety procedures some additional constraints were present:

- The hydrostatic pressure was not constant during tests. Displacement of mud by the drillstring resulted in the surface level, and thus hydrostatic pressure, variation during the experiment

- The casing used to form the BHA had to be filled with mud and in open connection to the wellbore, thus mud flowed in and out of the top of the assembly. This resulted in non instantaneous hydrostatic pressure variations due to displacement as the flow between the wellbore and the assembly was restricted.
- All components had to be tapered to prevent them from getting caught on edges
- Welding seems were not removed

E.3. Experimental set up

E.3.1. Overview

With the aim of the experiment in mind the set up is designed. It is vital to ensure that the generated pressures are sufficiently large for the pressure sensors to record them. However, not so large that the drillstring would buckle during surge tests (10 ton compressive force) or that vacuum pressures were approached during swab tests. Keeping all aforementioned constraints in mind, the configurations depicted in figure E.1 are selected. Before the test, the diameters of the pipes and the cones were measured to verify the dimensions. The host casing ID is measured at 4 locations and the BHA casing OD measured at 6 locations.

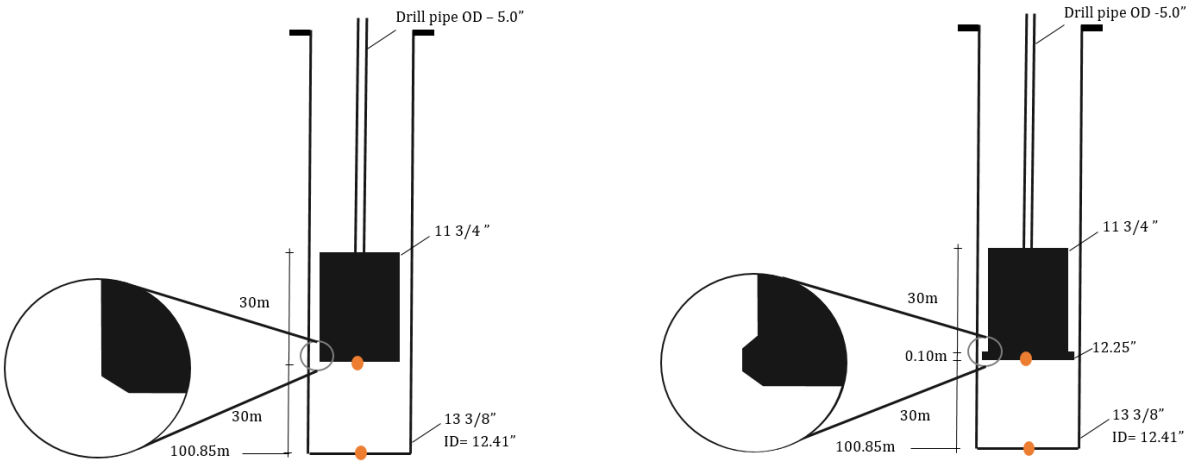

Figure E.1: Schematic of experiment design. Flush assembly on the left and coned assembly on the right. Pressure sensor locations indicated in red.

E.3.2. Components

Cones

As mentioned two different cones are used: one flush with the assembly and one which protrudes from the assembly, restricting annular flow. Both cones were to host a pressure sensor which is to be attached on the inside of the BHA and which is to measure pressure below the cone. Below the design and actual cones are pictured.

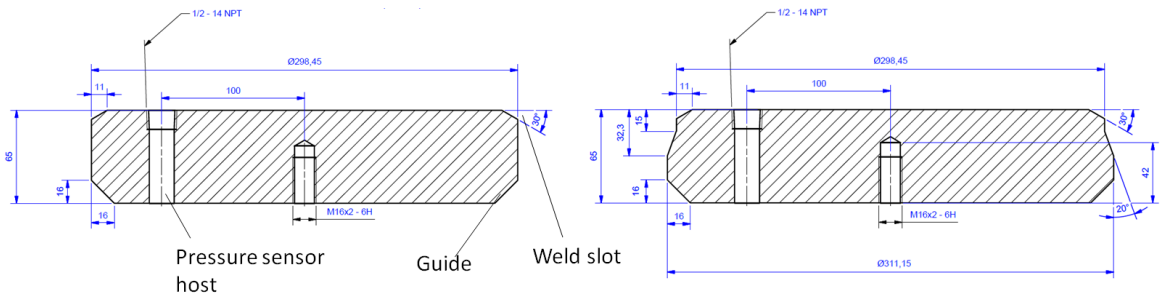

Figure E.2: The cones, flush (left), and coned (right) technical drawings by Koen Castelein, assistant research engineer.

Figure E.3: The cones, flush (left), and coned (right)

Cross-over

The casing used to make the BHA has to connect to drillstring. This is done with cross-over unit. The crossover must have a screw thread similar to that on the drill pipe on one end and a diameter equal to the BHA at the other end. It is also perforated to allow mud to flow into the BHA and drillstring to prevent them from becoming buoyant. The design drawing, and real object are presented in Figure E.4.

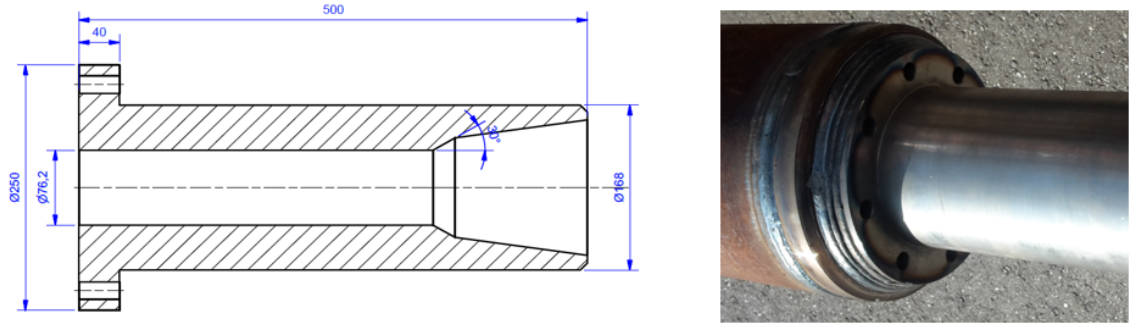

Figure E.4: Cross-over design and actual piece showing the perforations which allowing the BHA to fill with mud

Drilling mud

A bentonite (clay) and water based mud was ordered with the properties as listed in table E.1. Bentonite based mud was selected due to its stability. Its properties should not vary a lot over time and settlement of particles should be minimal resulting in a fairly homogeneous mud.

Table E.1: Design mud properties

Property	Value	Unit
Plastic viscosity (PV)	30	[cP]
Yield point (YP)	30	[lb/100ft^2]
Density (ρ)	1190	[kg/m^3]

Wellhead

The design of the wellhead matters because it is important input in determining the total depth of the well. During the experiment the position (depth) of the bottom of the cone was recorded relative to the rig floor. The following wellhead and well depth drawing is used to determine the distance between rig floor and bottom hole.

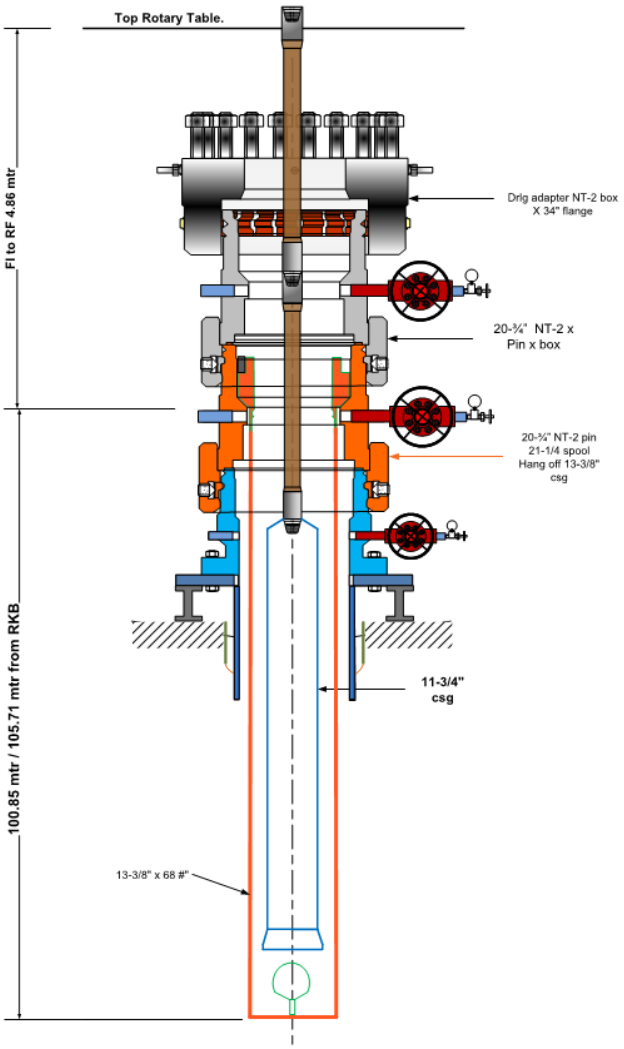

Figure E.5: Wellhead dimensions and depths relative to the rig floor. Drawing provided by the test rig team

Pressure sensors

The two *AE sensors DLN 70* pressure sensors are capable of measuring a maximum pressure of 100 and 200 bar. However, the casing protecting the electronics fails at 20 bar. Although pressures exceeding 20 bar are not expected, protective housing is made for both sensors. The housing of the sensor to be placed at the bottom of the well is equipped with two guides, to keep it upright in the well and elevated above potential debris. A metal wire loop is also attached so that it can be lowered into the hole and later 'fished' out with a hook attached to a wire.

Figure E.6: Pressure sensor in the cone (left), pressure sensor for the bottom (middle), and a sensor without its protective housing (right)

Rig specifications

The Rijswijk test rig specifications are given in the image below

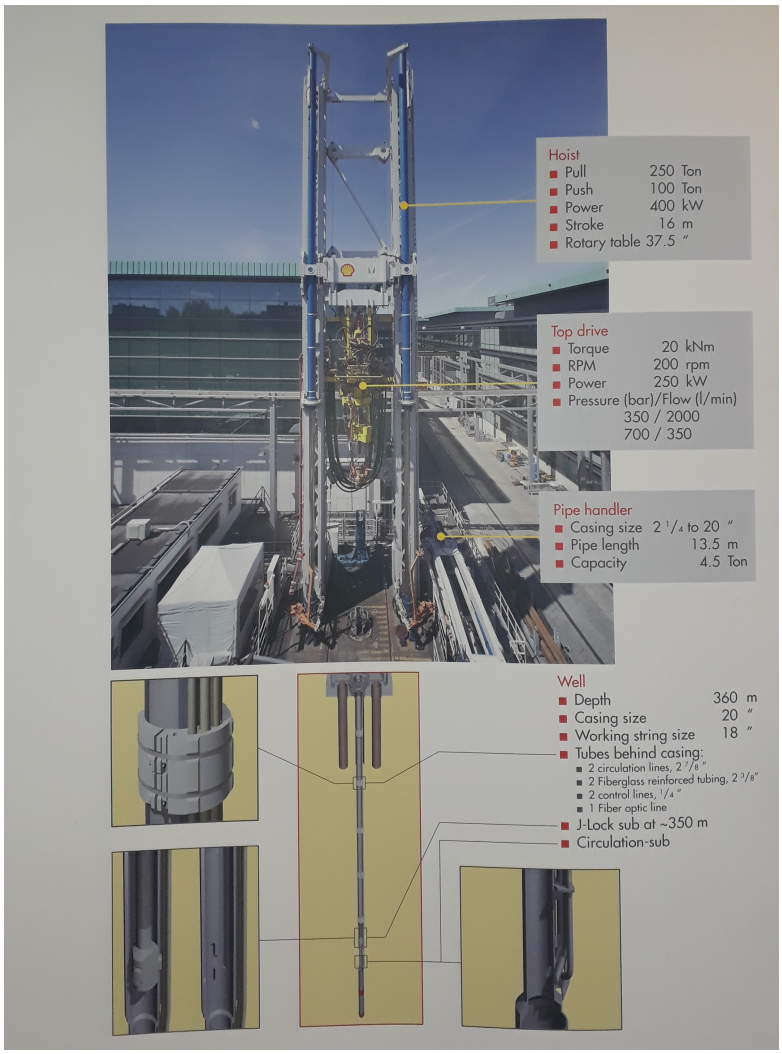

Figure E.7: Rijwijk test rig specifications

E.4. Test procedure

Considering the goal of the experiment, it is important to perform multiple movements with various velocities, accelerations, waiting times etc. so that enough insightful data can be gathered. In addition, the displacement of the rig's top drive in time must be known so that the velocity and accelerations can be accurately determined. These should then be matched to the pressure data. Accurate measurements of the mud properties are also required as input. The BHA movement and mud sampling are covered in more detail in the following sections.

E.4.1. BHA movement

Several velocity profile are suggested by the author. The shape and philosophy behind each profile will be discussed. As the speed of the topdrive (which moves the drillstring and in turn the BHA) in controlled manually through a joystick and speed dial, it is very difficult for the rig operator to reproduce the proposed movement and equally hard to achieve repeatability. The velocity profiles are provided in figure E.8.

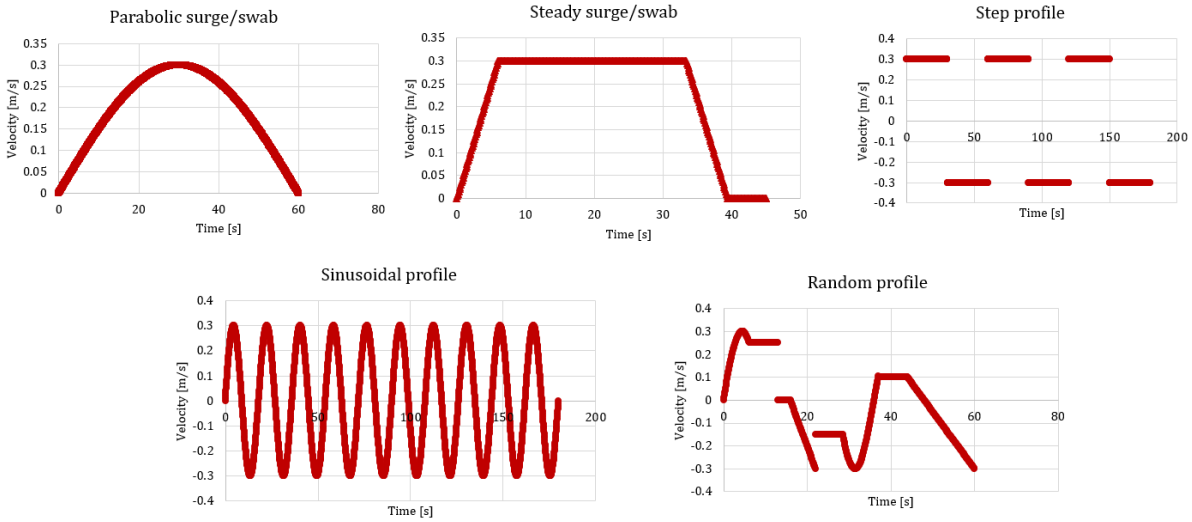

Figure E.8: Proposed velocity profiles

Parabolic surge/swab

This profile is included to see how pressures are formed when the fluid is subject to a gradual but constant acceleration. No steady state should ever be reached here. This movement is applied in both an upwards and downwards direction. This movement proved to be particularly difficult for the rig operator to perform.

Steady surge/swab

This profile is included to investigate the steady state. It is performed at various speeds to see how the pressures losses in the steady state vary with speed. Together with the parabolic profile it most closely resembles movements performed in the field. It is performed in both directions (tripping in and out). It is also performed once in both directions with the assembly rotating at 35 rpm to investigate the influence of rotation.

Step profile

Here we seek to apply a harsh acceleration to the fluid followed by a continues velocity. This should tell us how the fluid reacts to sudden movement and how potential peaks dampen out. It is performed at different speeds.

Sinusoidal profile

Here we attempt to continuously disturb the fluid inducing very irregular and unsteady flow.

Random profile
Here we want to test all possible movements a rig could apply to the BHA to test the robustness of the model. These kind of jerky, random movements are sometimes performed in the field to wiggle the assembly past downhole obstacles.

E.4.2. Testing sequence

Below the runs are presented in sequence, the sequence matches the sequence in which the results are presented in Appendix G.

Table E.2: Test assembly movements

Movement number	Description	Starting bit depth	Rotation	Waiting time [min] (before next run)
1	Parabolic swab	75m	-	2
2	Parabolic surge	65m	-	2
3	Parabolic swab	75m	-	2
4	Parabolic surge	65m	-	2
5	Step profile (full speed)	75	-	2
6	Step profile (full speed)	75	-	2
7	Step profile (half speed)	75	-	2
8	Step profile (half speed)	75	-	2
9	Random	-	-	2
10	Random	-	-	2
11	Steady surge (full speed)	65	-	2
12	Steady swab (full speed)	75	-	2
13	Steady surge (half speed)	65	-	2
14	Steady surge (half speed)	75	-	2
15	Steady swab (half speed)	65	Yes	2
16	Steady swab (half speed)	75	Yes	5
17	Steady surge (full speed)	65	-	5
18	Steady swab (full speed)	75	-	10
19	Steady surge (full speed)	65	-	10
20	Steady swab (full speed)	75	-	15
21	Steady surge (full speed)	65	-	15
22	Steady swab (full speed)	75	-	2
23	Sinus	-	-	2
24	Sinus	-	-	-

E.4.3. Mud sampling and testing

Comparing the measured pressures with computed pressures is meaningless if the mud properties are not well known. Therefore rigorous testing of mud samples is required to determine the properties during the testing days.

HAAKE MARS rheology
On each day during which an experiment is performed, a HAAKE MARS Viscometer performs a full analysis of the rheology. The viscometer is an very sensitive and accurate viscometer providing reliable data. It is used to:

1. Determine the mud rheology curve between a shear rate of 1 and 1000 [1/s]. Shear rate increase is logarithmic.
2. Determine the rheology curve between a shear stress of 0.05-50 [Pa]. Waiting time is 0 min. Shear stress increase is logarithmic.

3. Determine the rheology curve between a shear stress of 0.05-50 [Pa]. Waiting time is 2 min.Shear stress increase is logarithmic.
4. Determine the rheology curve between a shear stress of 0.05-50 [Pa]. Waiting time is 5 min.Shear stress increase is logarithmic.
5. Determine the rheology curve between a shear stress of 0.05-50 [Pa]. Waiting time is 10 min.Shear stress increase is logarithmic.
6. Determine the rheology curve between a shear stress of 0.05-50 [Pa]. Waiting time is 15 min.Shear stress increase is logarithmic.

Step one is taken to produce a smooth rheology curve. Steps 2-6 are used to determine the yield stress (τ_y) for various waiting times.

Figure E.9: HAAKE MARS viscometer

Fann viscometer rheology

In oil field practice, a Fann viscometer is often used to determine the mud's rheology. Although much less accurate than the HAAKE it is a much cheaper machine and the results are more convenient to analyze. A mud sample is to be tested with the Fann viscometer at least once every four hours during testing. This is done as a back up to the HAAKE analysis, and is educational for the author.

Figure E.10: Fann Viscometer

Density
The drilling mud's density is determined with a mud scale. The samples are weighted after they have been tested with the Fann viscometer. The Fann should remove some of the air bubbles, making the density measurement more accurate

Figure E.11: Mud scale

E.4.4. Schedule
An outline of the testing schedule is given below

Table E.3: Testing schedule

Action	Day	Time (approximately)
1st sensor placed at the bottom	24/08	13:00-16:00
Assembly lowered in place	25/08	07:00-10:00
Hole filled with mud	25/08	11:00-12:00
Test with flush cone	25/08	12:00-15:00
Pulling out the assembly	28/08	07:00-10:00
Retrieving sensors and downloading data	28/08	10:00-12:00
Placing bottom sensor, lowering assembly	28/08	13:00-16:00
Replacing mud spilled while pulling out	29/08	08:00 - 9:00
Test with protruding cone	29/08	09:00-13:00
Pulling out assembly and downloading data from cone sensor	29/08	14:00-16:00
Retrieving sensor from the bottom and downloading data	30/08	07:00-9:00

F

Experiment - Data collection & processing

F.1. Dimensions

F.1.1. Pipe Diameters

The diameters of the pipes used to form the assembly and the host casing were measured at each end. Not all host casing pipes could be measured due to subsequent tests. The pipes showed some ovality and the largest and smallest diameter at each cross section is given. Diameters were measured with a caliper gauge.

Table F.1: Measurements of the host pipes' (13.375") diameters

Pipe end	Maximum ID [mm]	Minimum ID [mm]	Average [mm]
1	317.5	315.5	316.5
2	316	315.5	316.3
3	317	315	316
4	316.5	317	316.8
Average	317	316	**316.4 (12.46")**

Table F.2: Measurements of the assembly pipes' (11.75") diameters

Pipe end	Maximum OD [mm]	Minimum OD [mm]	Average [mm]
1	301	298.5	299.8
2	301	299	300
3	300	298	299
4	300.5	298.5	299.5
5	301	300	300.5
6	301	299	300
Average	300.8	298.8	**299.8 (11.80")**

F.1.2. Component dimensions

Wellbore geometry and cones

The cones are welded to the assembly and thus some welding seams were present. The mud did not completely fill the well, and as explained in the previous section, the measured diameters of the pipes deviated from the design diameter. The resulting well geometry is depicted below.

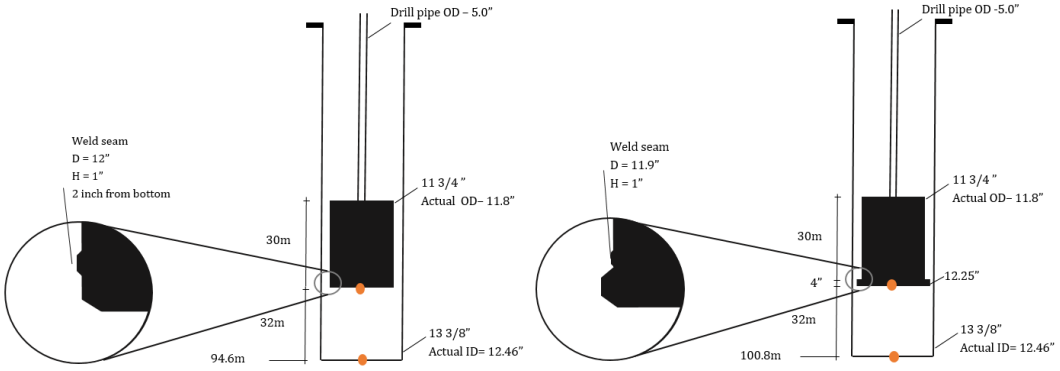

Figure F.1: Measured well geometry

Crossover

The crossover was measured to ensure the actual dimensions match the design dimensions. The measurements are summarized below:

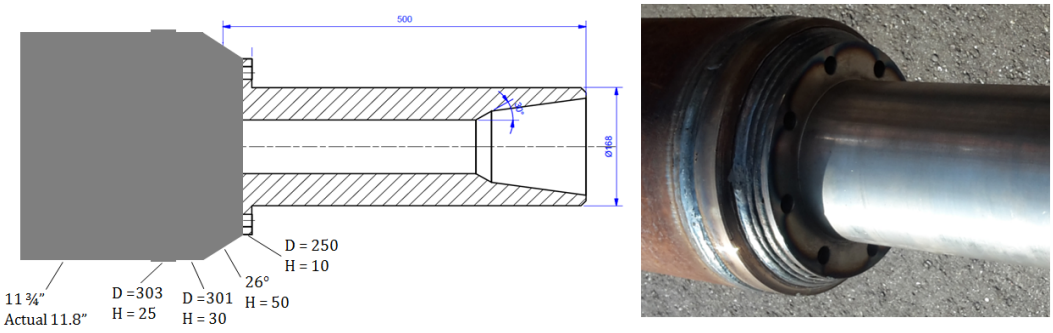

Figure F.2: Measued dimensions of the crossover piece

F.2. Mud properties

F.2.1. Rheology

The working fluid's rheology is measured by two separate pieces of equipment. Firstly, a HAAKE MARS rheometer was used for accurate rheology measurement. Secondly, a Fann viscometer was used. A Fann viscometer is a simple rheometer and is the most frequently used rheometer in the field. It was used mainly out of curiosity. The HAAKE data is used for futher analysis. For each test day, a mud sample was analyzed according to the procedure outlined in the previous chapter. The results are plotted in Figure F.3.

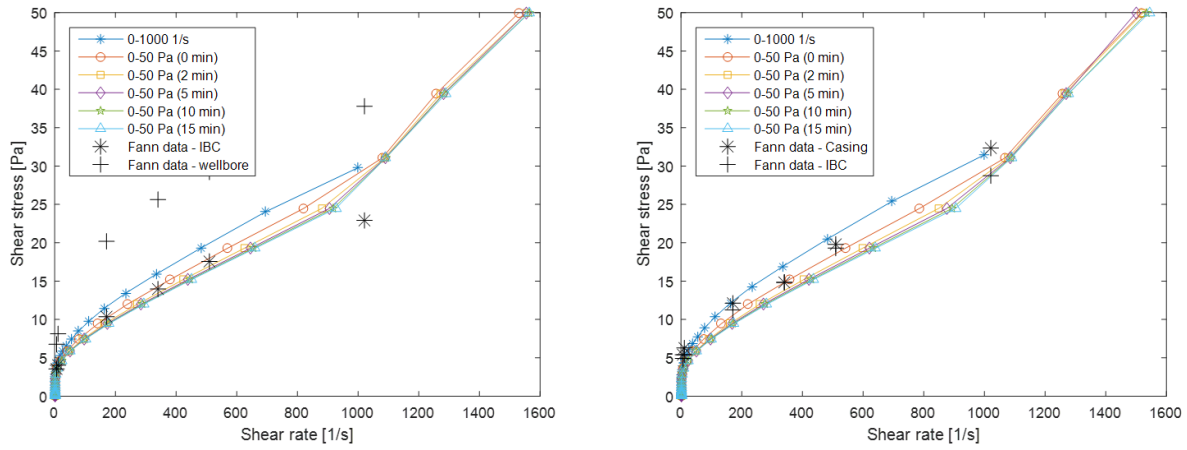

Figure F.3: Rheology measurement results for the flush assembly (left) and the coned assembly (right)

The mud is stable, meaning its properties did not change significantly during the test's duration. The rheology changes during the measuring of one sample yet all samples show this behavior. This indicates that their are either time-dependent or temperature-dependent effects at work. For the calculations, the data points for two minute waiting time data is used. The data points from the samples from both tests and the curve fit through them are provided below. An uncertainty range of 15% is used as this is the accuracy a lab technician can generally achieve [36].

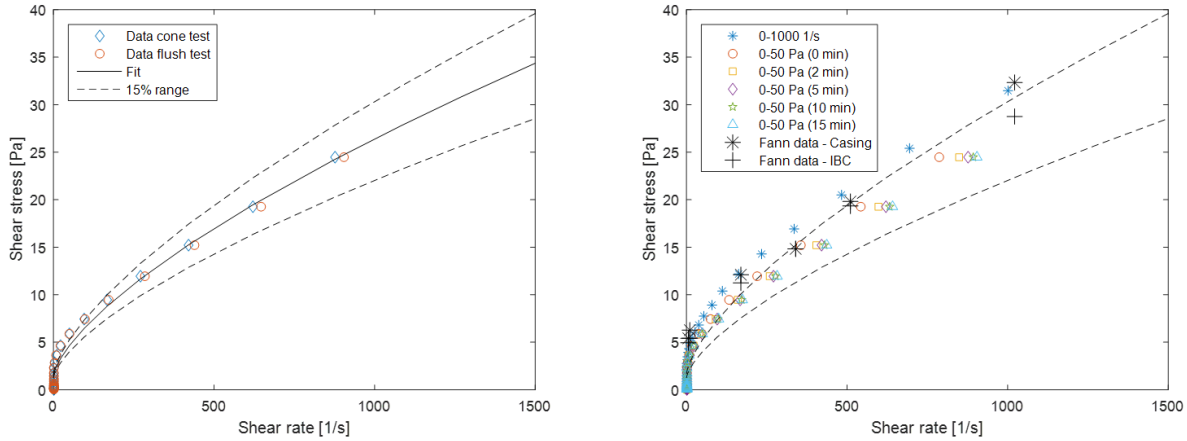

Figure F.4: Rheology curve used for modelling and uncertainty range (left) and the original data and the uncertainty range (right)

F.2.2. Density

The mud density was measured multiple times. Samples were taken from the Intermediate Bulk Containers (IBC), large tanks used to store extra mud, and from inside the BHA once it was tripped out. The mud balance provides the density in standard gravity (s.g.). This unit is multiplied by 1000 to obtain the density in kg/m^3.

Table F.3: Mud denisty measurements

Sample source	Density [s.g.]	Comment
Delivery truck	1.18	-
ICB (flush)	1.19	-
Well	0.83	Discarded
Assembly (flush)	1.19	-
ICB (cone)	1.20	-
Assembly (cone)	1.18	-
Average	**1.19**	

F.3. Rig data

The rig computer measured and recorded the top drive's position at roughly 10 Hz. From this the velocity is automatically calculated. The rig data was smoothed in MATLAB to remove any non-physical accelerations which were observed due to noise in the data.

F.4. Pressure data

F.4.1. Data selection

Pressure was recorded both below the assembly by a sensor installed in the cone and at TD. The data retrieved from the cone sensor is difficult to interpret. As it travels with the assembly, it changing depth means the surge/swab pressure is measured along with a change in hydrostatic pressure. It is possible to clean up this data to some degree. Although it requires lots of effort. It is verified for two runs that the cone sensor did not record substantially different value surge/swab value than the sensor placed at TD. Since the data from the sensor at TD is more reliable, this is the data that is used for further analysis.

F.4.2. Data processing

Unfortunately, the rig computer recorded data differently than the pressure sensors. The time trace of the pressure data and rig data not easily correlated. For each run the time axis of the rig and pressure data had to be manually adjusted to correctly connect the two.

Mud near the surface was very foamy and therefore less dense than expected. It would have been very inaccurate to determine the height of the mud column by measuring the mud's surface level. The height of the mud column, i.e. the depth of the well, is used in the calculations is therefore determined as follows. The hydrostatic pressure at the bottom of the well is taken and the atmospheric pressure is subtracted from it. Using the mud's density the height of the mud column is then calculated. Since mud was spilled and the well refilled between the tests, the height of the mud column differs for the two tests. This estimation is good enough as only a negligible amount of swab/surge pressure is developed over the drillsting, nearly all of it is generated over the assembly; the exact height of the mud column is not needed. The used well depths in the modelling are: 94.6 m for the flush test and 100.8 m for the coned test

G

Experiment - Results

G.1. Overview

Table G.1: Test assembly movements

Movement number	Description	Starting bit depth	Rotation	Waiting time [min] (before next run)
1	Parabolic swab	75m	-	2
2	Parabolic surge	65m	-	2
3	Parabolic swab	75m	-	2
4	Parabolic surge	65m	-	2
5	Step profile (full speed)	75	-	2
6	Step profile (full speed)	75	-	2
7	Step profile (half speed)	75	-	2
8	Step profile (half speed)	75	-	2
9	Random	-	-	2
10	Random	-	-	2
11	Steady surge (full speed)	65	-	2
12	Steady swab (full speed)	75	-	2
13	Steady surge (half speed)	65	-	2
14	Steady surge (half speed)	75	-	2
15	Steady swab (half speed)	65	Yes	2
16	Steady swab (half speed)	75	Yes	5
17	Steady surge (full speed)	65	-	5
18	Steady swab (full speed)	75	-	10
19	Steady surge (full speed)	65	-	10
20	Steady swab (full speed)	75	-	15
21	Steady surge (full speed)	65	-	15
22	Steady swab (full speed)	75	-	2
23	Sinus	-	-	2
24	Sinus	-	-	-

G.2. Flush assembly

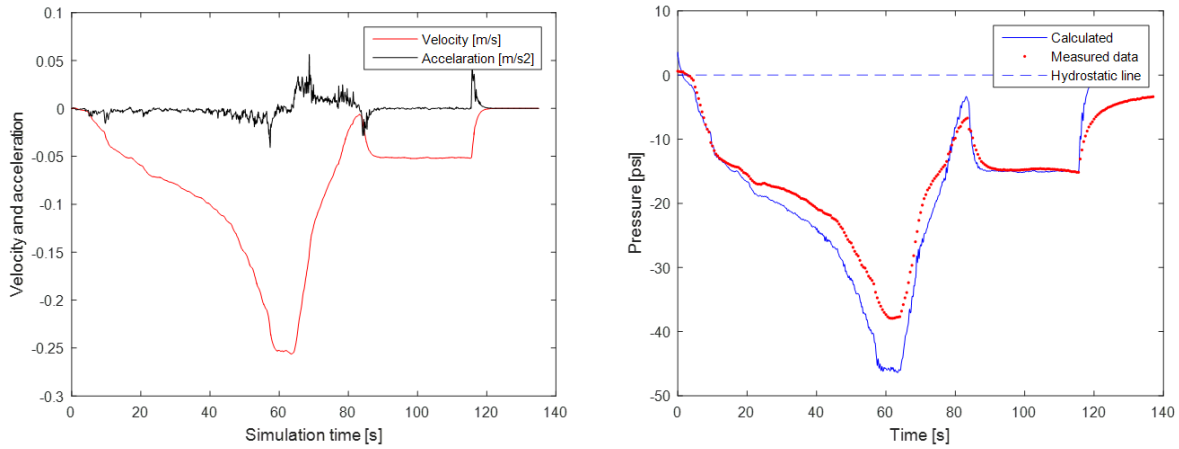

Figure G.1: Flush assembly movement 1, top drive movement (left), measured and calculated surge/swab pressures (right)

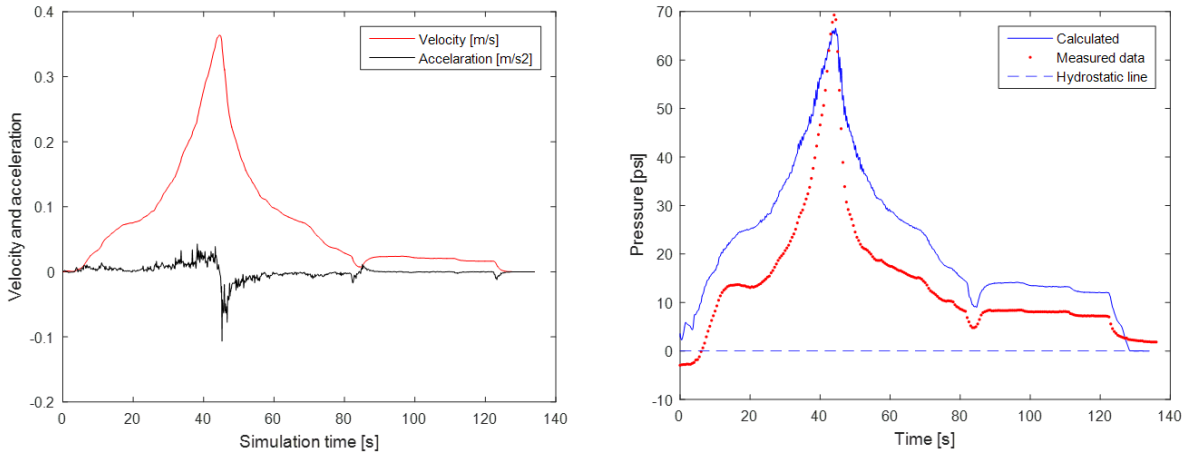

Figure G.2: Flush assembly movement 2, top drive movement (left), measured and calculated surge/swab pressures (right)

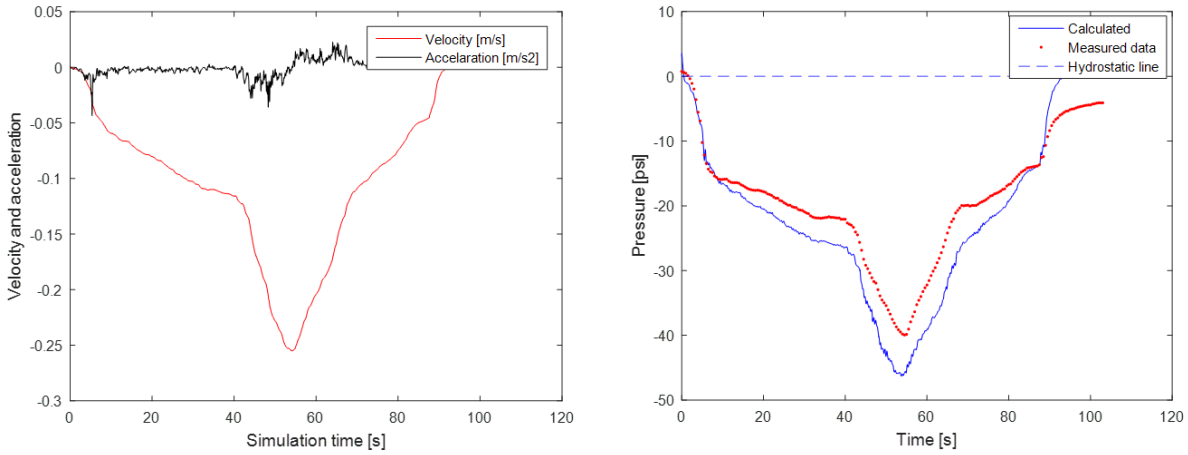

Figure G.3: Flush assembly movement 3, top drive movement (left), measured and calculated surge/swab pressures (right)

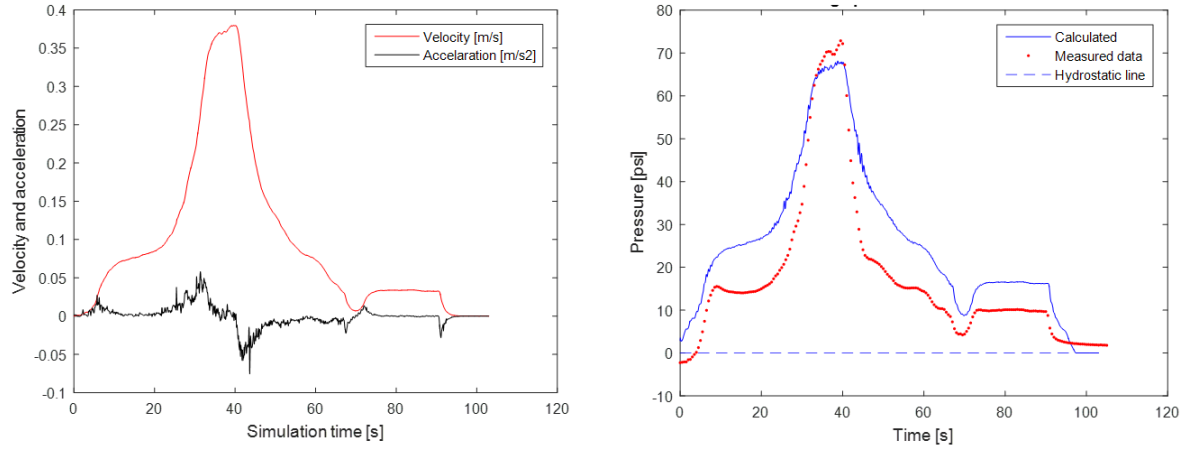

Figure G.4: Flush assembly movement 4, top drive movement (left), measured and calculated surge/swab pressures (right)

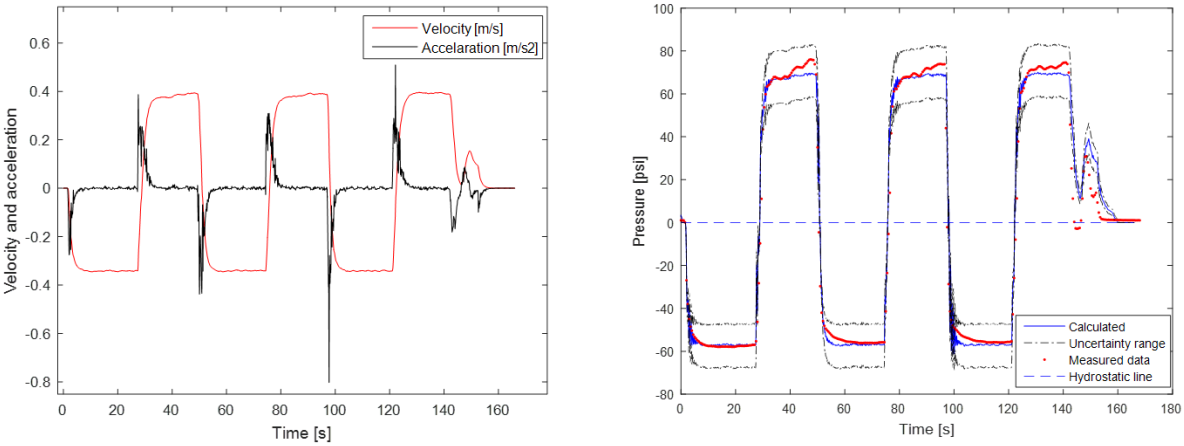

Figure G.5: Flush assembly movement 5, top drive movement (left), measured and calculated surge/swab pressures (right)

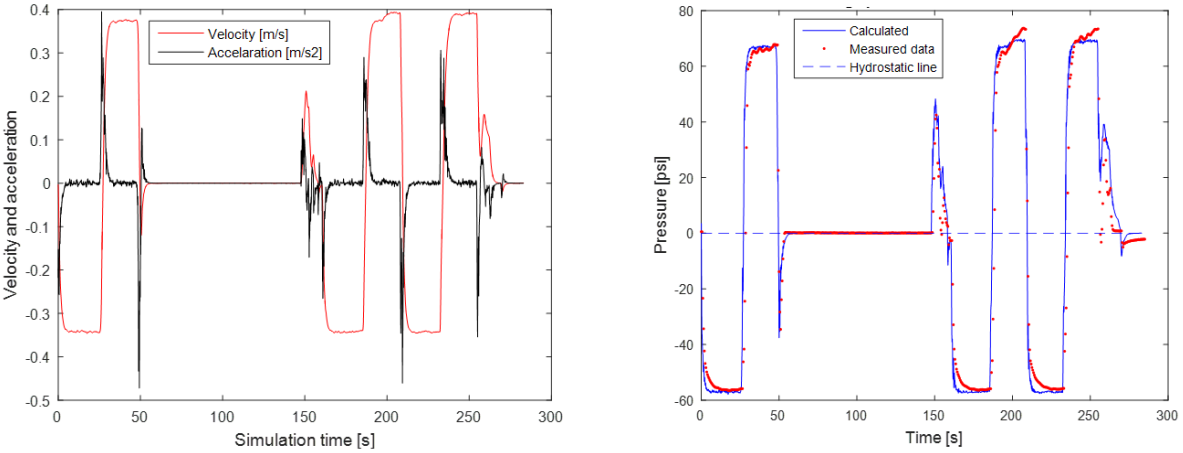

Figure G.6: Flush assembly movement 6, top drive movement (left), measured and calculated surge/swab pressures (right)

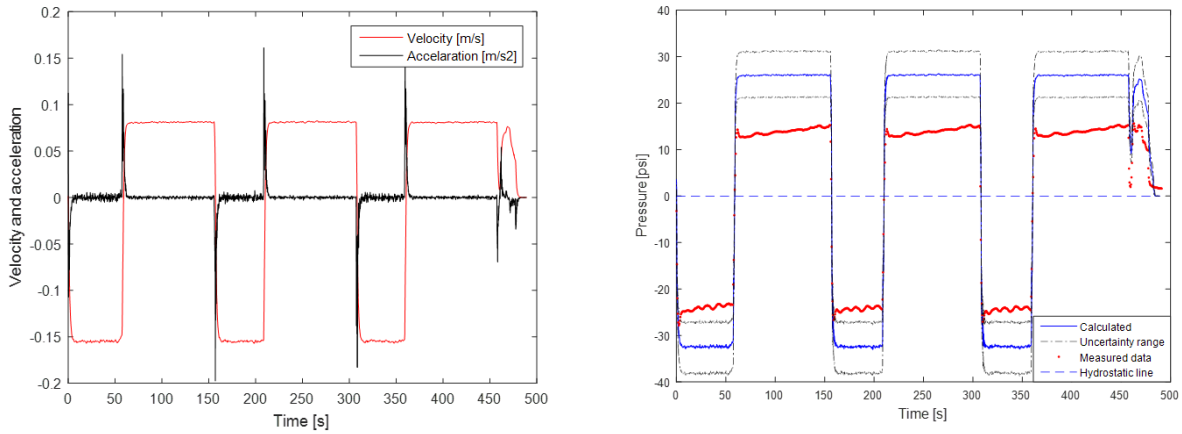

Figure G.7: Flush assembly movement 7, top drive movement (left), measured and calculated surge/swab pressures (right)

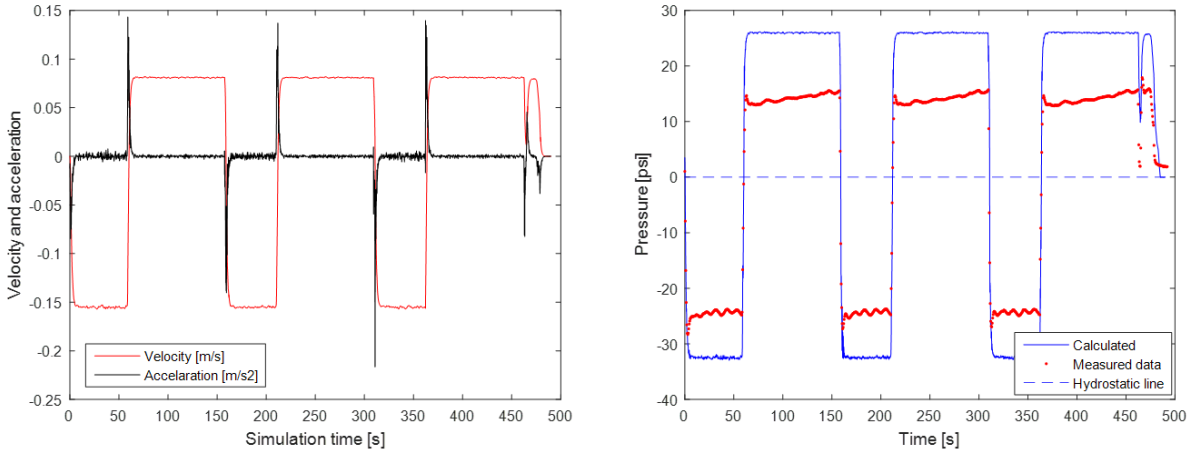

Figure G.8: Flush assembly movement 8, top drive movement (left), measured and calculated surge/swab pressures (right)

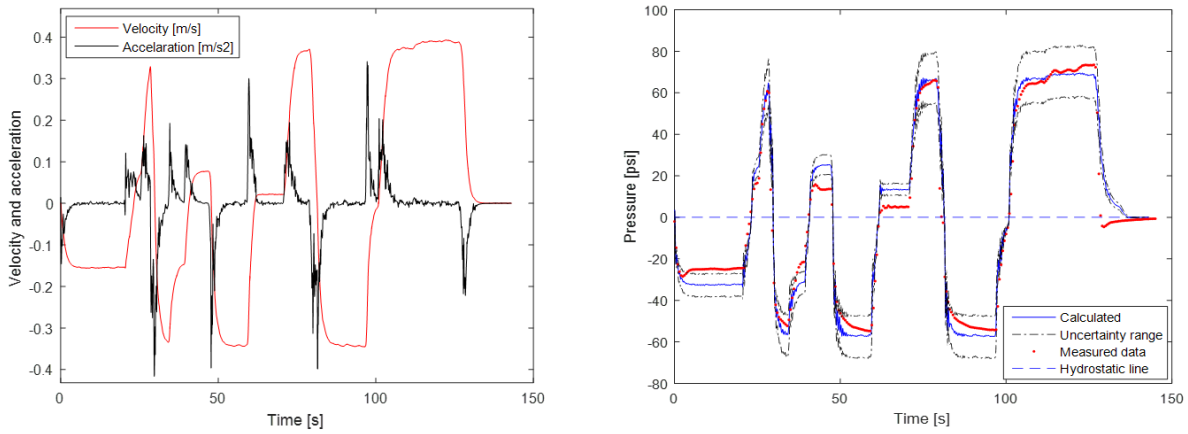

Figure G.9: Flush assembly movement 9, top drive movement (left), measured and calculated surge/swab pressures (right)

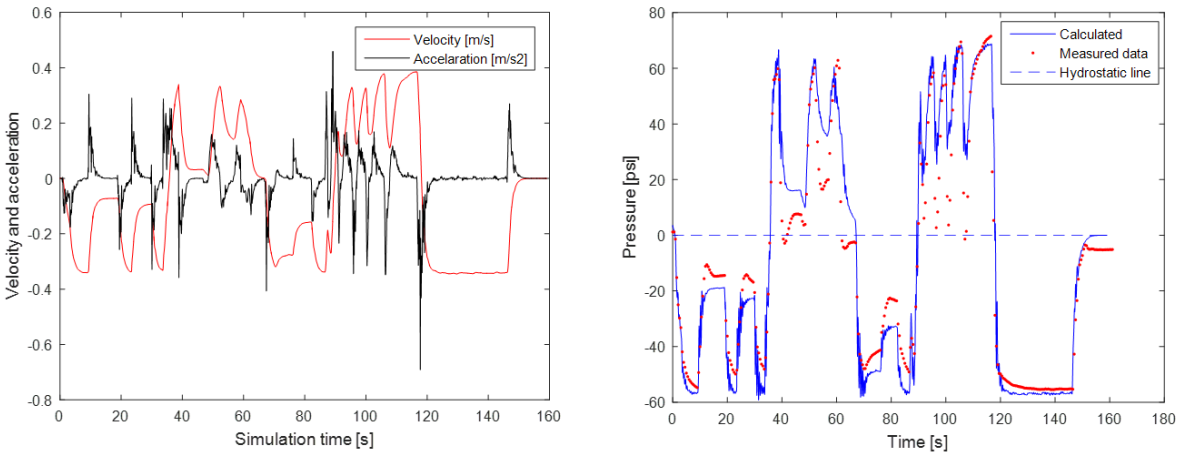

Figure G.10: Flush assembly movement 10, top drive movement (left), measured and calculated surge/swab pressures (right)

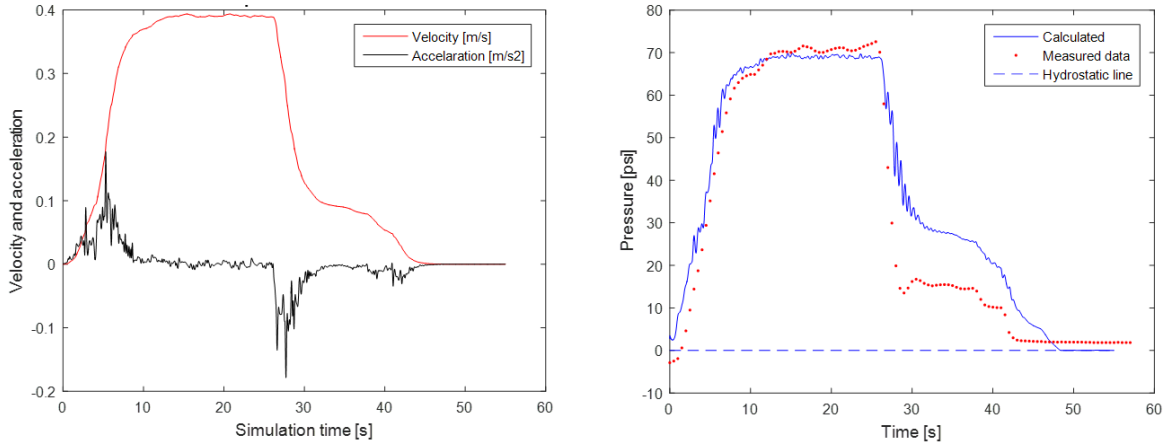

Figure G.11: Flush assembly movement 11, top drive movement (left), measured and calculated surge/swab pressures (right)

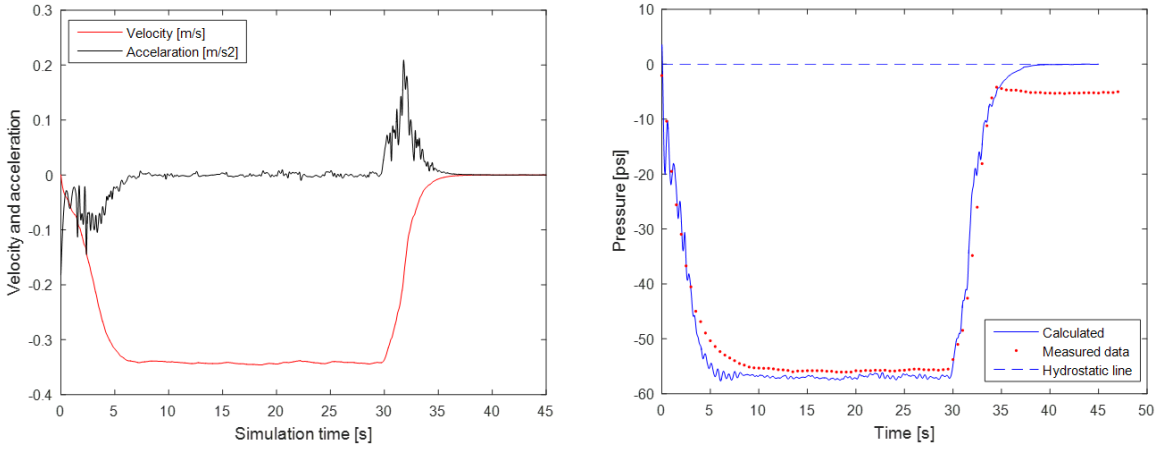

Figure G.12: Flush assembly movement 12, top drive movement (left), measured and calculated surge/swab pressures (right)

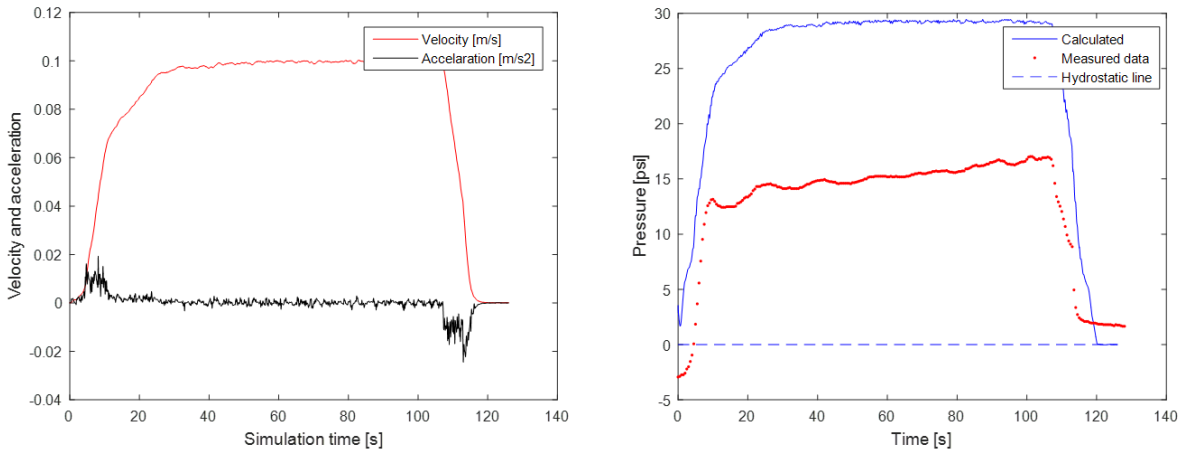

Figure G.13: Flush assembly movement 13, top drive movement (left), measured and calculated surge/swab pressures (right)

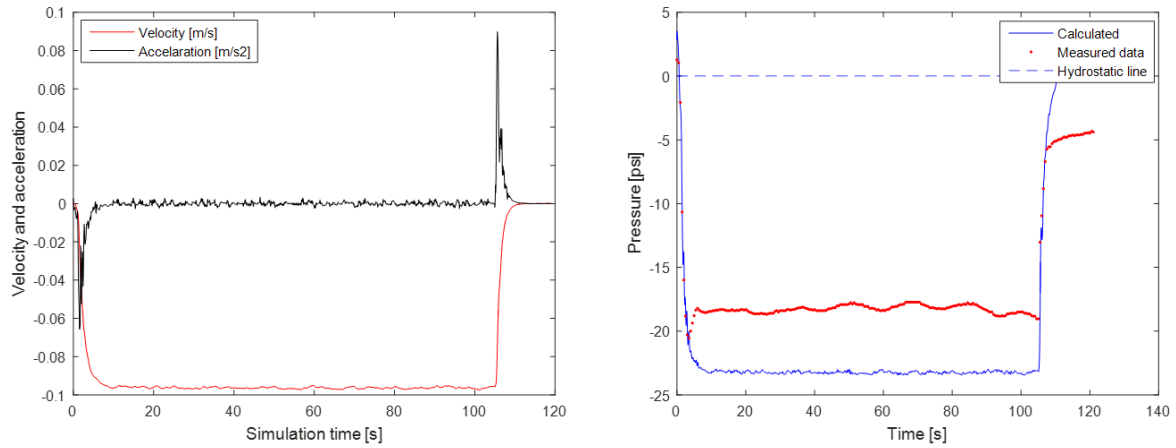

Figure G.14: Flush assembly movement 14, top drive movement (left), measured and calculated surge/swab pressures (right)

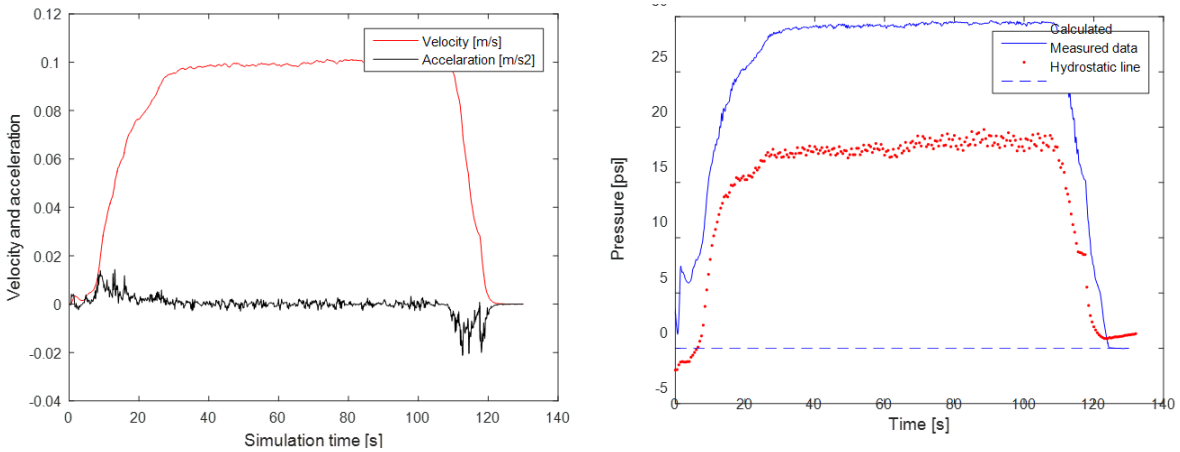

Figure G.15: Flush assembly movement 15, top drive movement (left), measured and calculated surge/swab pressures (right)

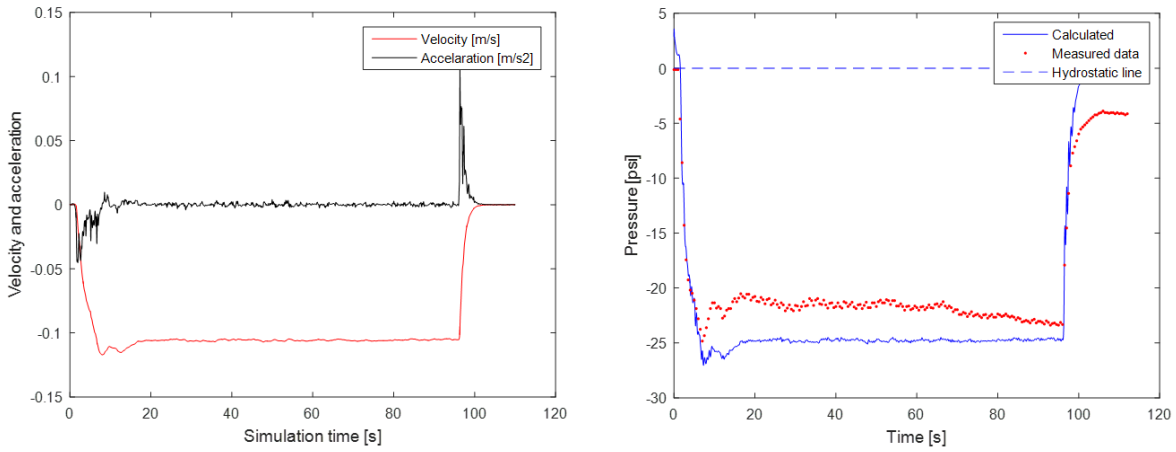

Figure G.16: Flush assembly movement 16, top drive movement (left), measured and calculated surge/swab pressures (right)

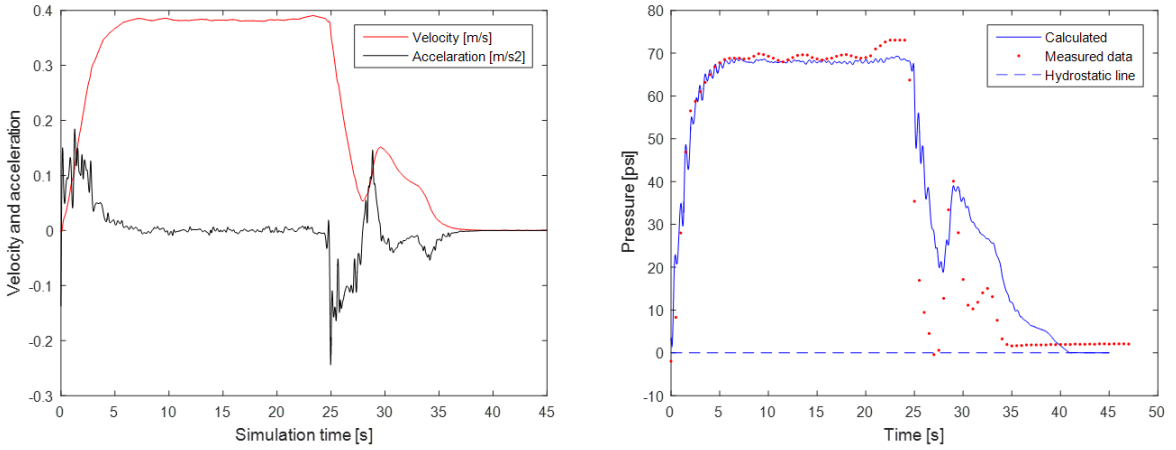

Figure G.17: Flush assembly movement 17, top drive movement (left), measured and calculated surge/swab pressures (right)

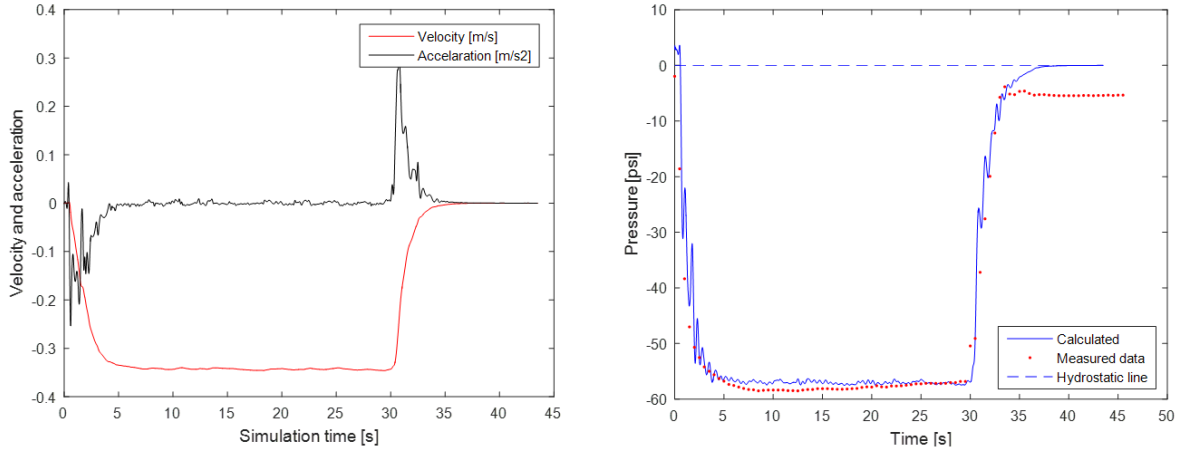

Figure G.18: Flush assembly movement 18, top drive movement (left), measured and calculated surge/swab pressures (right)

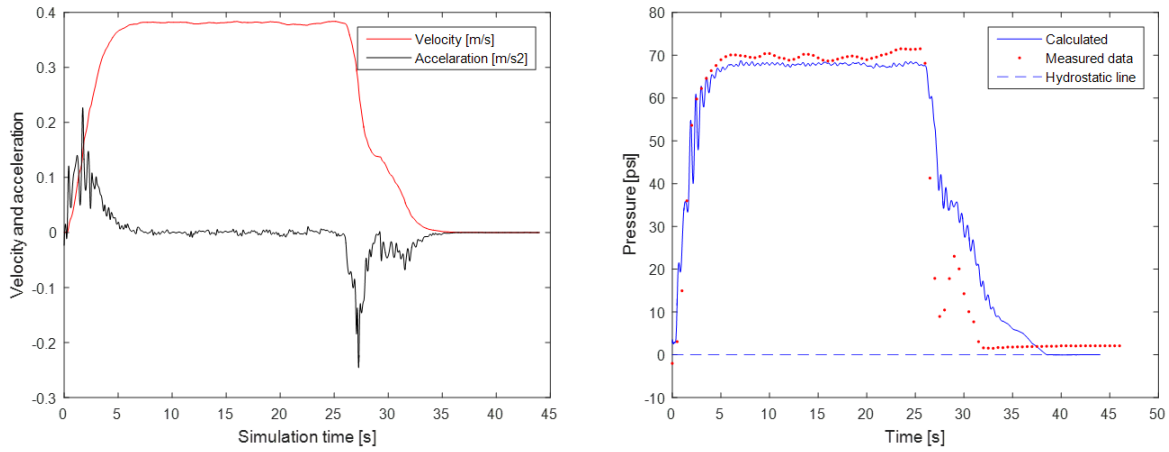

Figure G.19: Flush assembly movement 19, top drive movement (left), measured and calculated surge/swab pressures (right)

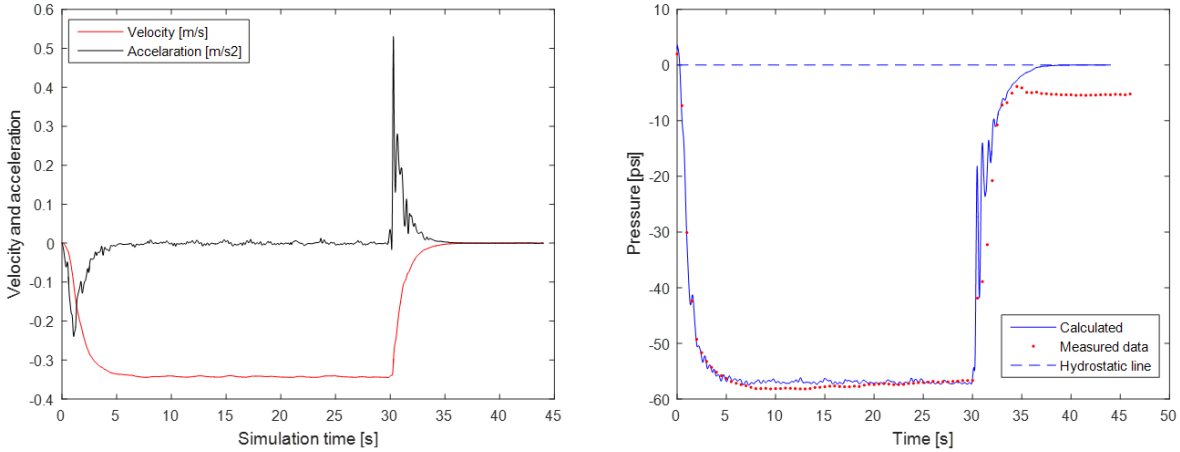

Figure G.20: Flush assembly movement 20, top drive movement (left), measured and calculated surge/swab pressures (right)

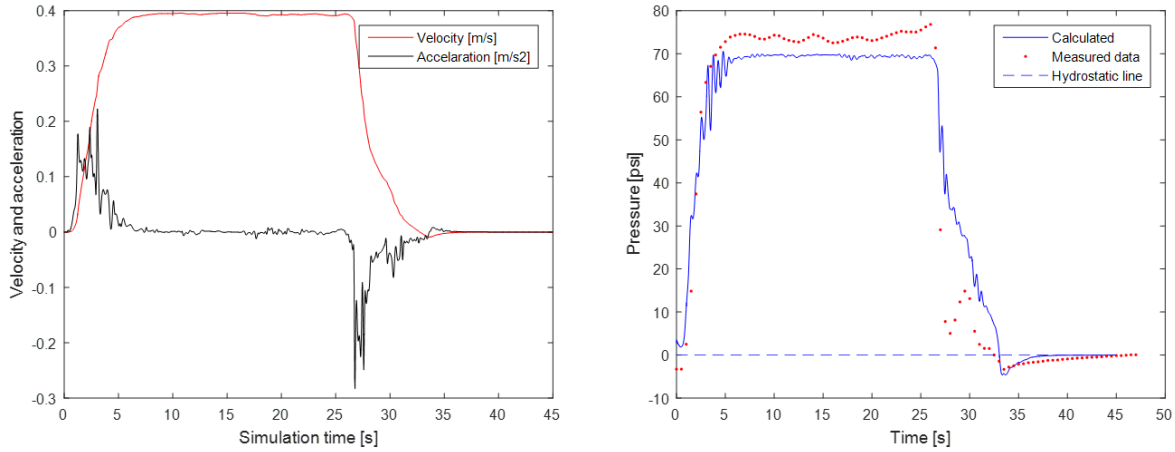

Figure G.21: Flush assembly movement 21, top drive movement (left), measured and calculated surge/swab pressures (right)

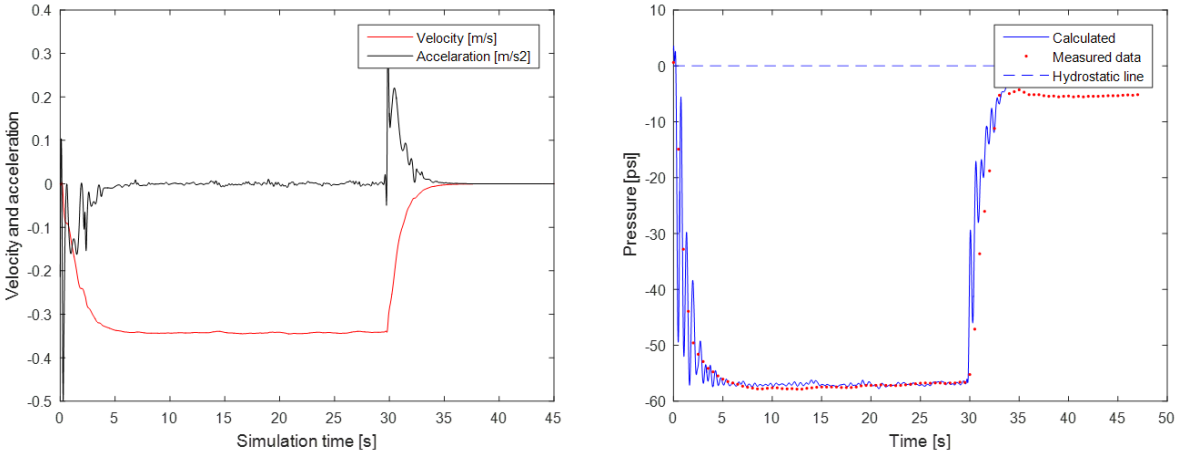

Figure G.22: Flush assembly movement 22, top drive movement (left), measured and calculated surge/swab pressures (right)

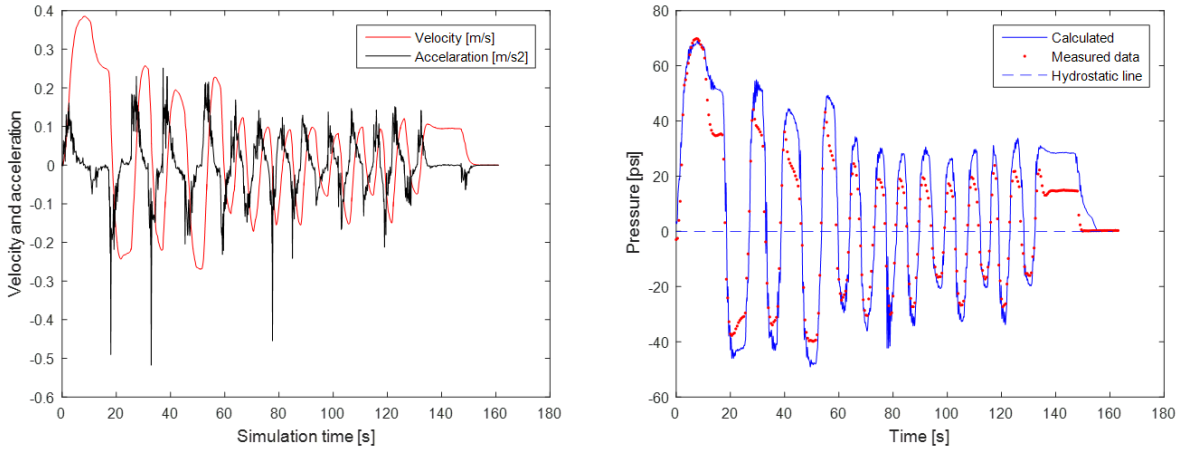

Figure G.23: Flush assembly movement 23, top drive movement (left), measured and calculated surge/swab pressures (right)

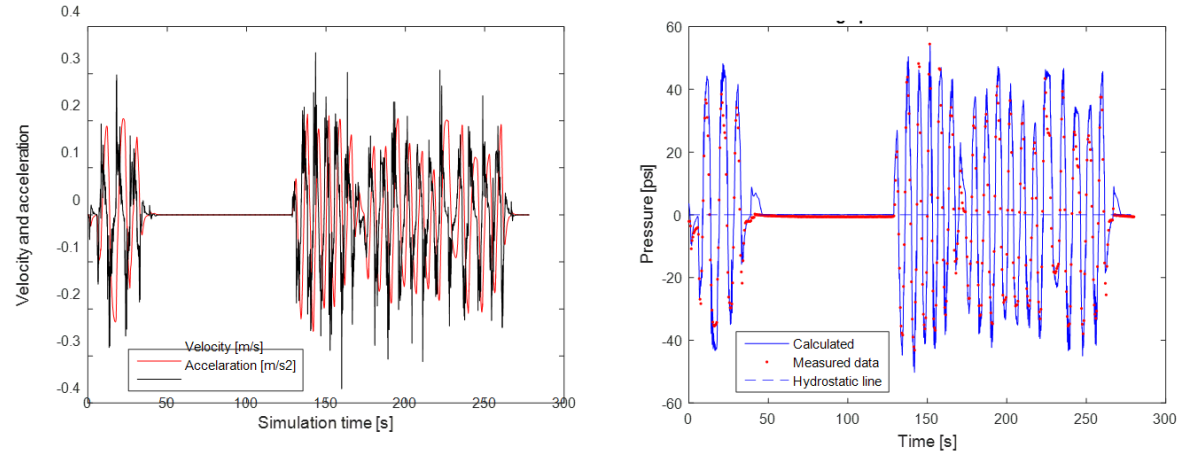

Figure G.24: Flush assembly movement 24, top drive movement (left), measured and calculated surge/swab pressures (right)

G.3. Coned assembly

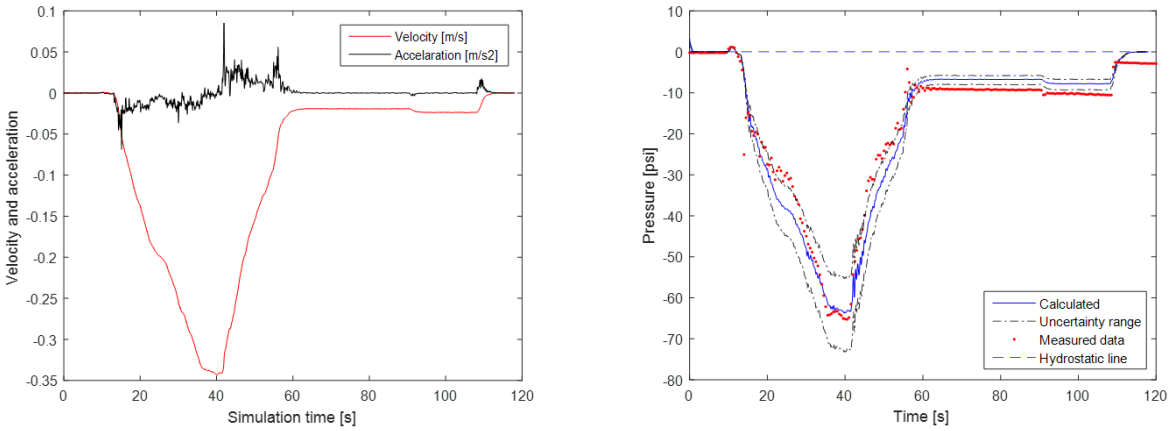

Figure G.25: Coned assembly movement 1, top drive movement (left), measured and calculated surge/swab pressures (right)

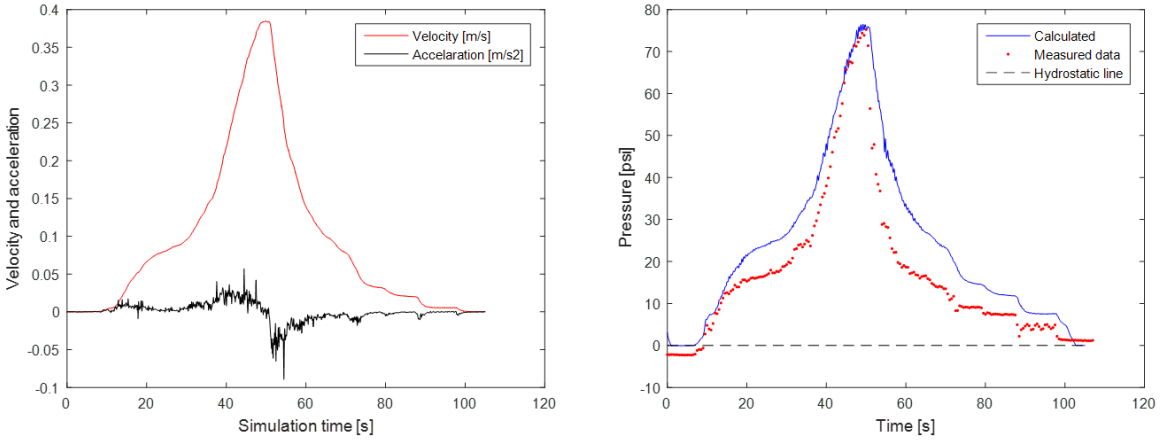

Figure G.26: Coned assembly movement 2, top drive movement (left), measured and calculated surge/swab pressures (right)

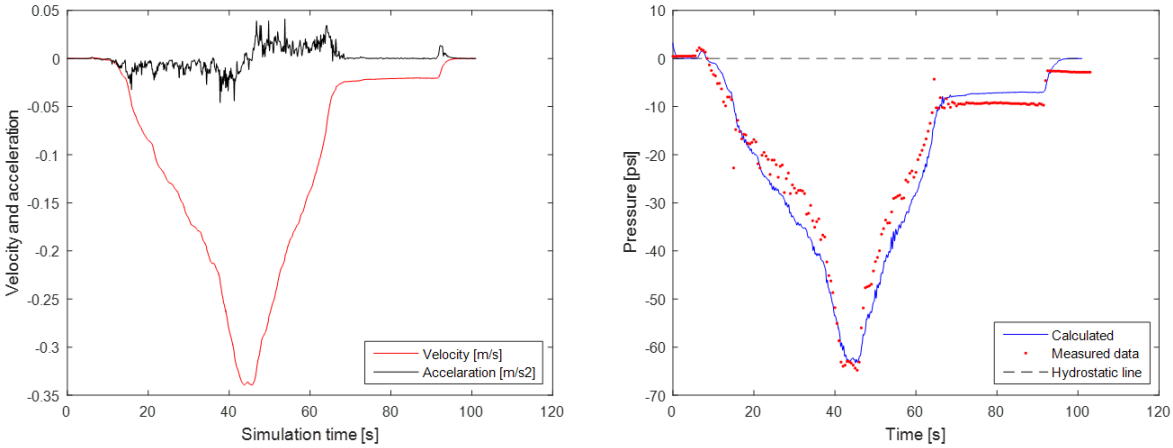

Figure G.27: Coned assembly movement 3, top drive movement (left), measured and calculated surge/swab pressures (right)

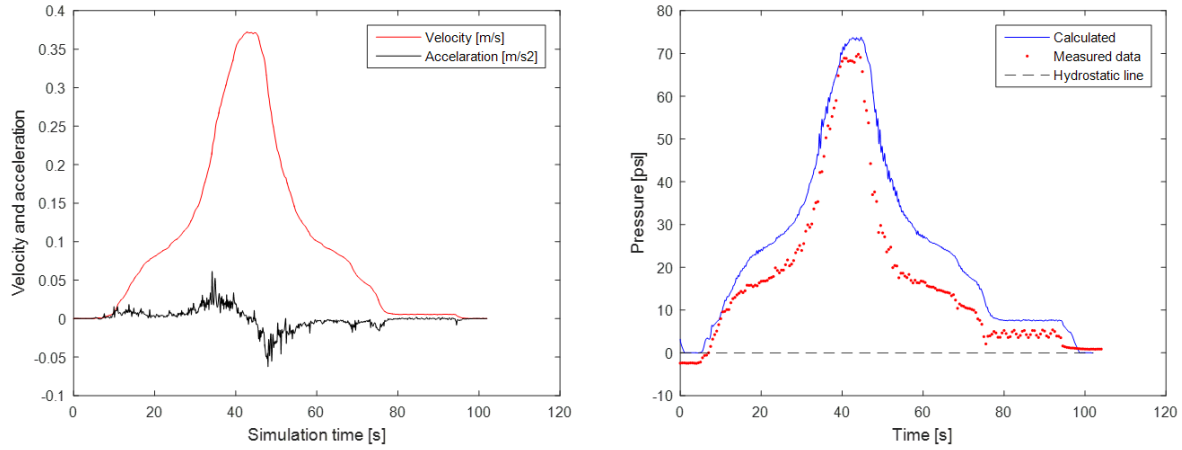

Figure G.28: Coned assembly movement 4, top drive movement (left), measured and calculated surge/swab pressures (right)

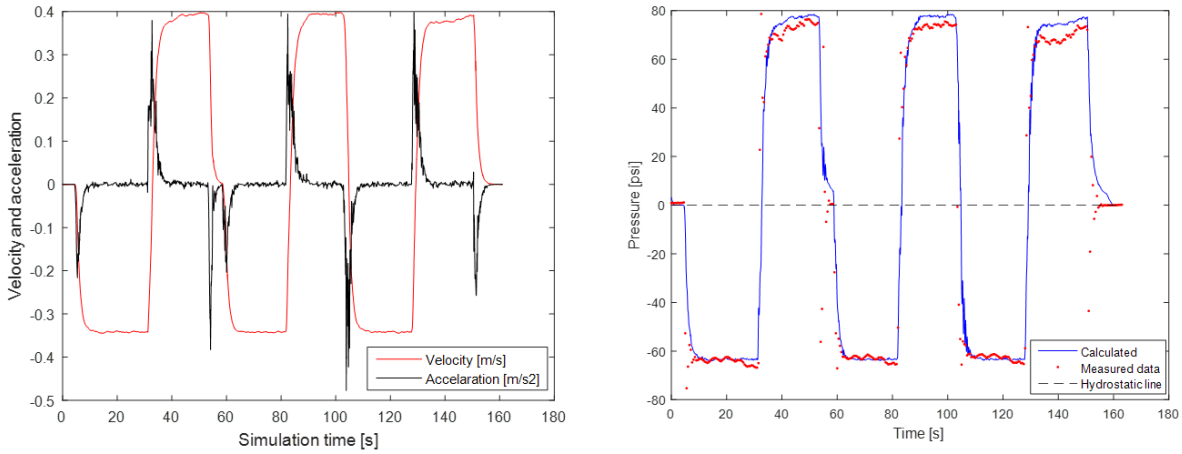

Figure G.29: Coned assembly movement 5, top drive movement (left), measured and calculated surge/swab pressures (right)

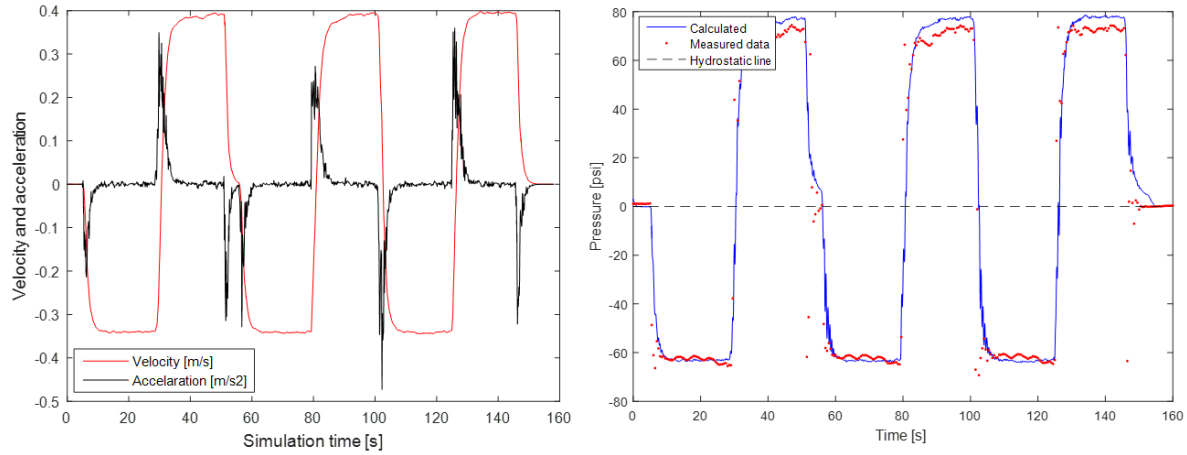

Figure G.30: Coned assembly movement 6, top drive movement (left), measured and calculated surge/swab pressures (right)

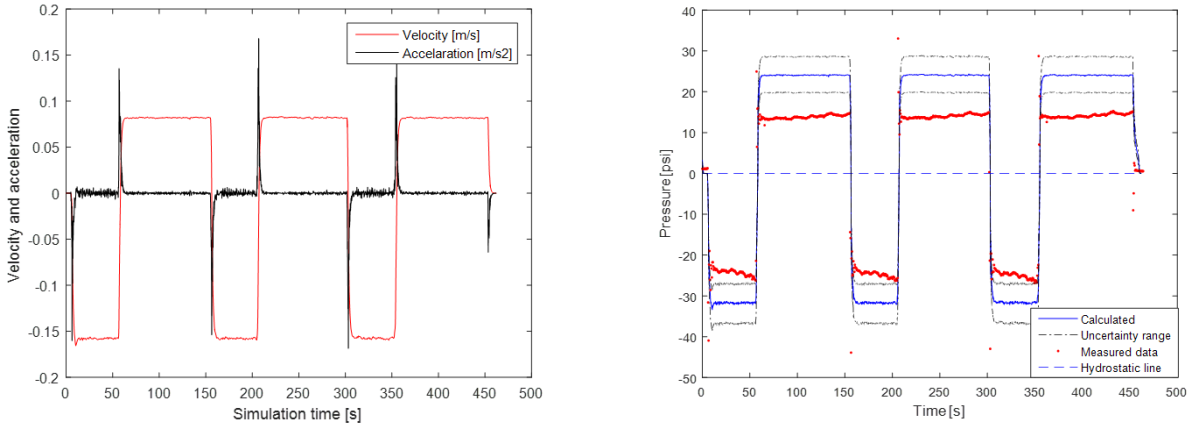

Figure G.31: Coned assembly movement 7, top drive movement (left), measured and calculated surge/swab pressures (right)

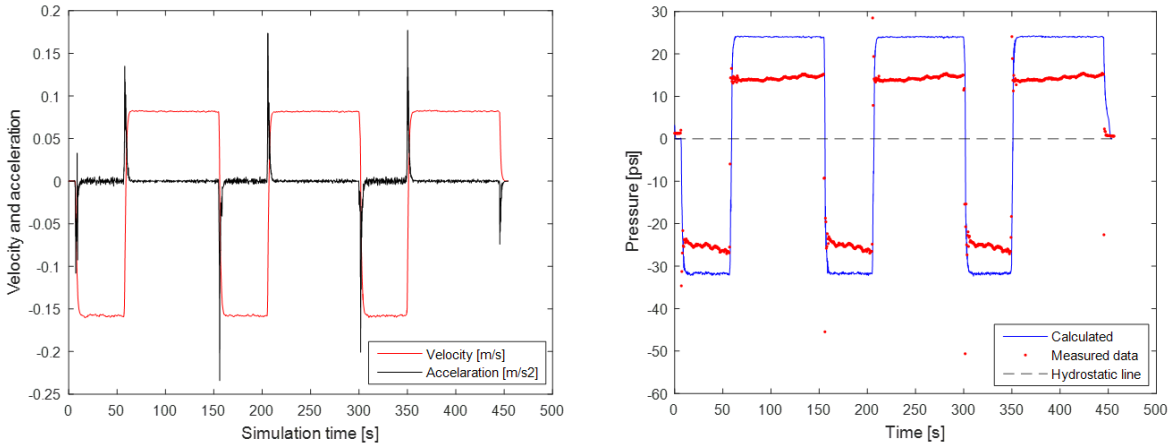

Figure G.32: Coned assembly movement 8, top drive movement (left), measured and calculated surge/swab pressures (right)

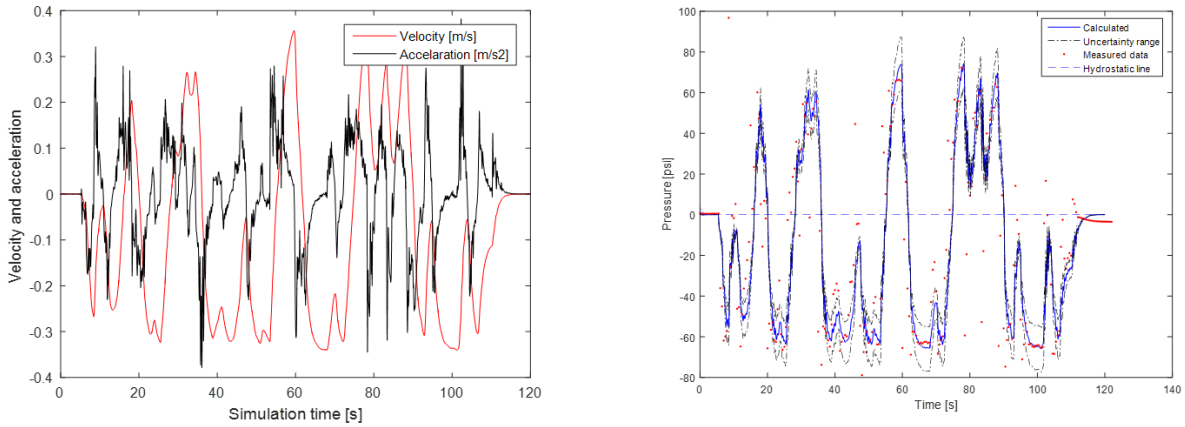

Figure G.33: Coned assembly movement 9, top drive movement (left), measured and calculated surge/swab pressures (right)

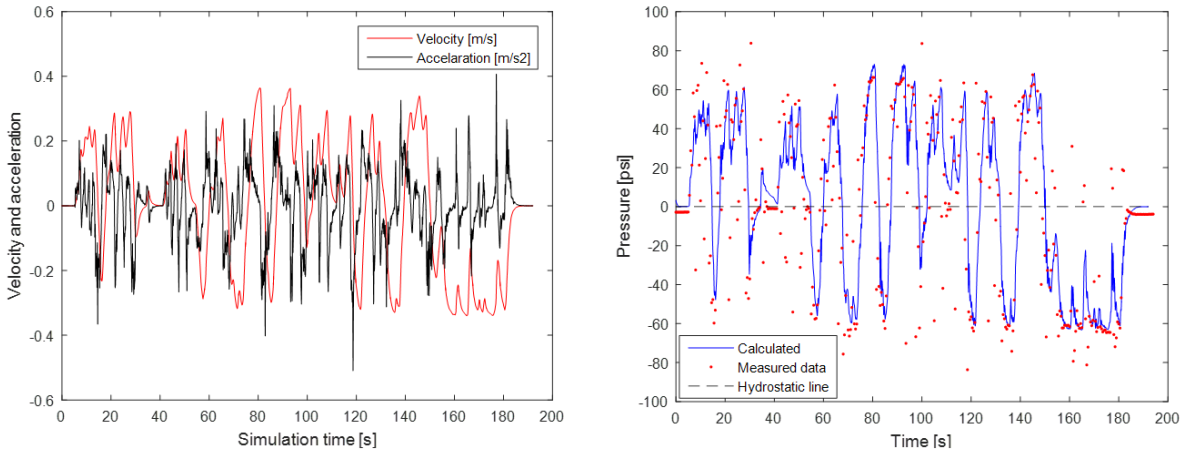

Figure G.34: Coned assembly movement 10, top drive movement (left), measured and calculated surge/swab pressures (right)

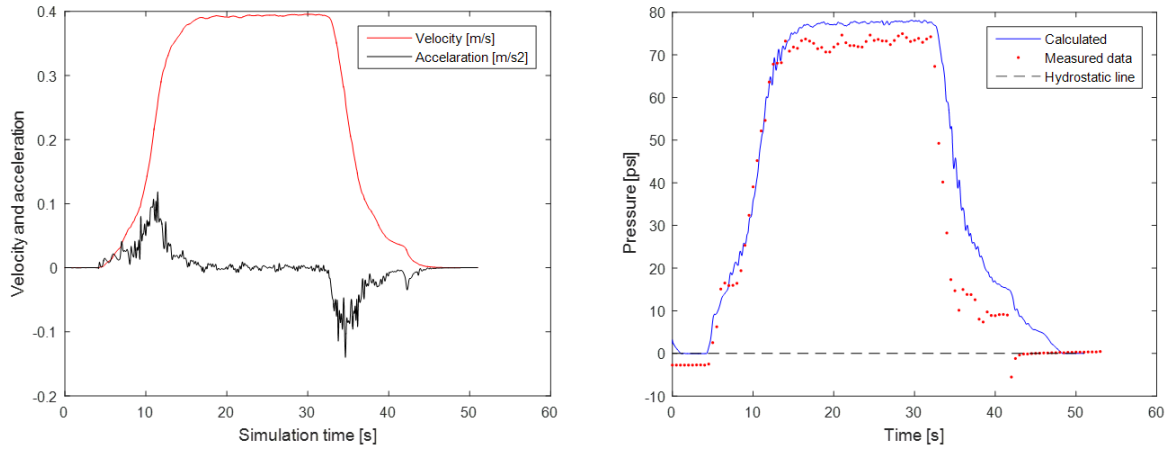

Figure G.35: Coned assembly movement 11, top drive movement (left), measured and calculated surge/swab pressures (right)

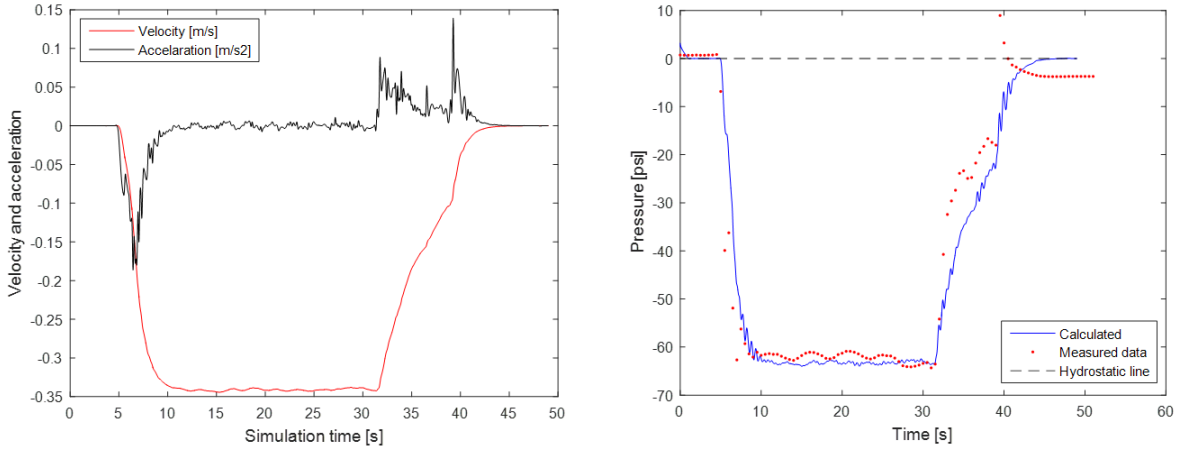

Figure G.36: Coned assembly movement 12, top drive movement (left), measured and calculated surge/swab pressures (right)

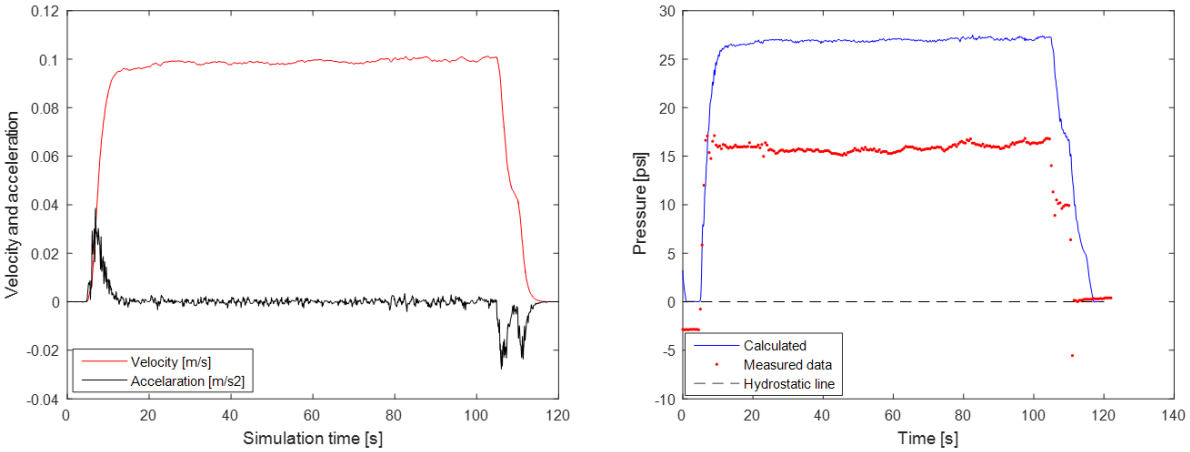

Figure G.37: Coned assembly movement 13, top drive movement (left), measured and calculated surge/swab pressures (right)

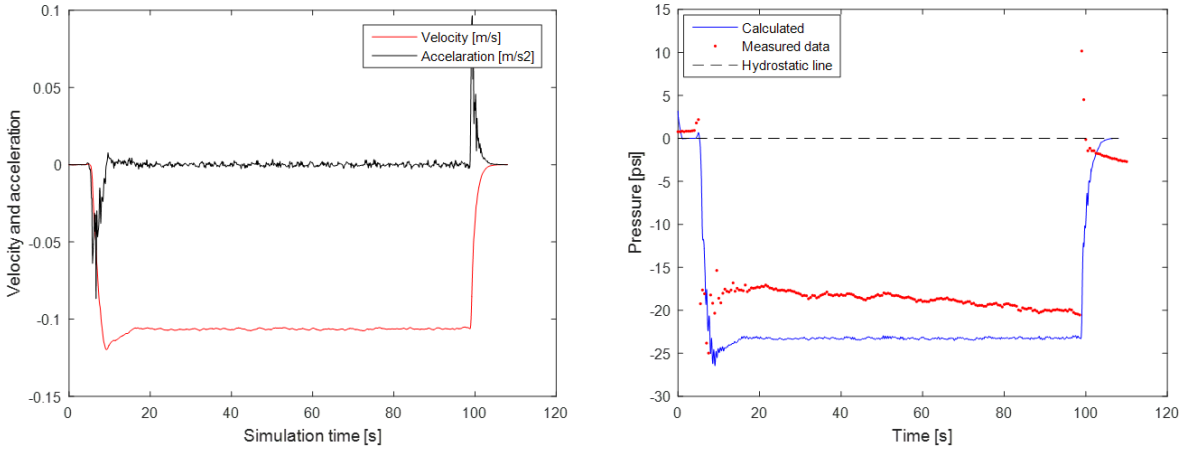

Figure G.38: Coned assembly movement 14, top drive movement (left), measured and calculated surge/swab pressures (right)

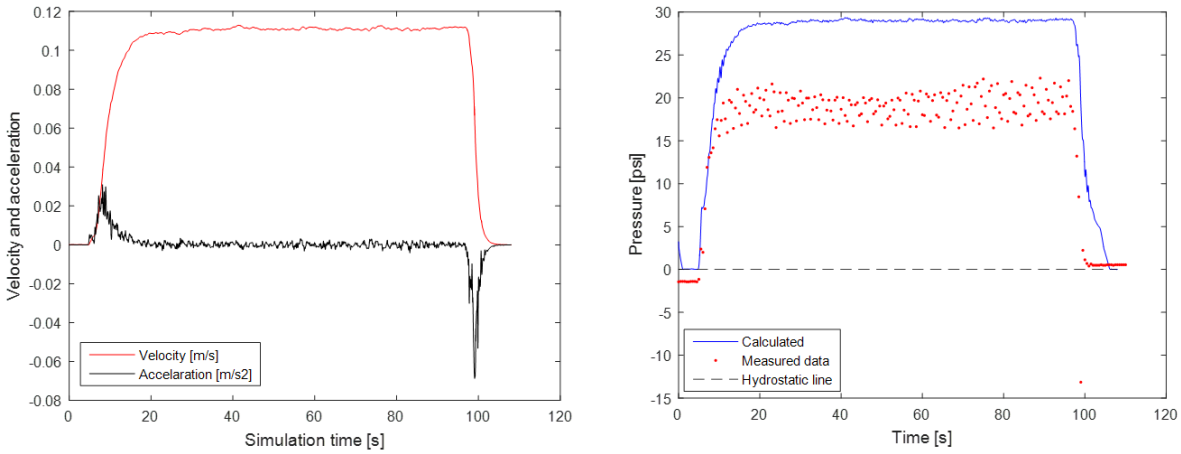

Figure G.39: Coned assembly movement 15, top drive movement (left), measured and calculated surge/swab pressures (right)

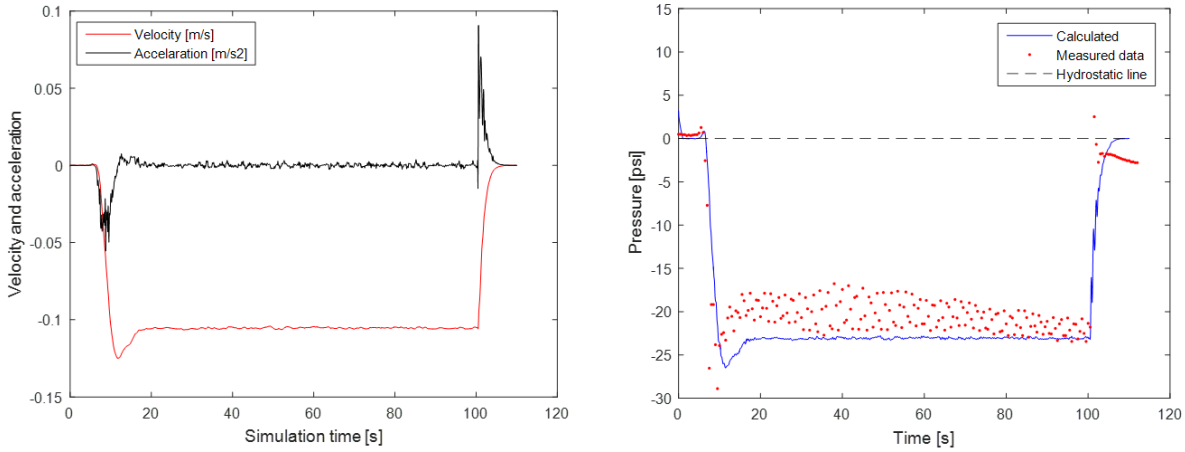

Figure G.40: Coned assembly movement 16, top drive movement (left), measured and calculated surge/swab pressures (right)

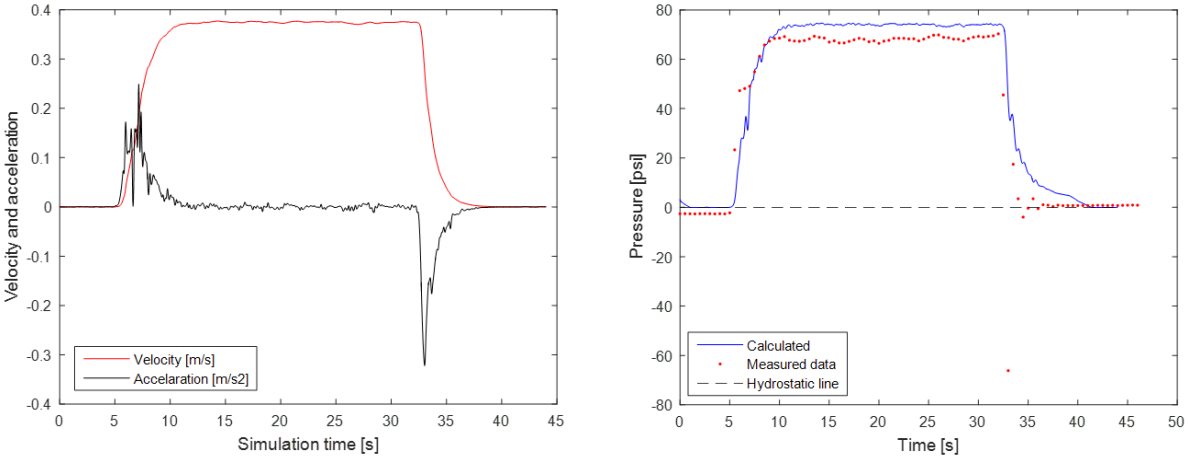

Figure G.41: Coned assembly movement 17, top drive movement (left), measured and calculated surge/swab pressures (right)

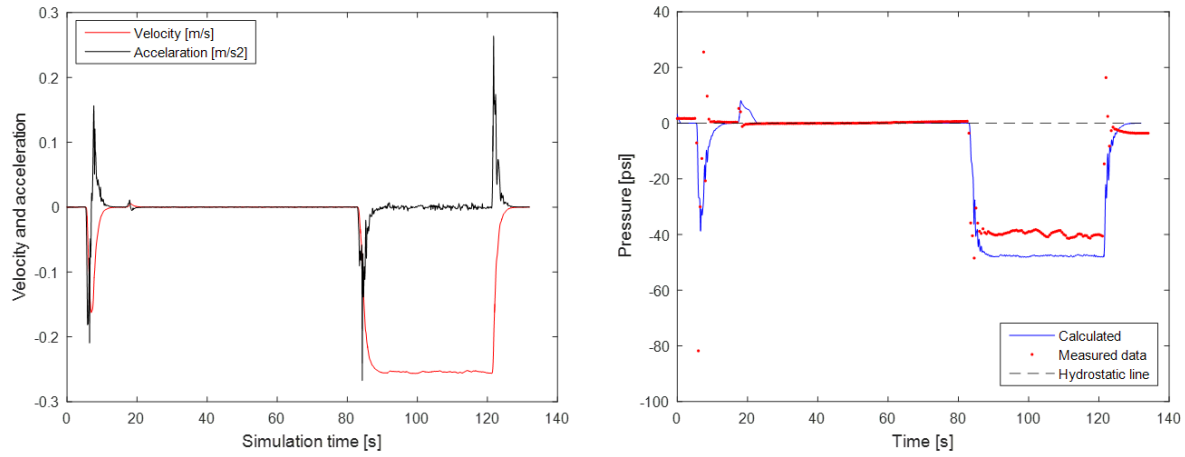

Figure G.42: Coned assembly movement 18, top drive movement (left), measured and calculated surge/swab pressures (right)

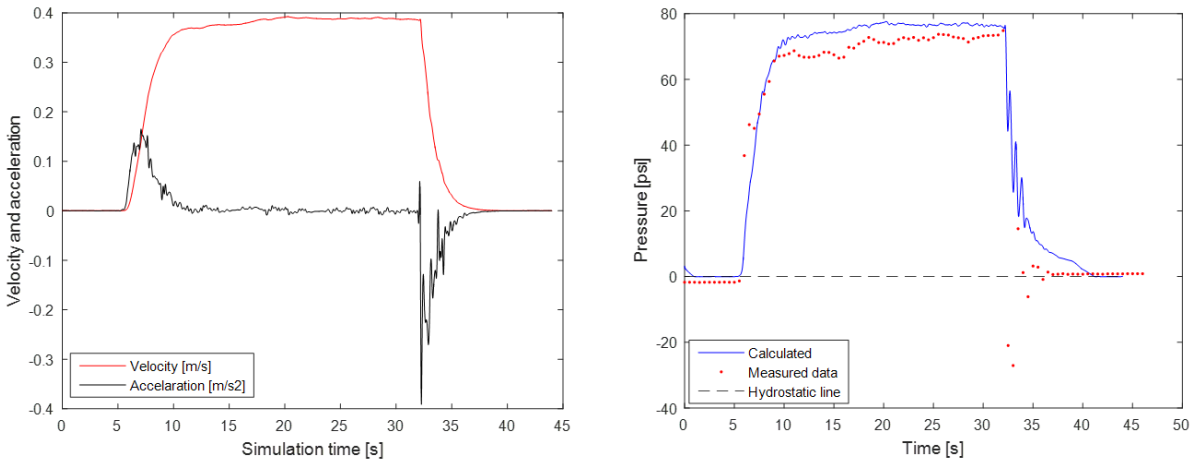

Figure G.43: Coned assembly movement 19, top drive movement (left), measured and calculated surge/swab pressures (right)

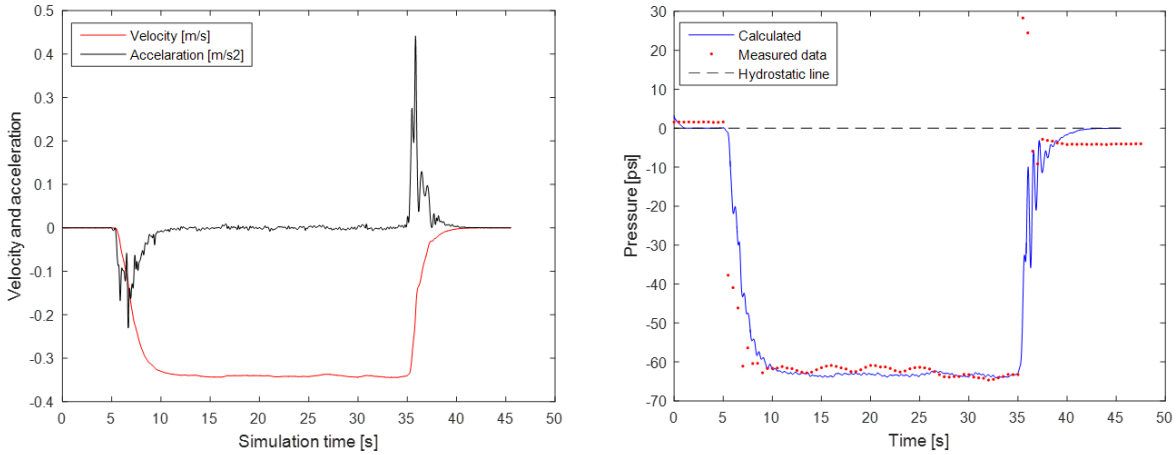

Figure G.44: Coned assembly movement 20, top drive movement (left), measured and calculated surge/swab pressures (right)

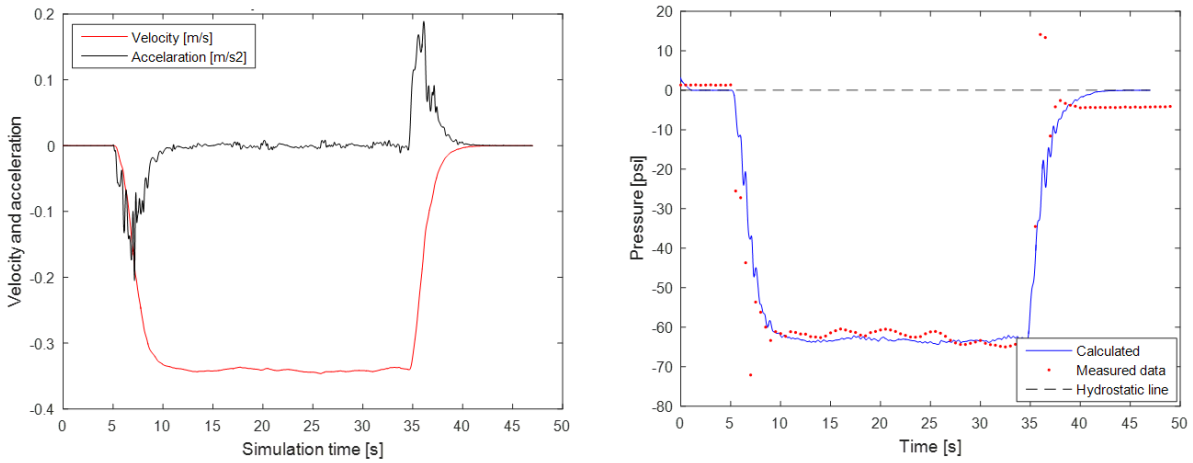

Figure G.45: Coned assembly movement 21, top drive movement (left), measured and calculated surge/swab pressures (right)

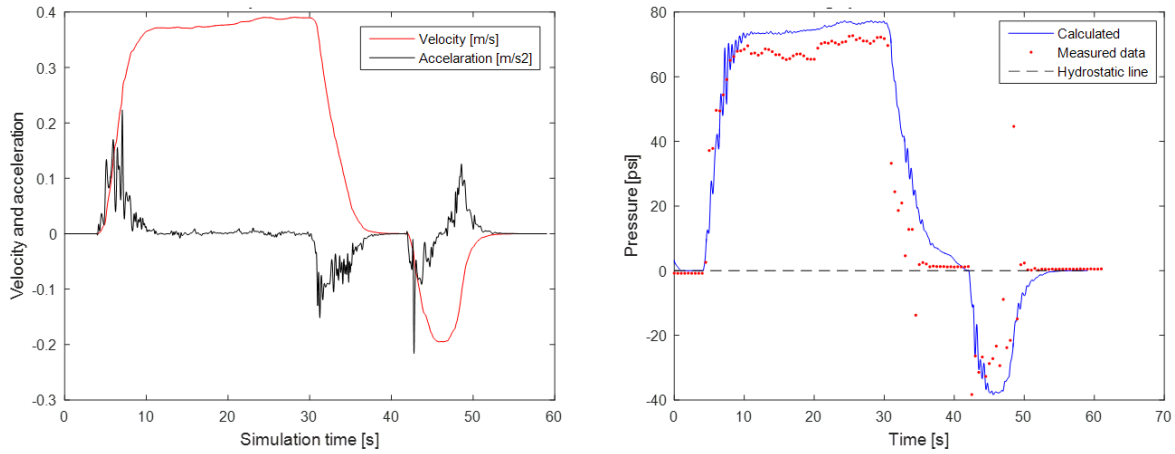

Figure G.46: Coned assembly movement 22, top drive movement (left), measured and calculated surge/swab pressures (right)

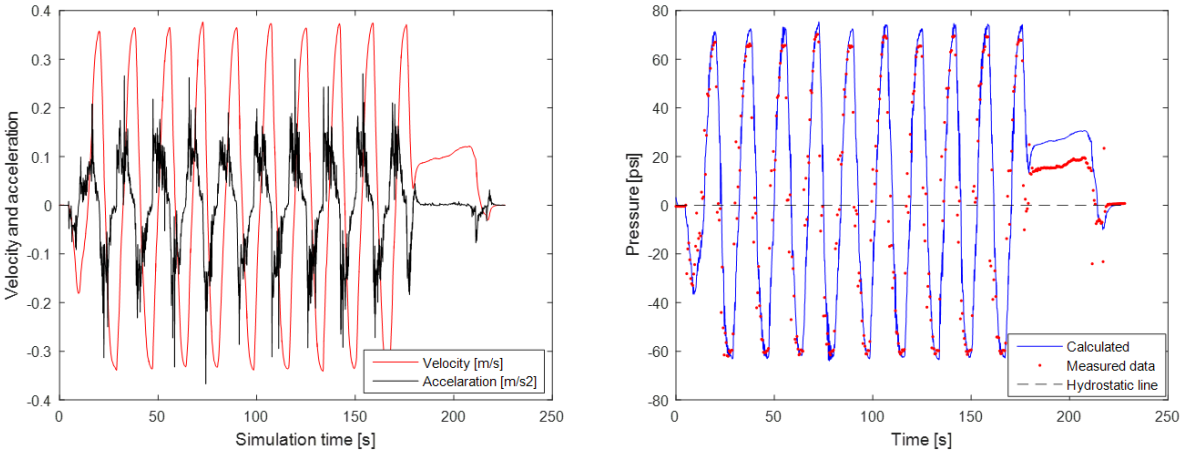

Figure G.47: Coned assembly movement 23, top drive movement (left), measured and calculated surge/swab pressures (right)

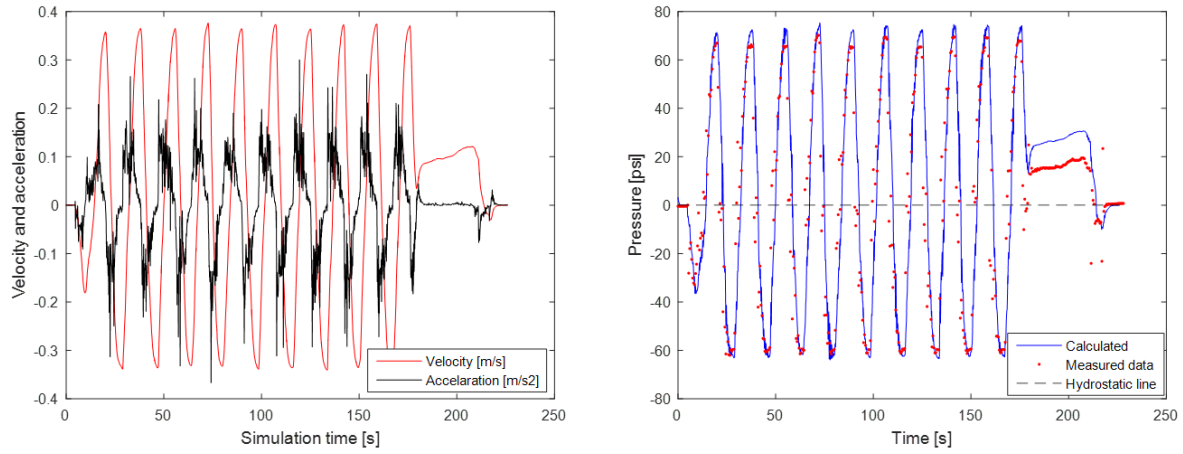

Figure G.48: Coned assembly movement 24, top drive movement (left), measured and calculated surge/swab pressures (right)

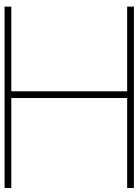

Casestudy

Model Flowchart

See next page

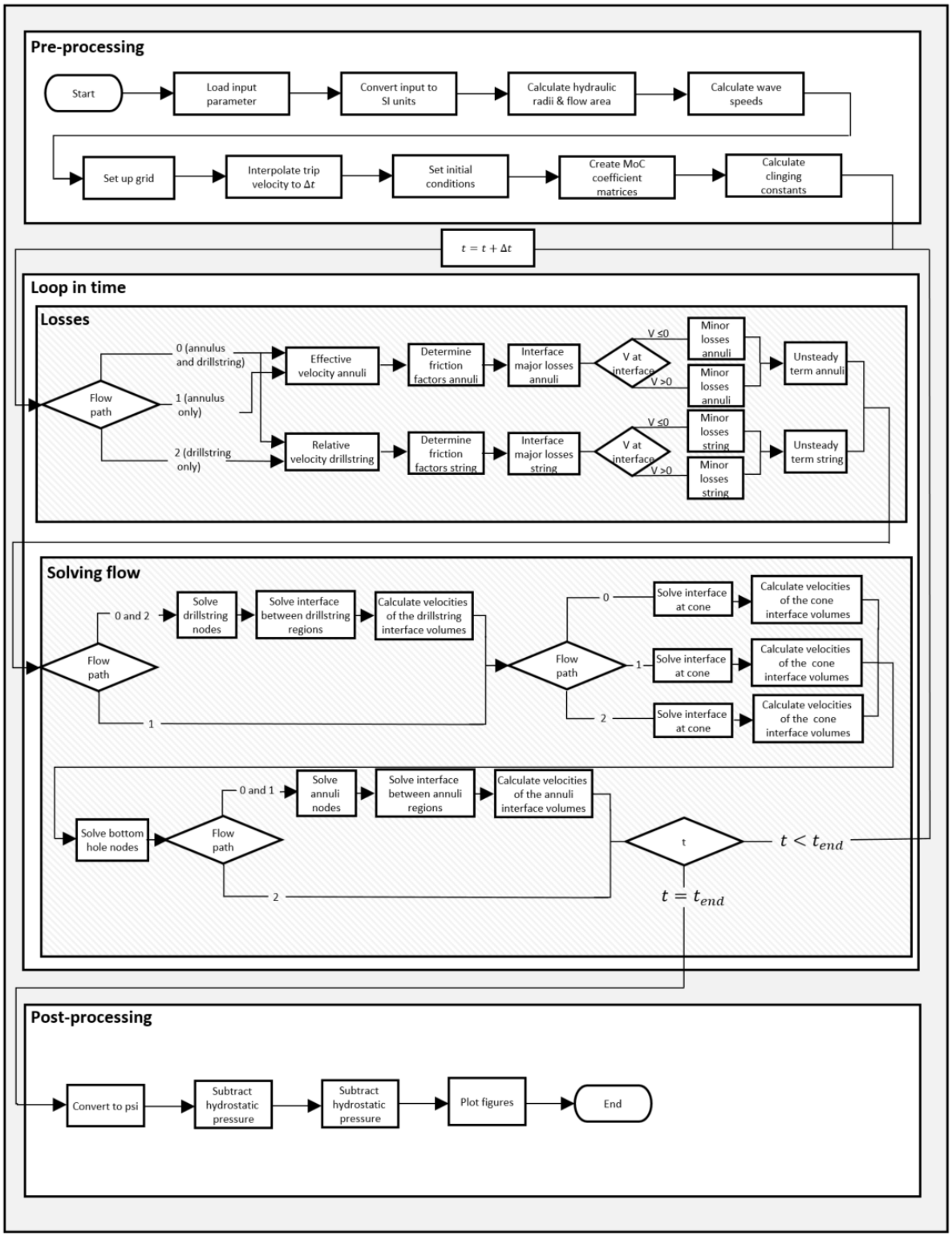

Figure I.1: MoC model flow chart